On the Formation of Magnetic Discontinuities in a Magnetofluid with Large Electrical Conductivity

A THESIS

submitted for the Award of Ph.D. degree of

MOHANLAL SUKHADIA UNIVERSITY

in the

Faculty of Science

by

Dinesh Kumar

Under the Supervision of

Prof. P. Venkatakrishnan

&

Dr. Ramitendranath Bhattacharyya

Udaipur Solar Observatory

Physical Research Laboratory, Udaipur

Department of Physics

Faculty of Science

MOHANLAL SUKHADIA UNIVERSITY

UDAIPUR

2015

DECLARATION

I hereby declare that the research work incorporated in the present thesis entitled ***"On the Formation of Magnetic Discontinuities in a Magnetofluid with Large Electrical Conductivity"*** *is my own work and is original. This work, in part or in full, has not been submitted to any University for the award of a Degree or a Diploma. I have properly acknowledged the material collected from secondary sources wherever required. I solely own the responsibility for the originality of the entire content.*

Date:

Dinesh Kumar

(Author)

Udaipur Solar Observatory

Physical Research Laboratory

Udaipur- 313 001, India

CERTIFICATE

I feel great pleasure in certifying that the thesis entitled ***"On the Formation of Magnetic Discontinuities in a Magnetofluid with Large Electrical Conductivity"*** *embodies a record of the results of investigations carried out by* ***Mr. Dinesh Kumar*** *under my guidance. I am satisfied with the analysis, interpretation of results and conclusions drawn. He has completed the residential requirement as per rules. I recommend the submission of thesis.*

Date:

Prof. P. Venkatakrishnan
(Thesis Supervisor)
Senior Professor
Udaipur Solar Observatory
Physical Research Laboratory
Udaipur- 313 001, India

Dr. Ramitendranath Bhattacharyya
(Thesis Co-Supervisor)
Reader
Udaipur Solar Observatory
Physical Research Laboratory
Udaipur- 313 001, India

Countersigned by

Head of the Department

To

My Late Father

Contents

List of Figures

List of Tables

Acknowledgements

I would first like to thank my thesis advisors, Prof. P. Venkatakrishnan and Dr. Ramitendranath Bhattacharyya, for their constant support, encouragement and guidance throughout this thesis work. I learned many theoretical aspects of the subject matter from Dr. Ramit Bhattacharyya through many fruitful discussions with him. Also, I learned both observational and theoretical aspects of various phenomena on the Sun through valuable discussions with Prof. P. Venkatakrishnan. I have always enjoyed solar physics by working with both of them.

I wish to thank Prof. Piotr K. Smolarkiewicz for helping me in various ways whenever I got stuck with the numerics and the code. I also acknowledge his constructive criticism to improve the quality of the work carried out in this thesis.

I would also like to thank Prof. J. N. Goswami, former Director; Prof. Utpal Sarkar, Director; Prof. P. Janardhan, Dean, for providing necessary facilities to carry out research work at PRL. I am also thankful to the faculty members of PRL, in particular, Dr. D. Chakrabarty, Dr. R. Rangarajan, Prof. S. Ramachandran, Dr. Jitesh R. Bhatt, Dr. Varun Sheel, Dr. Bijaya K. Sahoo, Dr. Bhuwan Joshi, Dr. K. K. Marhas, Prof. M. M. Sarin and Dr. A. Chakraborty for teaching various courses during my PhD course work.

I am also grateful to all the faculty members of USO, Prof. Ashok Ambastha, Prof. Nandita Srivastava, Prof. Shibu K. Mathew, Dr. Brajesh Kumar and Dr. Bhuwan Joshi for their generous helps and encouragements.

I would like to thank Prof. Amitava Bhattacharjee, who gave many valuable suggestions and comments on this thesis work while discussing with him during the COSPAR meeting, 2012. I also wish to thank prof. Paul Charboneau for discussing and providing many insightful views during the EULAG Workshop, 2014.

I am thankful to my seniors, Dr. Anand D. Joshi, Dr. Ram Ajor Maurya, Dr. Rohan Eugene Louis, Dr. Vema Reddy and Ms. Suruchi Goel; to my batch mates, Rajeev, Debashish, Upendra, Wageesh, Avdhesh, Tanmoy, Yashpal, Aadhi, Arko, *Anjali, Bhavya, Damodararao, Dillip, Girish, Gulab, Gangi, Priyanka, Gaurav, Lekshmy, Monojit, Midhun and Naveen; and to my juniors, Alok, Sanjay and Rahul for their company and help in different aspects throughout the thesis work.*

Thanks to all other staff members of USO, Mr. Raja Bayanna, Mr. Naresh Jain, Late Mr. Sudhir K. Gupta, Mr. Raju Koshy, Mr. Rakesh Jaroli, Ms. Ramya Reddy, Mr. Nurul Alam, Mr. Pinakin Shikari, Mr. Mukesh Sardava, Mr. Laxmilal Suthar, Mr. Dalchand Purohit and Mr. Jagdish Chauhan for their help and support in various ways during my stay at USO.

Special thanks to all the staff members of the computer center of PRL, for providing uniterruped computing facility at the HPC cluster. I also wish to acknowledge the visualisation software VAPOR (www.vapor.ucar.edu), for generating relevant graphics used in this thesis.

I would like to thank the Physics Department and the PhD section of Mohanlal Sukhadia University for their kind cooperation throughout my thesis work.

I am also thankful to all the family members at USO colony, Mrs. Usha Venkatakrishnan, Mrs. Mahima, Mrs. Bharati and Ms. Ramya for providing the homely environment with invitations for lunch and dinner on various occasions.

Finally, I express my deep gratitude to my late father to whom this thesis is dedicated. His hard work in his profession has always been an inspiration for me. Thanks to my mother, brother and all family members. Their support and encouragement helped me to concentrate on my thesis work.

Dinesh Kumar

Abstract

The million-degree temperature of the solar corona is an outstanding problem in solar physics since a long time. It is generally believed that the magnetic field of the Sun plays an important role in heating the solar corona. However, the theoretical difficulty is that the magnetic energy for the typical length scales of the coronal structures cannot be dissipated fast enough to compensate for the conductive losses from the corona due to the small electrical resistivity. A plausible mechanism for effective dissipation of magnetic energy is via generation of magnetic discontinuities (MDs). At these locations of discontinuity, a thin layer of electric current density (current sheet) is generated which is dissipated by the small but finite electrical resistivity to produce the necessary heat to maintain the million-degree corona.

It is essential to know the physical process by which MDs can be created. Parker proposed a persuasive idea based on magnetostatic theorem stating that an arbitrary field topology relaxing towards the static equilibrium under the frozen-in condition will develop magnetic discontinuities (MDs) or current sheets (CSs). This basic theoretical process of MD formation is a natural consequence of the general incompatibility to accommodate the arbitrary field topology in the static equilibrium. The demonstration of the formation of magnetic discontinuity is central to the Parker theory. Analytically, attempts have been made to demonstrate the formation of magnetic discontinuities by solving the magnetostatic equation, describing the final static equilibrium of the relaxation process. However, finding an analytical solution of the magnetostatic equation is in general a difficult task, except for special sets of field topology, due to the inherent nonlinear character of the magnetostatic equation. Because of such mathematical difficulties, Parker theory is still an interesting problem in solar physics.

This thesis is concerned with the numerical demonstration of the formation of magnetic discontinuities by studying the dynamical evolution of an initial topology of magnetic field. For the purpose, the full three dimensional time-dependent ideal magnetohydrodynamic (MHD) equations have been solved using the numer-

ical model EULAG-MHD, an extension of the standard hydrodynamic model EULAG (Eulerian-Lagrangian). Numerical demonstration of the formation of MD requires to maintain a high degree of frozen-in condition throughout the dynamical evolution of the magnetic field. Such a high degree of frozen-in condition is achieved by the second order accurate nonoscillatory advection scheme MPDATA (multidimensional positive definite advection transport algorithm). A feature unique to MPDATA and important in our calculations is its proven dissipative property mimicking the action of explicit subgrid-scale turbulence models whenever the concerned advective field is under-resolved. In literature, such calculations relying on the properties of nonoscillatory differencing are referred as implicit large-eddy simulations (ILES). This ILES property of the MPDATA is used to resolve the formation of magnetic discontinuities.

Under the general coronal conditions, the magnetic forces dominate over all other forces like gradient of plasma pressure, gravity, etc., and hence coronal magnetic fields can be approximated to be in static force-free equilibrium. Coronal field lines are rooted to the photosphere, which are continuously shuffled by the convective motion in the photosphere. This shuffling process interlaces the field lines to generate a complex field topology, resulting in build up of Maxwell stresses in the magnetic field. Such a stressed field topology will try to relax towards the static equilibrium while preserving its initial field topology in the coronal medium of large electrical conductivity. The result is the formation of MDs in a similar manner as suggested by Parker. However, the presence of large but finite electrical conductivity of the solar corona avoids to attain the limit of static equilibrium with a true mathematical discontinuity with zero thickness of current sheet. This eventually leads to dissipation of CS along with change in field topology via the process of magnetic reconnection. Such a process then removes the stresses from the magnetic field to achieve the terminal state of equilibrium. This interplay between Maxwell stresses and dissipation of CSs continues and keeps the coronal magnetic fields in the quasi-steady equilibrium.

The fluid with large electrical conductivity, thus, has a remarkable property to dissipate the energy with a simultaneous preservation of field topology, providing a way to find the minimum energy state of terminal equilibrium based on the techniques of variational calculus. We use the two-fluid plasma model to find the terminal state with flow coupled to magnetic field. Such an equilibrium may have possible application in modeling the high β solar corona.

In this thesis, we have numerically investigated the formation of MDs in an initial complex topology of magnetic field undergoing viscous relaxation in an incompressible fluid with infinitely large electrical conductivity. The role of the initial topological structure of the magnetic field in generation of magnetic discontinuities is investigated. This study has the importance to explore the potential sites where MDs may appear. Moreover, this thesis is also devoted to investigate the possible role of repeated magnetic reconnections in generating various magnetic structures, like tornadoes and magnetic flux ropes, as the magnetic field configuration, initially out of equilibrium, relaxes towards the quasi-steady state. Such magnetic structures are topologically similar in appearance to that observed in the solar corona. Finally, we have attempted to address the possibility of finite time formation of magnetic discontinuities.

Chapter 1

Introduction

1.1 Motivation

Observations show that the outer atmosphere (corona) of the Sun possesses extremely high temperature of the order of million degrees Kelvin [1]. However, the temperature of the solar surface (photosphere) is about 6000 K [2]. These observations suggest that the elevated coronal temperature cannot be a direct consequence of heat transfer by thermal conduction or radiation in accordance with the second law of thermodynamics [3]. The heat flows from the corona towards the lower atmosphere, and therefore to balance the energy loss from the corona some heating mechanism is required [4]. It is generally believed that the magnetic field plays a fundamental role, and that the source of this energy derives from convective motions in the photosphere. Because of the high temperature, coronal gas becomes fully ionized and behaves as a plasma with large electrical conductivity, large enough in a sense that magnetic field lines are tied with the fluid elements of the coronal plasma— called the flux-freezing or frozen-in condition [5]. From theoretical viewpoint, it seems that the magnetic energy cannot be dissipated in the solar corona due to the large electrical conductivity of the coronal medium [3]. Then the crucial point is what are the physical mechanisms responsible for transferring the energy from the photosphere to the corona and dissipating there as heat.

Parker proposed that the coronal magnetic fields are continuously deformed

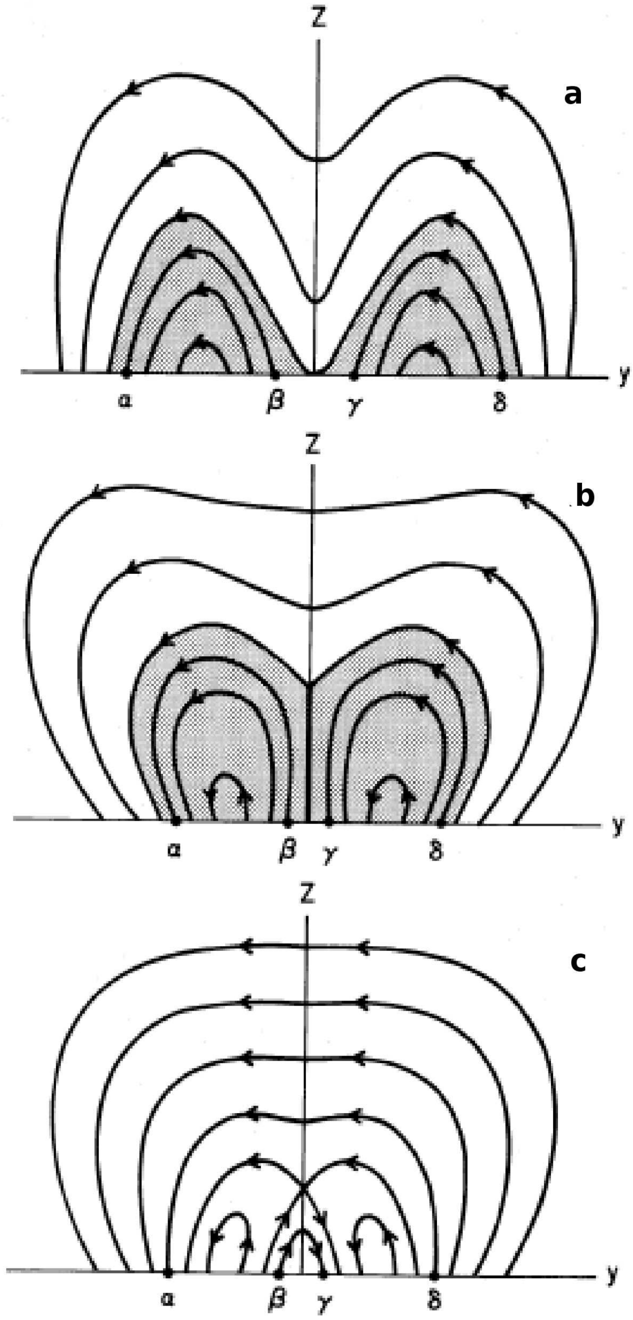

Figure 1.1: Panel a depicts a continuous quadrupolar magnetic field configuration which is being deformed by imposing continuous footpoint displacement in the y-direction. The two lines of force are identified by their footpoints $\alpha, \beta, \gamma, \delta$. Panel b shows the formation of magnetic discontinuity, where the magnetic field is discontinuous across the vertical current sheet. The field topology of this configuration is same as the panel a since the connectivities of footpoints does not change. Panel c illustrates the dissipation of current sheet and the change in field topology. Taken from [6].

by the convective motion that brings any two portions of the field lines towards each other to meet at a surface and form magnetic discontinuities (MDs), of which eventual dissipation provides sufficient heat to maintain corona at its million degree Kelvin temperature [7, 8, 9]. The essential to this Parker's idea of MD formation is the large electrical conductivity of the coronal medium. To focus on the basic idea, let us consider a continuous quadrupolar magnetic field [6] embedded in a fluid with large electrical conductivity as shown in the panel a of Figure 1.1. This initial magnetic configuration is continuously deformed under the frozen-in condition by imposing magnetic footpoint displacement. The two shaded lobes of the bipolar fields approach towards each other by expelling out the magnetic field and fluid in between them. Subsequently, the two shaded lobes of the field lines come into contact (panel b, Fig. 1.1) at a line, across which the tangential field jumps discontinuously. It is to be noted that this new magnetic configuration is topologically similar to that of panel a, Figure 1.1, as the connectivities of the footpoints of the field lines remain the same. The discontinuous magnetic field generates an electric current density, called the current sheet (CS) due to its two-dimensional appearance (an extension of the contact line in the third direction x). In the absence of electrical resistivity, the thickness of the current sheet is zero with an infinite electric current density. However in a real plasma, the presence of small but finite electrical resistivity dissipates the current sheet via Joule heating, and the thickness of the CS to a zero limit cannot be attained. In this dissipative process, magnetic reconnection [5] takes place which rearranges the field topology that makes the magnetic field once again continuous everywhere as shown in panel c of Figure 1.1. The above physical process then explain the formation of magnetic discontinuity in the solar corona where magnetic field lines are continuously deformed through shuffling their footpoints by convective motion in the photosphere [10]. The MD forms and dissipates along with change in field topology. The field lines are again deformed and new MD forms. This ongoing process of the formation of MDs and their eventual decay supply the continuous heat to the solar corona [3, 11]. Further details of this process of MD formation and its consequence in context of the solar corona are discussed in the chapter 5.

The basic physical process of the MD formation as suggested by Parker, though, appears to be simple but its mathematical demonstration is formidably difficult, in general [3, 12]. This fundamental process of MD formation, thus, provides the motivation for this thesis work to numerically understand the physics of discontinuity formation and its consequence that have possible relevance to coronal physics.

The above process of discontinuity formation is not unique to the solar magnetic fields but also appear in a wide range of physical systems like stellar magnetic fields (Sun-like stars) [3, 13], terrestrial magnetic fields [14, 15, 16, 17] and Laboratory plasmas [18, 19, 20]. In these physical systems, the appearance of magnetic discontinuities is due to the constraints of field topology as a result of large electrical conductivity of the plasma. Mathematically, the origin of discontinuity is inherent to the nonlinear nature of the governing partial differential equations [21, 22]. Discontinuities associated with nonlinearities will be discussed in chapter 2.

1.2 Thesis Overview

We have seen that the formation of magnetic discontinuity plays a crucial role in determining the dynamics of the magnetofluid. The formation of magnetic discontinuities and their subsequent decay leads the magnetofluid to the asymptotes of magnetostatic equilibrium [3], depicting the terminal state of the magnetofluid. In this thesis, our objectives are the following. (1) To analytically determine the terminal state of equilibrium. (2) To numerically explore the formation of magnetic discontinuities and their subsequent reconnection. The chapterwise details of the thesis are as follows.

Chapter 2 covers details of the plasma models, e.g. the two-fluid and the single-fluid, required to understand the terminal state and the dynamics of discontinuity formation. Also, we discuss the theoretical concepts of discontinuity formation. The role of the nonlinearity in generating discontinuity will be addressed.

In chapter 3, we discuss the employed numerics of the model EULAG-MHD, an extension of EULAG (Eulerian-Lagrangian) [23], that solves the sets of non-linear partial differential equations of ideal magnetohydrodynamics (MHD). This numerical model is based on a second order accurate nonoscillatory forward-in-time numerical algorithm, MPDATA (multidimensional positive definite advection sheme) [24]. We also discuss the novelty of the numerical algorithm as introduced in this thesis in the MPDATA.

Chapter 4 documents the present status of the work related to the formation of magnetic discontinuity. We will survey both the theoretical and the computational works done in this direction.

In chapter 5, we will address the general physical conditions of the solar corona and the possibility of the formation of magnetic discontinuities. Also, we will highlight some important physical phenomena mostly observed at the solar atmosphere, like flares and CMEs, as a consequence of discontinuity formation and their eventual decay.

Chapter 6 explores the role of discontinuity formation in constructing the variational problem to find the terminal state of equilibrium. We propose a terminal state obtained by two-fluid plasma model applied to an open system like the solar corona. The various topological properties of the terminal magnetic field are studied.

In chapter 7, we numerically investigate the formation of magnetic discontinuity in a magnetofluid with infinitely large electrical conductivity based on suitable initial value problems (IVPs). Two sets of numerical experiments are carried out. The first set of experiments utilize an initial magnetic field with periodic boundary conditions to demonstrate only the formation of magnetic discontinuities. The second set of experiment utilizes the initial magnetic field with open boundary conditions, which is relevant to the general morphology of coronal magnetic fields. Here we elaborate on the dynamics of discontinuity formation and the subsequent magnetic reconnection till the magnetofluid reaches to the quasi-steady equilibrium. We will discuss the role of repetitive reconnections in generating various magnetic structures which are topologically similar to that observed in the solar atmosphere.

Chapter 8 deals with an important problem of ideal magnetohydrodynamics that whether a magnetic discontinuity appears in a finite or an infinite time. In this chapter, we present some numerical results which address the issue of finite time formation of magnetic discontinuities.

In chapter 9, we will briefly summarize the work carried out in this thesis and also highlight the possible future work pursued in this direction.

Chapter 2

Theoretical Background

In this chapter we first highlight some basics of theoretical models of the plasma, required to understand the dynamics of discontinuity formation in magnetic fields. Some important features of the magnetohydrodynamics (MHD) under the constraint of infinitely large electrical conductivity will be discussed. We discuss the role of nonlinearity in generation of discontinuity. Since the nonlinearity is associated with the governing partial differential equations (PDEs), it is therefore necessary to understand the nature of the concerned PDEs. The method of characteristic [21, 22] is a useful technique to solve the PDEs. The characteristic determines the basic nature of PDEs. Based on the method of characteristics, we will show the inevitability of discontinuity formation in a fluid with infinitely large electrical conductivity. Also, the appearance of discontinuity from physical viewpoint is presented. The optical analogy [3] is introduced to understand the dynamics of discontinuity formation in magnetic fields.

2.1 Plasma Models

A plasma is a quasi-neutral gas of charged and neutral particles which exhibits collective behavior [25]. The charge imbalance produced by thermal motion spontaneously builds up electric field to the extent that the associated electrostatic energy balances the thermal energy. This yields the Debye length λ_D over which the plasma remains quasi-neutral [26]. Thus the Debye length is the spatial scale associated with the charge separation, which is effectively screened from rest of the plasma system. Therefore for a complete shielding there must be a sufficiently large number of particles [27]. As a result of charge separation the electrons oscillate, with plasma frequency ω, collectively about the heavy ions in response to the restoring force provided by the long-range Coulomb attraction. There is also short-range interaction between neutrals and charged particles, which effectively damp the oscillation. Consequently, the collision frequency of electrons with neutrals must be smaller than that with the ions to sustain the plasma oscillation, i.e., $\omega\tau > 1$ where τ is the mean time between collisions of electrons with neutrals.

The complexity of the plasma dynamics is reduced by certain assumptions and approximations, which give various plasma models. In the following, we discuss only those models which are relevant to our thesis.

2.1.1 Two-fluid Plasma Model

The governing equations of a fully ionized plasma consisting of only two species $\alpha = e, i$, electrons and singly charged ions, are obtained by taking the moments of Boltzmann equation [28]. With respective to these moments, we obtain the mass, the momentum and the energy conservation equations, written as

$$\frac{\partial n_\alpha}{\partial t} + \nabla \cdot (n_\alpha \mathbf{u}_\alpha) = 0, \quad (2.1.1)$$

$$m_\alpha n_\alpha \left[\frac{\partial \mathbf{u}_\alpha}{\partial t} + (\mathbf{u}_\alpha \cdot \nabla)\mathbf{u}_\alpha\right] = -\nabla \cdot \boldsymbol{\mathcal{P}}_\alpha + q_\alpha n_\alpha (\mathbf{E} + \mathbf{u}_\alpha \times \mathbf{B}) + \mathbf{R}_{\alpha\beta}, \quad (2.1.2)$$

$$\frac{\partial}{\partial t}\left(\frac{3}{2}p_\alpha\right) + \nabla \cdot \left(\frac{3}{2}p_\alpha \mathbf{u}_\alpha\right) + (\boldsymbol{\mathcal{P}}_\alpha \cdot \nabla) \cdot \mathbf{u}_\alpha + \nabla \cdot \mathbf{q}_\alpha = \mathbf{S}_{\alpha\beta}. \quad (2.1.3)$$

Here the number density n_α, the fluid velocity $\mathbf{u}_\alpha$, the stress tensor (pressure tensor) $\boldsymbol{\mathcal{P}}_\alpha$, the momentum transfer vector due to collisions of particles $\mathbf{R}_{\alpha\beta}$, the scalar pressure p_α, the heat flux vector $\mathbf{q}_\alpha$, and the collisional dissipation $\mathbf{S}_{\alpha\beta}$ refer to each species α. Under the adiabatic approximation (where the heat flux and other collision terms can be neglected) equation (2.1.3) forms the closure for the two-fluid equations. With this, the conservation equations (2.1.1)-(2.1.3) together with the Maxwell's equations then form the complete set of two-fluid equations.

2.1.2 Single-fluid Plasma Model

The two-fluid description of plasma still contains the microscopic informations which, in turn, implies that solving these equations are in general cumbersome. Following [25], such complexities of plasma can be further reduced by assuming the concerned phenomena of interest to be of large spatial ($L \gg \lambda_D$) and temporal scales $\tau \ll \tau_e = 1/\omega$. We also assume that the electron inertia is much smaller ($m_e \ll m_i$) than the ion inertia and the bulk plasma flow is non-relativistic, i.e., ($v \ll c$). These approximations then allow us to treat the two species, electrons and ions, as a single-fluid. The complete set of single-fluid equations, or the MHD equations, read as

$$\frac{\partial \rho}{\partial t} + \nabla \cdot (\rho \mathbf{u}) = 0, \tag{2.1.4}$$

$$\nabla \cdot \mathbf{J} = 0, \tag{2.1.5}$$

$$\rho \left[\frac{\partial \mathbf{u}}{\partial t} + (\mathbf{u} \cdot \nabla) \mathbf{u} \right] = -\nabla \cdot \boldsymbol{\mathcal{P}} + \mathbf{J} \times \mathbf{B}, \tag{2.1.6}$$

$$\mathbf{E} + \mathbf{u} \times \mathbf{B} = \eta_e \mathbf{J}, \tag{2.1.7}$$

$$\frac{d}{dt} \left(\frac{p}{\rho^\gamma} \right) = 0, \tag{2.1.8}$$

$$\nabla \times \mathbf{B} = \mu_0 \mathbf{J}, \tag{2.1.9}$$

$$\nabla \times \mathbf{E} = -\frac{\partial \mathbf{B}}{\partial t}, \tag{2.1.10}$$

$$\nabla \cdot \mathbf{B} = 0. \tag{2.1.11}$$

Plugging the electric field $\mathbf{E}$ from the Ohm's law (2.1.7) in the Faraday's law (2.1.10) and then substituting current density $\mathbf{J}$ from the Ampere's law (2.1.9) then yields a relation between the magnetic field $\mathbf{B}$ and the velocity field $\mathbf{u}$ as

$$\frac{\partial \mathbf{B}}{\partial t} = \nabla \times (\mathbf{u} \times \mathbf{B}) + \eta \nabla^2 \mathbf{B}, \tag{2.1.12}$$

where $\eta = \eta_e/\mu_0$ is the magnetic diffusivity. This relation is known as the induction equation [27]. The physical significance of this induction equation is that the change in magnetic field is being carried out in response to the advection/convection of the magnetic field by the flow velocity $\mathbf{u}$ and that due to the diffusion of the magnetic field. The relative dominance of these two terms can be conveniently measured by a dimensionless parameter, the magnetic Reynolds number R_M, which is the ratio of the convective term over the diffusive term. This parameter R_M is akin to the fluid Reynolds number R_F of hydrodynamics, measuring the ratio of inertial term and the viscous term of the Navier-Stokes equation. In other words, R_M is defined as the ratio between the diffusive time scale τ_d to that of the advective time scale τ_c. If the advective time scale is replaced with the Alfven time scale $\tau_A = B_0/\sqrt{\mu_0 \rho_0}$ in R_M, we get the Lundquist number S. Thus for a characteristic length scale L_0 and a characteristic fluid speed u_0,

$$R_M = \frac{\mid \nabla \times (\mathbf{u} \times \mathbf{B}) \mid}{\mid \eta \nabla^2 \mathbf{B} \mid} = \frac{u_0 L_0}{\eta}, \tag{2.1.13}$$

where, if $R_M \ll 1$ then the system is diffusive whereas for $R_M \gg 1$ the system is flow dominated. In absence of the magnetic diffusivity η, in a fluid with infinite electrical conductivity, the induction equation (2.1.12) leads to $R_M \to \infty$, implying a fully flow-dominated system and is characterized by ideal MHD. In such an ideal system, the magnetic field lines move with the plasma flow as though both the magnetic field lines and the plasma are tied together— called the flux-freezing condition [5, 26]. That is to say the magnetic flux associated with any arbitrary fluid element remains conserved. This is an important consequence of an ideal MHD.

2.2 Origin of Discontinuity: A Mathematical Perspective

Here we focus on the origin of discontinuity in a nonlinear system from the mathematical point of view. The method of characteristics [21, 22, 29] is a powerful technique to solve partial differential equations. This technique essentially utilizes the idea to transform the given partial differential equation to an ordinary differential equation (ODE) along a given characteristic curve. It is the nonlinear hyperbolic PDE that has the property to develop discontinuity [22, 30].

In the following we take an important example of magnetostatic equilibrium [3] from magnetohydrodynamics (MHD) and investigate its mathematical behavior, in general. The balance between the fluid pressure and the Maxwell stresses in magnetic fields is represented by the magnetostatic equation given by

$$(\nabla \times \mathbf{B}) \times \mathbf{B} = \mu_0 \nabla p, \tag{2.2.1}$$

where $p(\mathbf{x})$ represents the fluid pressure. The magnetic field $\mathbf{B}(\mathbf{x})$ satisfies the solenoidality condition

$$\nabla \cdot \mathbf{B} = 0. \tag{2.2.2}$$

The equations (2.2.1)-(2.2.2) can also be written in their component forms of a Cartesian three dimensional space as

$$\begin{aligned} B_j \frac{\partial B_j}{\partial x_i} - B_j \frac{\partial B_i}{\partial x_j} + \mu_0 \frac{\partial p}{\partial x_i} &= 0, \\ \frac{\partial B_j}{\partial x_j} &= 0. \end{aligned} \tag{2.2.3}$$

In order to understand the fundamental property of these four sets of differential equations (2.2.3), i.e., the magnetostatic equation, we can fix an arbitrary curve $\mathbf{\Gamma}$ on which the values of $p(\mathbf{x}(s))$ and $\mathbf{B}(\mathbf{x}(s))$, with s as a parameter, are specified. The directional derivatives of $p(\mathbf{x}(s))$ and $\mathbf{B}(\mathbf{x}(s))$ along this curve $\mathbf{\Gamma}$, with direction cosines $\alpha_j = \frac{dx_j}{ds}$ $(j = x, y, z)$, are given by

$$\begin{aligned} \frac{dp}{ds} &= \alpha_j \frac{\partial p}{\partial x_j}, \\ \frac{dB_i}{ds} &= \alpha_j \frac{\partial B_i}{\partial x_j}. \end{aligned} \tag{2.2.4}$$

Thus we have a set of eight linear equations (2.2.3)-(2.2.4) with twelve unknowns of partial derivatives of p and B_i $(i = x, y, z)$. Obviously, these equations cannot be solved due to inconsistency between the number of unknown variables and the available sets of equations. Therefore we need to provide some extra conditions so that the number of unknown variables get reduced to the same as the number of independent equations. These extra conditions are met by specifying the values of unknowns on the initial curve $\mathbf{\Gamma}$. The specification of all the z-components of partial derivatives of p and B_i along the curve $\mathbf{\Gamma}$ then guarantees that the equations (2.2.3)-(2.2.4) can be solved. We can cast the equations (2.2.3)-(2.2.4) in matrix form as

$$\begin{bmatrix} \mu_0 & 0 & 0 & -B_y & B_y & 0 & B_z & 0 \\ 0 & \mu_0 & 0 & B_x & -B_x & 0 & 0 & B_z \\ 0 & 0 & 0 & 0 & 0 & 0 & -B_x & -B_y \\ 0 & 0 & 1 & 0 & 0 & 1 & 0 & 0 \\ \alpha_x & \alpha_y & 0 & 0 & 0 & 0 & 0 & 0 \\ 0 & 0 & \alpha_x & \alpha_y & 0 & 0 & 0 & 0 \\ 0 & 0 & 0 & 0 & \alpha_x & \alpha_y & 0 & 0 \\ 0 & 0 & 0 & 0 & 0 & 0 & \alpha_x & \alpha_y \end{bmatrix} \begin{bmatrix} \frac{\partial p}{\partial x} \\ \frac{\partial p}{\partial y} \\ \frac{\partial B_x}{\partial x} \\ \frac{\partial B_x}{\partial y} \\ \frac{\partial B_y}{\partial x} \\ \frac{\partial B_y}{\partial y} \\ \frac{\partial B_z}{\partial x} \\ \frac{\partial B_z}{\partial y} \end{bmatrix} = \begin{bmatrix} 0 \\ 0 \\ 0 \\ 0 \\ dp \\ dB_x \\ dB_y \\ dB_z \end{bmatrix} \tag{2.2.5}$$

If the determinant of the coefficient matrix of the above equation (2.2.5) is zero then the eight unknown derivatives cannot be computed. Such a condition of the vanishing value of the determinant then yields the direction of the characteristic curve determined by the equation

$$\begin{vmatrix} \mu_0 & 0 & 0 & -B_y & B_y & 0 & B_z & 0 \\ 0 & \mu_0 & 0 & B_x & -B_x & 0 & 0 & B_z \\ 0 & 0 & 0 & 0 & 0 & 0 & -B_x & -B_y \\ 0 & 0 & 1 & 0 & 0 & 1 & 0 & 0 \\ \alpha_x & \alpha_y & 0 & 0 & 0 & 0 & 0 & 0 \\ 0 & 0 & \alpha_x & \alpha_y & 0 & 0 & 0 & 0 \\ 0 & 0 & 0 & 0 & \alpha_x & \alpha_y & 0 & 0 \\ 0 & 0 & 0 & 0 & 0 & 0 & \alpha_x & \alpha_y \end{vmatrix} = 0. \tag{2.2.6}$$

This equation (2.2.6) can be further simplified to read as

$$(\alpha_x^2 + \alpha_y^2)(\alpha_x\ B_y - \alpha_y\ B_x)^2 = 0. \tag{2.2.7}$$

On solving the above equation (2.2.7) for $\frac{dy}{dx}$ gives two imaginary values, $\frac{dy}{dx} = \pm i$, and two degenerate real values, $\frac{dy}{dx} = \frac{B_y}{B_x}$. These solutions represent the slopes of the characteristic curves. Consequently, the magnetostatic equation (2.2.1) has two imaginary family of characteristic curves and one real family of characteristic curve. Therefore, the magnetostatic equation is a mixed elliptic hyperbolic type of partial differential equation. Here the real characteristic represents the magnetic field line that permits the formation of discontinuity.

2.3 Origin of Discontinuity: A Physical Perspective

In the previous section we have developed the basic mathematical background to explore the origin of discontinuity. It is seen that discontinuity arises due to nature of the partial differential equations themselves. The development of discontinuities in magnetohydrodynamics are evident from the nature of the concerned governing partial differential equations. In this section we will try to understand the origin of discontinuity from the physical viewpoint— only restricted to the magnetohydrodynamics.

Before presenting the details of the physical construction, in the following we show some important features of the magnetostatic equation (2.2.1) as discussed by Parker [3]. Taking the dot product of $\mathbf{B}$ on both sides of the equation (2.2.1), yields

$$\mathbf{B} \cdot \nabla p = 0, \tag{2.3.1}$$

representing that the fluid pressure p is constant along the magnetic field line. If fluid pressure p is uniform throughout some finite region, then $\nabla p = 0$ and equation (2.2.1) takes the form

$$(\nabla \times \mathbf{B}) \times \mathbf{B} = 0. \tag{2.3.2}$$

This relation is referred as the force-free equation due to the absence of any external forces like pressure, gravity, viscous drag, etc. Equation (2.3.2) can also be written as

$$\nabla \times \mathbf{B} = \alpha(\mathbf{r})\mathbf{B}, \tag{2.3.3}$$

where $\alpha(\mathbf{r})$ represents the torsion coefficient—a measure of circulation per unit magnetic flux [31]. Operating the divergence on equation (2.3.3) leads to

$$\mathbf{B} \cdot \nabla\alpha(\mathbf{r}) = 0, \tag{2.3.4}$$

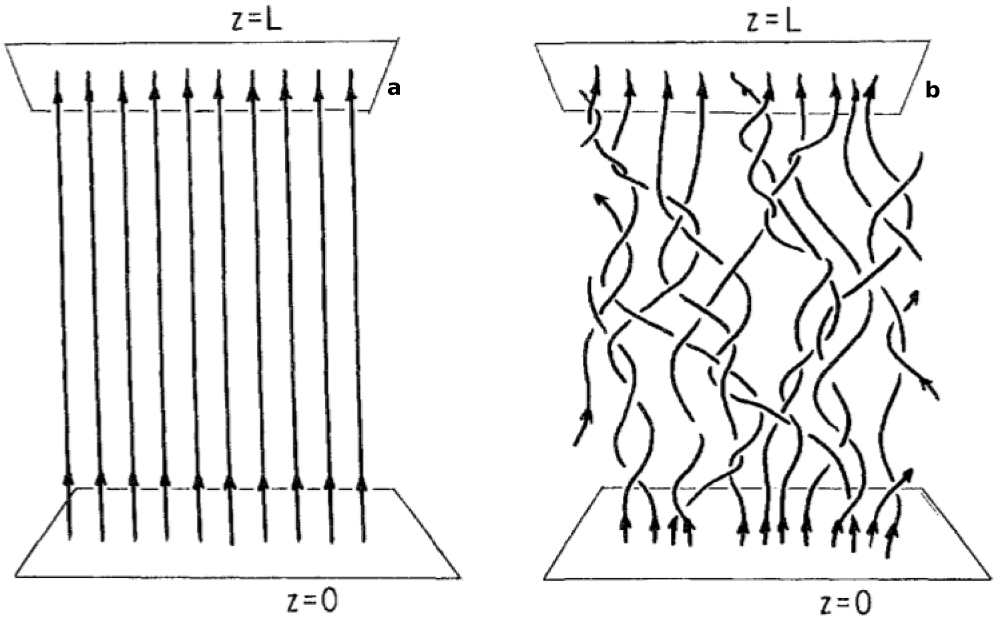

Figure 2.1: Panel a depicts the schematic of the field lines of a uniform continuous magnetic field. Panel b shows the interlaced field configuration after shuffling by the fluid motion imposed at the lower boundary $z = 0$. Adapted from [3].

expressing the fact that the torsion coefficient α is strictly constant along each magnetic field line. Based on this important property of the equilibrium magnetic field, we will now present the physical justification for the appearance of magnetic discontinuity in an ideal MHD.

Let us consider a uniform continuous magnetic field embedded in an incompressible inviscid infinitely conducting fluid, confined to the region $0 \leq z \leq L$ with infinite lateral extensions as shown in the panel a of Figure 2.1. We shuffle this initial magnetic configuration by imposing a smooth velocity field in the xy-plane at the boundary $z = 0$ while there is no fluid motion at the upper boundary $z = L$. It is to be noted that the magnetic field evolves under the flux-freezing condition. After some time the magnetic field lines will get sufficiently interlaced and have an arbitrary complex field topology, shown in the panel b of Figure 2.1. At this stage, we stop the fluid motion and allow the magnetic field to relax to the static equilibrium by keeping the ends of the field lines to be tied rigidly at the boundaries $z = 0, L$— ensuring the fixed topology of the interlaced magnetic field lines. A small viscosity— so small that the flux freezing condition is maintained— is included to the fluid to allow the relaxation. Also, the fluid pressure is maintained uniform at the boundaries, and hence uniform throughout the interior domain. Obviously, the initial interlaced magnetic field is not in equilibrium and, therefore, in response to the unbalanced Maxwell stresses the magnetic field evolves towards the static equilibrium. The relaxing fields will have to preserve their arbitrary field topologies as a consequence of flux freezing, thus, the existence of a smooth static equilibrium with an arbitrary field topology is contradictory, in general. The simple reason for this contradiction is that the static equilibrium posses a special field topology— that is of constant torsion along the real characteristics— while the field topology of the interlaced field is arbitrary. This contradiction with discrepancy in field topology can then be avoided if we permit discontinuity in the magnetic field. At the site of discontinuity any two real characteristics of the interlaced fields are compatible to adjust their individual torsions to that demanded by the real characteristics of the static equilibrium. Thus the appearance of discontinuities in magnetic fields is a natural tendency of magnetostatic equilibrium.

2.4 The Optical Analogy

The analogous behavior of the field lines of a potential magnetic field $-\nabla\phi$ to that of the optical rays in an index of refraction $\mid \nabla\phi \mid$ provides an elegant way to understand the discontinuity in magnetic fields [3, 32, 33, 34]. To appreciate this optical analogy, let us consider an equilibrium magnetic field $\mathbf{B}(\mathbf{r})$ whose projection on the surface S of $\nabla \times \mathbf{B}$ is $\mathbf{B}_s$ as depicted in the panel a of Figure 2.2. It is immediately seen from the equilibrium equation (2.3.3) that there is no component of the $\nabla \times \mathbf{B}$ across the field and hence the magnetic field $\mathbf{B}_s$ is curl-free. Therefore the magnetic field on the surface S can be written as

$$\mathbf{B}_s = -\nabla\phi_s \tag{2.4.1}$$

with ϕ_s as a scalar function. Since the magnetic field $\mathbf{B}_s$ is strictly confined to a surface S, the field pattern of $\mathbf{B}_s$ represents a magnetic flux surface. In order to understand the nature of the magnetic field $\mathbf{B}_s$ given by the relation (2.4.1), we consider for simplicity that the surface S lies in the xy-plane of a Cartesian coordinate system. It is to be noted that the surface S, in general, is a non-Euclidean two-dimensional space, but the mathematical procedure follows like the Cartesian coordinates. The trajectory of the field lines of $\mathbf{B}_s$ in the surface S is given by

$$\begin{aligned} B_s \frac{dx}{ds} &= -\frac{\partial \phi_s}{\partial x}, \\ B_s \frac{dy}{ds} &= -\frac{\partial \phi_s}{\partial y}, \end{aligned} \tag{2.4.2}$$

where s is the parameter along the field lines of $\mathbf{B}_s$. On squaring and adding the two relations given by the equations (2.4.2), we obtain

$$B_s{}^2 = (\nabla \phi_s)^2. \tag{2.4.3}$$

It is readily seen that the above equation (2.4.3) is analogous to the Eikonal equation of optics expressed as

$$n^2 = (\nabla \phi)^2, \tag{2.4.4}$$

with $n = n(x, y)$ as the index of refraction. Thus the trajectory of a field line in a medium with an index of refraction $\mid \mathbf{B}_s \mid$ behaves in a similar fashion to that of the path of an optical ray in a medium with index of refraction $n(x, y)$. That is to say the magnetic field lines stream in a medium with refractive index equal to $\mid \mathbf{B}_s \mid$.

To obtain the path of the optical rays, we use the Fermat's principle

$$\delta \int_1^2 B_s \, ds = 0, \tag{2.4.5}$$

where the extremum of the optical path length $B_s \, ds$, with $ds = \sqrt{dx^2 + dy^2}$, is evaluated on a parametric curve Γ represented by the coordinates $(x(s), y(s))$— with s as a parameter— in between the two fixed points 1 and 2 lying on the surface S. The resulting Euler equation reads as

$$\frac{y''}{\left(1 + y'^2\right)^{3/2}} = \frac{1}{\left(1 + y'^2\right)^{1/2}} \frac{\partial \ln B_s}{\partial y} - \frac{y'}{\left(1 + y'^2\right)^{1/2}} \frac{\partial \ln B_s}{\partial x}. \tag{2.4.6}$$

Here we have used the notations $y' = \frac{dy}{dx}$ and $y'' = \frac{d^2y}{dx^2}$. Now define a unit tangent vector along the curve Γ, i.e. the ray path, being represented by $\hat{\mathbf{e}}_s = \left[\frac{1}{\left(1+y'^2\right)^{1/2}}, \frac{y'}{\left(1+y'^2\right)^{1/2}}\right]$. Since the curvature of the ray path Γ is given by $\kappa = \mid \frac{d}{ds}\hat{\mathbf{e}}_s \mid$, therefore, utilizing the values for $\hat{\mathbf{e}}_s$, yields $\kappa = \frac{y''}{\left(1+y'^2\right)^{3/2}}$. Hence equation (2.4.6) for the ray path then becomes

$$\boldsymbol{\kappa} = \hat{\mathbf{e}}_s \times \nabla B_s, \tag{2.4.7}$$

expressing the fact that the field line or the ray path is concave toward a local maximum in the index of refraction $\mid \mathbf{B}_s \mid$. The concavity of the field lines then generates gap (panel a, Fig. 2.2) in the pattern of the field lines of $\mid \mathbf{B}_s \mid$ since the field lines pass around the localized maximum in the index of refraction $\mid \mathbf{B}_s \mid$, rather than through the localized maximum, so as to make the optical path length shortest. It is readily seen that a stack of flux surfaces then creates a hole (panel b, Fig. 2.2) in the flux surfaces extending along the thickness of the flux surfaces. Moreover the gap generated in the flux surfaces due to the bifurcation of the field lines lying on the flux surfaces, permits the otherwise separate fields on either side of the gap to come into contact through the gap. The intrusion

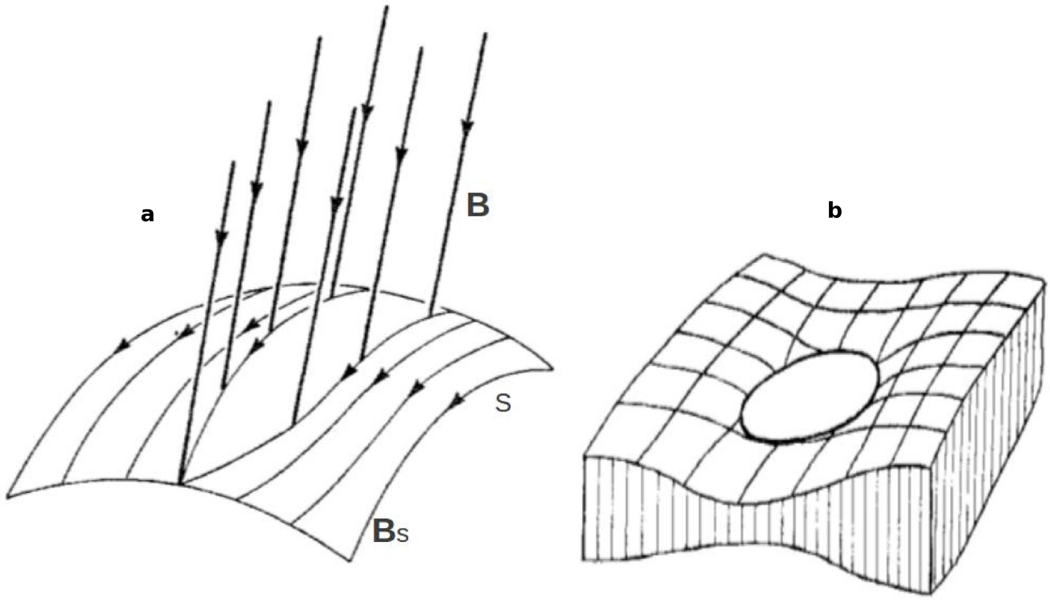

Figure 2.2: The projection $\mathbf{B}_s$ of the magnetic field $\mathbf{B}$ on the surface S is depicted in panel a. The enhanced local maximum in $\mid \mathbf{B}_s \mid$ then generates a gap in the flux surface onto which field lines of $\mathbf{B}_s$ lies. In a stack of such flux surfaces then create a hole— in which the field lines from other flux surfaces meet to permit discontinuity in magnetic fields, shown in panel b. Adapted from [3].

of fields from the separate regions are generally not parallel where they meet in the gap, so their contact in the gap creates a discontinuity in magnetic field.

2.5 Summary

In summary, we discussed the general criteria for the existence of plasma. Various theoretical models to describe dynamics and statics of plasma have also been presented. Utilization of different models is subjective to the physical problem under consideration. We discussed an important frozen-in property of magnetic field for an infinitely conducting fluid described by ideal MHD equations. The appearance of discontinuity is central to the mathematical nature of the partial differential equation. Utilizing the concept of the method of characteristics, it is shown that nonlinear hyperbolic partial differential equation has a natural tendency to develop discontinuity. We see that the characteristics associated with the magnetostatic equation are of mixed type, i.e., elliptic-hyperbolic in nature. The hyperbolic nature of these two equations then permit the formation of discontinuities. The generation of magnetic discontinuity in a static equilibrium is discussed in brief from physical point of view. The real characteristic of the magnetostatic equation represents the magnetic field line along which the torsion-coefficient remains constant. Under the flux-freezing condition, the magnetic topology is preserved, and, therefore, an arbitrary field topology in general cannot achieve a continuous static equilibrium. In other words, it is then essential that the magnetic field develops discontinuity in order to accommodate any arbitrary field topology in the static equilibrium. A more convenient tool to understand the magnetic discontinuity is based on the optical analogy. This analogy utilizes the fact that a potential field line traces exactly the similar path to that of an optical ray in an index of refraction given by the magnitude of the potential field. Therefore a localized maximum in the field magnitude then generates a gap in the flux surface. A stack of such surfaces produces a hole (the 3D extension of the gap). In general the non-parallel field lines lying on either side of the gap then come into direct contact in the gap, thereby forming discontinuity in magnetic field.

Chapter 3

Numerical Model

To numerically study the formation of magnetic discontinuity (MD), we need to solve the sets of the governing equations of ideal magnetohydrodynamics (MHD). For the purpose, we use the numerical model EULAG-MHD [35, 36], an extension of the general purpose hydrodynamical model EULAG (Eulerian-Lagrangian) [23]. As we have seen in the previous chapter 2 that the ideal MHD has a natural tendency to develop discontinuities in magnetic fields. Till now analytical techniques are not very matured, which can handle a discontinuous solution of ideal MHD, except for some simple cases. Such analytical difficulties then can be circumvented to some extent by utilizing numerical techniques. Although numerical algorithms have their own limitations— in that at most of them show spurious oscillations near the discontinuities, i.e., steep gradients of physical variables. However such oscillations can be mitigated by adopting high-resolution numerical algorithms like FCT (flux-corrected transport) [21]. The numerical model EULAG-MHD is based on a class of high-resolution numerical scheme MPDATA (multidimensional positive definite advection transport algorithm) [24], which is second order accurate in space and time. This accuracy in the numerical model is essential in order to resolve the magnetic discontinuities. From the model point of view, the work presented in this thesis is among the first applications of the numerical model EULAG-MHD to successfully capture the physics of discontinuity formation in magnetic fields. The preliminaries of the analytical and numerical details of the EULAG-MHD will be presented.

3.1 Analytical Formulation

The governing equations of an incompressible, thermally homogeneous magnetofluid with an infinite electric conductivity can be compactly written as

$$\frac{d\mathbf{u}}{dt} = -\nabla\pi' + \frac{1}{\mu_0\rho}\mathbf{B}\cdot\nabla\mathbf{B} + \nu\nabla^2\mathbf{u}, \tag{3.1.1}$$

$$\frac{d\mathbf{B}}{dt} = \mathbf{B}\cdot\nabla\mathbf{u} - \mathbf{B}\nabla\cdot\mathbf{u}, \tag{3.1.2}$$

$$\nabla\cdot\rho\mathbf{u} = 0, \tag{3.1.3}$$

$$\nabla\cdot\mathbf{B} = 0, \tag{3.1.4}$$

where π' subsumes both the density normalized fluid pressure and the magnetic pressure. The kinematic viscosity in the momentum balance equation is denoted by $\nu = \mu/\rho$, with μ representing the dynamic viscosity. The differential operator of the full derivative d/dt is defined as $d/dt \equiv \partial/\partial t + \mathbf{u}\cdot\nabla$, also called the Lagrangian derivative.

In the standard EULAG, the governing model equations are formulated in time dependent generalized/curvilinear coordinates

$$(\bar{t}, \bar{\mathbf{x}}) \equiv (t, \mathcal{F}(t, \mathbf{x})), \tag{3.1.5}$$

where the actual computations are performed. The physical domain $(t, \mathbf{x})$ where the actual problem is posed can be any stationary orthogonal (Cartesian, spherical and cylindrical) coordinate system [23, 37]. Assuming the above mapping or transformation to be invertible, the solution in the physical domain can then be obtained by the inverse transformation. EULAG-MHD employs a stationary subset of the transformation relation (3.1.5). The calculations carried out in this thesis implement the physical domain to be Cartesian, and, therefore both the computational space and the physical space are identical, i.e., $(\bar{t}, \bar{\mathbf{x}}) \equiv (t, \mathbf{x})$. Here we present the details of the EULAG-MHD in the general tensorial framework. In generalized coordinates the governing equations (3.1.1)-(3.1.4) then take the following form [35]

$$\frac{d\mathbf{u}}{d\bar{t}} = -\widetilde{\mathbf{G}}\overline{\nabla}\pi' + \frac{1}{\mu_0\rho}\overline{\mathbf{B}}^* \cdot \overline{\nabla}\mathbf{B} + \overline{\mathcal{D}}_{\mathbf{u}}, \tag{3.1.6}$$

$$\frac{d\mathbf{B}}{d\bar{t}} = \overline{\mathbf{B}}^* \cdot \overline{\nabla}\mathbf{u} - \mathbf{B}\frac{1}{\overline{\mathcal{G}}}\overline{\nabla} \cdot \overline{\mathcal{G}}\overline{\mathbf{u}}^*, \tag{3.1.7}$$

$$\frac{1}{\rho^*}\overline{\nabla} \cdot \rho^*\overline{\mathbf{u}}^* = 0, \tag{3.1.8}$$

$$\frac{1}{\overline{\mathcal{G}}}\overline{\nabla} \cdot \overline{\mathcal{G}}\ \overline{\mathbf{B}}^* = 0, \tag{3.1.9}$$

with total derivative operator $d/d\bar{t} = \partial/\partial\bar{t} + \overline{\mathbf{u}}^* \cdot \overline{\nabla}$, where $\overline{\mathbf{u}}^* = d\bar{\mathbf{x}}/d\bar{t}$ and $\overline{\nabla} \equiv \partial/\partial\bar{\mathbf{x}}$ representing respectively the contravariant velocity and the vector of partial derivatives in the computational space. A convenient transformation that relates directly the physical and the contravariant forms is given by

$$\overline{\mathbf{u}}^* = \widetilde{\mathbf{G}}^T\mathbf{u}, \quad \overline{\mathbf{B}}^* = \widetilde{\mathbf{G}}^T\mathbf{B}, \tag{3.1.10}$$

where the symbol $\widetilde{\mathbf{G}}$ denotes the renormalized elements of the Jacobian matrix. The term $\overline{\mathcal{D}}_{\mathbf{u}}$ in the momentum balance equation (3.1.6) denotes the viscous dissipation. In the continuity equation of (3.1.8), the generalized density $\rho^* = \rho\overline{\mathcal{G}}$ with $\overline{\mathcal{G}}$ representing the Jacobian of transformation [38] from physical space to computational space.

3.2 Numerical Approximations

Employing the continuity equation (3.1.8) and the solenoidality condition (3.1.9), equations (3.1.6)-(3.1.7) can be written in the flux-form Eulerian conservation laws [35, 37]

$$\frac{\partial}{\partial\bar{t}}(\rho^*\mathbf{\Psi}) + \overline{\nabla} \cdot (\rho^*\overline{\mathbf{u}}^*\mathbf{\Psi}) = \rho^*\mathbf{R} \tag{3.2.1}$$

with $\mathbf{\Psi} = (\mathbf{u}, \mathbf{B})^T$ denoting the vector of prognosed dependent variables, and $\mathbf{R}$ symbolizes the associated forcings on rhs terms of equations (3.1.6) and (3.1.7). In writing the above conservative form (3.2.1), the Lorentz force in (3.1.6) and the induction term in (3.1.7) are transformed via relations

$$\overline{\mathbf{B}}^* \cdot \overline{\nabla}\mathbf{B} = \frac{1}{\overline{\mathcal{G}}}\overline{\nabla} \cdot \mathcal{G}\overline{\mathbf{u}}^*\mathbf{B}, \quad \overline{\mathbf{B}}^* \cdot \overline{\nabla}\mathbf{u} = \frac{1}{\overline{\mathcal{G}}}\overline{\nabla} \cdot \mathcal{G}\overline{\mathbf{B}}^*\mathbf{u}. \tag{3.2.2}$$

Moreover, an ad hoc potential term $-\widetilde{\mathbf{G}}\overline{\nabla}\pi^*$ is added to the rhs of the induction equation (3.1.7)— in the spirit of hydrodynamic pressure fluctuations in the standard EULAG— to ensure the solenoidality of $\mathbf{B}$. Thus a general representation of the potential term can be viewed as $-\widetilde{\mathbf{G}}\overline{\nabla}\mathbf{\Phi}$ with $\mathbf{\Phi} \equiv (\pi', \pi', \pi', \pi^*, \pi^*, \pi^*)$.

Equation (3.2.1) is integrated using a nonoscillatory forward-in-time (NFT) algorithm with second-order accuracy in space and time, and, therefore can be written in a compact form as

$$\mathbf{\Psi}_i^n = \mathcal{L}E_i\left(\widetilde{\mathbf{\Psi}}, \widetilde{\mathbf{V}}^*, \rho^*\right) + 0.5\delta t\mathbf{R}_i^n \equiv \widehat{\mathbf{\Psi}}_i + 0.5\delta t\mathbf{R}_i^n, \tag{3.2.3}$$

where $\mathbf{\Psi}_i^n$ is the solution sought at the mesh point $(t^n, \mathbf{x}_i)$. The symbol $\mathcal{L}E_i$ denotes the NFT advection scheme MPDATA [23, 24, 37], and $\widetilde{\mathbf{\Psi}} \equiv \mathbf{\Psi}^{n-1} + 0.5\delta t\mathbf{R}^{n-1}$. Advecting the auxiliary variable $\widetilde{\mathbf{\Psi}}$ while combining $0.5\delta t(\mathbf{R}^{n-1}+\mathbf{R}^n)$ outside of $\mathcal{L}E_i$ then compensates for the first order error $\mathcal{O}(\delta t)$ proportional to the divergence of the advective flux of the source terms, i.e., $\overline{\nabla}\cdot\widetilde{\mathbf{V}}^*\mathbf{R}$. Centering in time of the advective momenta $\widetilde{\mathbf{V}}^* \equiv \rho^*\overline{\mathbf{u}}^*|^{n-1/2}$ that appears as an argument of $\mathcal{L}E_i$ is required to compensate for the first order error proportional to $\partial\overline{\mathbf{u}}^*/\partial\bar{t}$. To achieve the second order accuracy of the solution given by (3.2.3), it is sufficient to provide only a first order accurate estimate of $\overline{\mathbf{u}}^*$. The simplest choice is the linear extrapolation from $\overline{\mathbf{u}}^{*n-1}$ and $\overline{\mathbf{u}}^{*n-2}$ that also assures solenoidality of $\widetilde{\mathbf{V}}^*$, provided the solenoidality of $\rho^*\overline{\mathbf{u}}^*$ at earlier times.

The model template algorithm (3.2.3) is implicit for all prognosed dependent variables $\mathbf{u}, \mathbf{B}, \pi'$ and π^* for an inviscid system, because all principal forcing terms are unknown at n. Therefore a fixed point iteration of (3.2.3) can be viewed as

$$\mathbf{\Psi}_i^{n,\nu} = \widehat{\mathbf{\Psi}}_i + 0.5\delta t\mathbf{L}(\mathbf{\Psi})|_i^{n,\nu} + 0.5\delta t\mathbf{N}(\mathbf{\Psi})|_i^{n,\nu-1} - 0.5\delta t\widetilde{\mathbf{G}}\overline{\nabla}\mathbf{\Phi}|_i^{n,\nu}, \qquad (3.2.4)$$

where $\mathbf{R}$ is decomposed into a linear term $\mathbf{L}(\mathbf{\Psi})$, a nonlinear term $\mathbf{L}(\mathbf{\Psi})$ and a potential term $\widetilde{\mathbf{G}}\overline{\nabla}\mathbf{\Phi}$, with $\nu = 1, 2, ..., m$ numbers the iterations. By lagging behind the nonlinear term and performing algebraic manipulation facilitates the relation (3.2.4) to take a closed form for $\mathbf{\Psi}_i^{n,\nu}$, and reads as

$$\mathbf{\Psi}_i^{n,\nu} = [\mathbf{I} - 0.5\delta t\mathbf{L}]^{-1}\left(\widehat{\widehat{\mathbf{\Psi}}}_i - 0.5\delta t\widetilde{\mathbf{G}}\overline{\nabla}\mathbf{\Phi}|^{n,\nu}\right)\Big|_i, \qquad (3.2.5)$$

where $\widehat{\widehat{\mathbf{\Psi}}} \equiv \widehat{\mathbf{\Psi}} + 0.5\delta t\mathbf{N}(\mathbf{\Psi})|_i^{n,\nu-1}$ subsumes all the explicit terms. The dissipative forcing terms, say $\widetilde{\mathbf{R}}$, enter into the model algorithm (3.2.3) as a first order accurate estimate and hence are absorbed in the first argument of the operator $\mathcal{L}E_i$, i.e., $\widetilde{\mathbf{\Psi}} \equiv \mathbf{\Psi}^{n-1} + 0.5\delta t(\mathbf{R}^{n-1} + 2\widetilde{\mathbf{R}})$. Inserting the expressions (3.2.5) for the physical variables ($\mathbf{u}$, $\mathbf{B}$) into the transformation relations (3.1.10) yields the contravariant components of the prognostic variables $\mathbf{u}$ and $\mathbf{B}$, which are then subsequently plugged into relations (3.1.8) and (3.1.9) to produce elliptic equations for π' and π^*. Under appropriate boundary conditions for π' and π^*, these elliptic equations are solved iteratively using a preconditioned generalized conjugate residual (GCR) algorithm [39]. The iterations appearing in (3.2.5) and in the GCR solver are abbreviated as the "outer iteration" and the "inner iteration", respectively.

The numerical experiments [40, 41, 42] so far carried out using EULG-MHD to demonstrate the formation of magnetic discontinuities essentially employ the periodic boundary conditions. However, the problems attempted in chapter 7 to explore the MD formation deal with both periodic and open systems. For solving the problem with open system we have incorporated open boundary conditions in EULAG-MHD, which is a significant contribution to the numerical model and its advancement to a step further. To accommodate open boundary conditions we have written separate codes within the numerical framework of EULAG-MHD for adjustment of variables $(\mathbf{u}, \mathbf{B})$ at the boundaries— subject to the integrability condition [39], i.e., the balance of mass and magnetic fluxes over the computational domain— to ensure the solenoidality of $\mathbf{u}$ and $\mathbf{B}$ throughout the computations. Also the newly imposed boundary conditions lead to the rapid convergence of the GCR algorithm while maintaining its numerical accuracy, and therefore resulting in a substantial reduction in computation time.

3.3 Numerical Implementation

Here we outline the actual implementation of the numerical approximations (3.2.3) to solve the desired set of equations (3.1.6)-(3.1.9). Following (3.2.3), the iterations progress stepwise such that the most current update of a dependent variable is used in the ongoing step, wherever possible. A single outer iteration consists of two distinct blocks. The first block, referred as the hydrodynamic block, serves to integrate the momentum balance equation where the magnetic field enters the Lorentz force and is viewed as supplementary. This block ends with the final update of the velocity field via the solution of the elliptic equation for π'. The second block, referred as the magnetic block, uses the current updates of the velocities to integrate the induction equation. It ends with the final update of the magnetic field via the solution of the elliptic equation for π^*. Hereafter we drop the superscripts n as there is no ambiguity.

The hydrodynamic block begins with finding a first guess for the magnetic field at t^n by inverting the induction equation (3.1.7) in terms of the physical variables $(\mathbf{u}, \mathbf{B})$, as

$$\mathbf{B}_i^{\nu-1/2} = \widehat{\mathbf{B}}_i + 0.5\delta t \left[\left(\mathbf{B}^{\nu-1/2} \cdot \widetilde{\mathbf{G}} \overline{\nabla} \mathbf{u}^{\nu-1} \right) - \mathbf{B}^{\nu-1/2} tr\{ \widetilde{\mathbf{G}} \overline{\nabla} \mathbf{u}^{\nu-1} \} \right]_i , \quad (3.3.1)$$

where a second order estimate of the velocity is assumed as $\mathbf{u}^0 = 2\mathbf{u}^{n-1} - \mathbf{u}^{n-2}$ at $\nu = 1$. The superscript $\nu - 1/2$ symbolizes half of the single outer iteration. The term expressed by (3.3.1) contributes explicitly to the momentum balance equation (3.1.7), written as

$$\mathbf{u}_i^\nu = \widehat{\mathbf{u}}_i + \frac{0.5\delta t}{\mu_0 \rho}\left(\frac{1}{\overline{\overline{\mathcal{G}}}}\overline{\nabla} \cdot \mathcal{G}\overline{\mathbf{B}}^* \mathbf{B}\right)_i^{\nu-1/2} - 0.5\delta t\left(\widetilde{\mathbf{G}}\overline{\nabla}\pi'\right)_i^\nu, \tag{3.3.2}$$

which can be transformed to the contravariant velocity $\overline{\mathbf{u}}^*$ via the relation (3.2.2) for the velocity field. Plugging $\overline{\mathbf{u}}^*$ in the continuity equation (3.1.8) leads to the elliptic equation for π', of which the solution provides the updated contravariant velocity $\overline{\mathbf{u}}^*$ at $t^{n,\nu}$. The inverse transformation of (3.2.2) for the velocity field then returns back the physical velocity $\mathbf{u}^\nu$. This completes the hydrodynamic block of the single outer iteration.

The magnetic block begins with finding a new solution to (3.3.1) using the updated velocity. This, in turn, gives the estimate of the magnetic field $\mathbf{B}^{\nu-1/4}$ at t^n, expressed as

$$\mathbf{B}_i^{\nu-1/4} = \widehat{\mathbf{B}}_i + 0.5\delta t\left[\left(\mathbf{B}^{\nu-1/4} \cdot \widetilde{\mathbf{G}}\overline{\nabla}\mathbf{u}^\nu\right) - \mathbf{B}^{\nu-1/4} tr\{\widetilde{\mathbf{G}}\overline{\nabla}\mathbf{u}^\nu\}\right]_i, \tag{3.3.3}$$

where the superscript $\nu - 1/4$ denotes the iteration being a quarter away from the completion that is a single outer iteration. This magnetic field is being used in the induction equation (3.1.7) in order to write the closed form of magnetic field as

$$\mathbf{B}_i^\nu = \widehat{\mathbf{B}}_i + 0.5\delta t\left(\frac{1}{\overline{\overline{\mathcal{G}}}}\overline{\nabla} \cdot \mathcal{G}\overline{\mathbf{B}}^*|^{\nu-1/4}\mathbf{u}^\nu\right)_i - 0.5\delta t\left(\widetilde{\mathbf{G}}\overline{\nabla}\pi^*\right)_i^\nu. \tag{3.3.4}$$

Here only the last term is implicit while all other terms are subsumed into the explicit term of the solution. Utilizing the transformation relation (3.2.2) for the magnetic field and the solenoidal condition (3.1.9) then leads the closed form $\mathbf{B}^\nu$

to provide the elliptic equation for π^*, of which solution provides the updated contravariant magnetic field $\overline{\mathbf{B}}^*$ at $t^{n,\nu}$. The inversion transformation (3.2.2) for the magnetic field then returns back to the physical field $\mathbf{B}^\nu$. This completes the magnetic block and hence a single outer iteration.

3.4 Numerical Advection Scheme MPDATA

MPDATA is a class of high-resolution advection scheme— akin to Lax-Wendroff scheme— which is nonoscillatory, positive definite, sign preserving and second order accurate [24, 43, 44, 45]. This advection algorithm was developed by Smolarkiewicz in the early 1980's [43]. The underlying idea of MPDATA is to compensate the truncation error of the upwind/donor cell scheme in an iterative manner. The first iteration is a simple donor cell approximation which is positive definite and estimates the solution to a first order accuracy. The second iteration increases the accuracy of the calculation by estimating and compensating the truncation error of the first iteration, achieved by applying again the donor cell scheme to the truncated error terms. For this second iteration, the velocity is calculated from the field that is being advected and has no physical significance. These velocities are termed antidiffusive, or equivalently pseudo velocities. Further iterations can be executed to estimate the residual error of the previous iteration and approximately compensate it. This iteration may be performed an arbitrary number of times, leading to successively more accurate solutions of the advection equation. In the following, we illustrate the basic scheme of MPDATA.

To begin with, consider the one dimensional advection equation obtained by inserting $\rho^* = 1$ and $\mathbf{R} = 0$ in equation (3.2.1), taking the form

$$\frac{\partial \Psi}{\partial t} = -\frac{\partial}{\partial x}(u\Psi), \tag{3.4.1}$$

for the scalar variable Ψ with velocity u. The donor cell approximation to the advection equation (3.4.1) can be compactly written as

$$\Psi_i^{n+1} = \Psi_i^n - \left[F\left(\Psi_i^n, \Psi_{i+1}^n, U_{i+1/2}\right) - F\left(\Psi_{i-1}^n, \Psi_i^n, U_{i-1/2}\right)\right], \tag{3.4.2}$$

with flux function F defined by

$$F\left(\Psi_{i-1}, \Psi_i, U\right) = \Psi_{i-1}\left(\frac{U+ \mid U \mid}{2}\right) + \Psi_i\left(\frac{U- \mid U \mid}{2}\right), \tag{3.4.3}$$

where $U \equiv u\delta t/\delta x$ is the Courant number. The integer indices correspond to the center and the half integer indices are on the boundaries of the grid cells. Assuming u to be constant, a Taylor series expansion of the donor cell approximation (3.4.3) can therefore be written as

$$\frac{\partial \Psi}{\partial t} = -\frac{\partial}{\partial x}(u\psi) + \frac{\partial}{\partial x}\left(K\frac{\partial \Psi}{\partial x}\right), \tag{3.4.4}$$

where $K = \frac{(\delta x)^2}{2\delta t}(\mid U \mid - U^2)$. Thus the donor cell approximation (3.4.2) represents the advection equation (3.4.1) with the second order error (diffusive term of (3.4.4)). Hence one must compensate this second order error to improve the accuracy of the donor cell. This accuracy is achieved by estimation of the diffusion term in (3.4.4) with a donor cell approximation and then subtracting from (3.4.2). To proceed further, we write the diffusive error in the form of an advective flux as

$$\frac{\partial}{\partial x}\left(K\frac{\partial \Psi}{\partial x}\right) = \frac{\partial}{\partial x}\left(\frac{K}{\Psi}\frac{\partial \Psi}{\partial x}\Psi\right) = \frac{\partial}{\partial x}\left(v^{(1)}\Psi\right), \tag{3.4.5}$$

with $v^{(1)} \equiv \frac{K}{\Psi}\frac{\partial \Psi}{\partial x}$ representing the pseudo velocity. The superscript over v shows that it is the first approximation to subtracting the error. A first order estimate of the pseudo velocity in nondimensional form can be written as

$$V^{(1)}_{i+1/2} = \frac{2K}{\delta x}\frac{\Psi^{(1)}_{i+1} - \Psi^{(1)}_{i}}{\Psi^{(1)}_{i+1} + \Psi^{(1)}_{i}} = \left(\mid U \mid - U^2\right)\frac{\Psi^{(1)}_{i+1} - \Psi^{(1)}_{i}}{\Psi^{(1)}_{i+1} + \Psi^{(1)}_{i}}, \tag{3.4.6}$$

where $V^{(1)} \equiv v^{(1)}\delta t/\delta x$. Thus the compensation of the truncation error can be estimated in the second donor cell pass by subtracting the second order estimate Ψ^{n+1} from the first donor cell pass solution $\Psi^{(1)}$, and reads as follows

$$\Psi^{(2)}_i = \Psi^{(1)}_i - \left[F\left(\Psi^{(1)}_i, \Psi^{(1)}_{i+1}, V^{(1)}_{i+1/2}\right) - F\left(\Psi^{(1)}_{i-1}, \Psi^{(1)}_{i}, V^{(1)}_{i-1/2}\right)\right]. \tag{3.4.7}$$

The algorithm (3.4.7) preserves the sign of Ψ while maintaining the second order accuracy [24]. Also, the stability of the donor cell pass ensures the stability of the second pass as $\mid V \mid \leq \mid U \mid$. For a nonuniform physical velocity u, the pseudo velocity is not necessarily solenoidal and hence MPDATA algorithm may not preserve monotonicity [46]. This oscillatory behavior can then be circumvented by combining the flux-corrected transport (FCT) method with the MPDATA. The basic MPDATA formalism has a variety of extending options to enhance the accuracy and generality of the transport equations [44].

3.5 Merits of High-Resolution Numerics and the Physics of ILES

Astrophysical and geophysical fluids are associated with high Reynolds number and therefore contain a wide range of spatial and temporal scales. A numerical simulation that capture all the relevant physical scales of motion are termed as a direct numerical simulation (DNS). Resolving all the scales of flows is computationally expensive. An alternate way to circumvent this problem is to model only the large scales (the resolved scales) and filtering out the unresolved small scales by an explicit subgrid-scale (SGS) model— referred as large eddy simulation (LES). Moreover an unconventional strategy can be adapted viz rather than modeling the two separate scales, the effects of unresolved scales are incorporated implicitly through a class of nonlinear high-resolution numerical scheme. This is called the implicit large eddy simulation (ILES) [47]. The absence of explicit SGS models in the ILES approach then provides many practical advantages such as computational efficiency and ease of implementation.

Prior to 1970's the most challenging problem with numerical computation was the physically unrealizable solution near the developing sharp gradients of the advected flow variables. Although the first order numerical schemes like the upwind (donor-cell) method preserve monotonicity, despite that it suffers from the bizarre numerical diffusion resulting in flattening of the solution around the steep gradients of the physical variables [21]. On the other hand the second order numerical schemes like Lax-Wendroff become oscillatory— develop ripples or spurious oscillations— near the sharp gradients and hence do not preserve monotonicity [48]. In the early 1970's, a second order accurate monotonicity preserving numerical scheme— the flux-corrected transport (FCT) was developed by Boris and Book [49]. Later on, this FCT technique was further extended by Zalesak [50] to be applicable for a multidimensional systems. With the advent of such high-resolution numerical techniques, the numerical computations become more reliable and provide enough confidence to be used in interdisciplinary fields of science and engineering. Boris was first to recognize that the truncation errors of FCT algorithms serve as a SGS model— called the monotonically integrated LES (MILES) [51]. In general, this implicit property is applicable for all classes of high-resolution monotone numerical methods. MPDATA is one such method that has an inherent property of implicit dissipation, employed to model successfully the ILES of high Reynolds number geophysical flows [52, 53] as well as modeling of solar dynamo [35, 54, 55, 56, 57]. The simulations performed in this thesis to resolve the discontinuity of ideal MHD are based on the ILES property of MPDATA.

Moreover, analyzing and visualizing computational data sets are important aspects of any numerical simulation. NCAR Graphics (http://dx.doi.org/10.5065 /D6WD3XH5) is the traditional tool to analyze and visualize the data sets generated by both EULAG and EULAG-MHD. In our computations the size of the output data is enormously large, of the order of several gigabyte, which considerably degrade the performance of NCAR graphics. Therefore to enhance the capability of data processing, we have translated the simulation outputs to the desired format of other data analysis and visualization platforms, such as IDL and VAPOR, which handle the massive numerical data with great ease.

3.6 Summary

In summary, the general strategies for solving the governing equations of ideal magnetohydrodynamics using the numerical model EULAG-MHD is presented. EULAG-MHD modeling framework has been discussed briefly in generalized coordinates. EULAG-MHD is based on a second order accurate nonoscillatory advection scheme MPDATA. The numerics of basic MPDATA has also been discussed. The inherent property of implicit dissipation of MPDATA then provides the basis for ILES. The role of ILES is important to study the dynamics of discontinuity formation in ideal MHD.

Chapter 4

Dynamics of Discontinuity Formation: Present Status

In this chapter we highlight some of the major works so far carried out on the formation of magnetic discontinuities in a fluid with large electrical conductivity. We will present both the analytical and numerical works already done in this direction.

4.1 Analytical Study

In this section we show an example to demonstrate the formation of magnetic discontinuity through the analytical solution of magnetostatic equilibrium. For simplicity, the solution is obtained for a 2D field with a simple field topology [3, 58].

Considering an equilibrium magnetic field $\mathbf{B}_0$ confined in between $z = 0$ and $z = L$ of the two parallel conducting plates, Parker [7] shows using the series expansion that a perturbed magnetic field $\mathbf{B}$ led by a continuous deformation of the initial equilibrium magnetic field $\mathbf{B}_0$ cannot achieve a smooth equilibrium unless the perturbed field has some kind of symmetry or involves an ignorable co-ordinate, i.e. $\partial\mathbf{B}/\partial z = 0$. To demonstrate this general idea of Parker's theory, analytical solution is constructed by a continuous deformation of an equilibrium magnetic field. In the following we discuss the necessary mathematical procedure required to demonstrate the discontinuity formation.

In Cartesian geometry with x as an ignorable coordinate, a general magnetic field $\mathbf{B}$ can be expressed in terms of the flux function ψ as

$$\mathbf{B} = B_x(y,z)\hat{\mathbf{x}} + \hat{\mathbf{x}} \times \nabla\psi(y,z) \equiv B_x(y,z)\hat{\mathbf{x}} + \frac{\partial\psi}{\partial z}\hat{\mathbf{y}} - \frac{\partial\psi}{\partial y}\hat{\mathbf{z}}. \tag{4.1.1}$$

On plugging this field $\mathbf{B}$ into a force-free field satististifying the equation

$$(\nabla \times \mathbf{B}) \times \mathbf{B} = 0, \tag{4.1.2}$$

we obtain the Grad-Shafranov equation

$$\nabla^2\psi = -B_x\frac{dB_x}{d\psi} \tag{4.1.3}$$

with $B_x = B_x(\psi)$. The flux function ψ is constant along a field line and hence contours of ψ are the projections of field lines on the yz-plane. B_x is also constant along a field line since B_x is a function of ψ.

Now consider a force-free field, enclosed by the two conducting plates at $z = 0$ and $z = L$, with all field lines connecting one end plate to the other, and which is deformed continuously by imposing a footpoint displacement (or shear) Δx in the x direction. This Δx is related to the quantities ψ and B_x of eqution (4.1.3) given by the footpoint mapping from one end to the other. Therefore integrating the field line equation

$$\frac{dx}{ds} = \frac{B_x}{\mid \nabla\psi \mid}, \tag{4.1.4}$$

along a given field line from $z = 0$ to $z = L$ gives the footpoint displacement Δx as

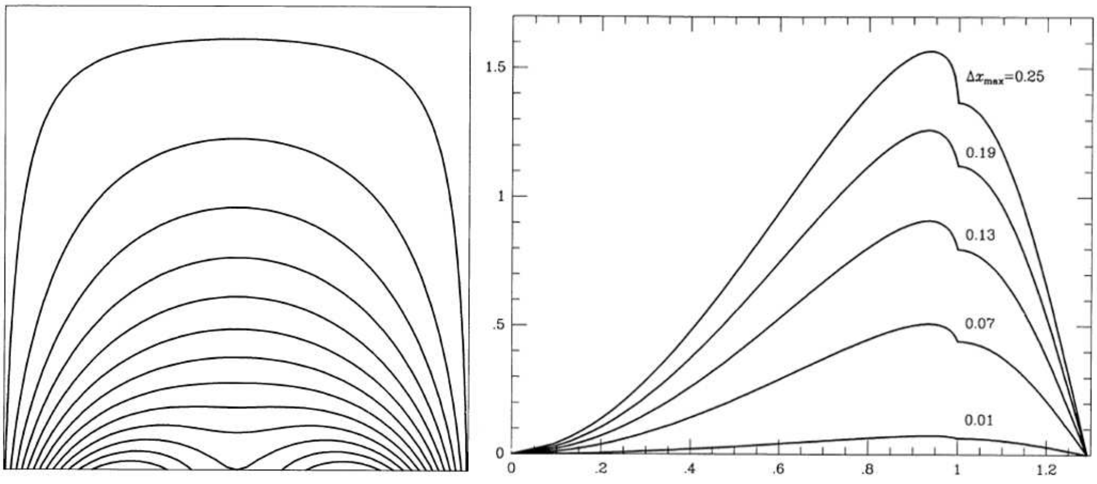

Figure 4.1: Left panel: potential magnetic field lines with separatrix $\psi = \psi^*$, which separates field lines of different connectivities. Right Panel: The plot is for $B_x(\psi)$ (ordinate) vs. the field line label, ψ (abscissa) for distinct values of the maximum shear Δx_{max}. Noticeable is the presence of discontinuity at the separatrix $\psi = \psi^* = 1$. Taken from [58].

$$\Delta x(\psi) = B_x(\psi) \left[\int_{z=0}^{z=L} \frac{ds}{\mid \nabla\psi \mid} \right]_{\psi}, \tag{4.1.5}$$

where ds and $\nabla\psi$ represent a line element and the field component in the yz-plane, respectively. The subscript symbolizes that the integration is carried out along a constant ψ contour. B_x is taken outside the integral since it is constant along a field line. Thus, the coupled equations (4.1.3) and (4.1.5) are solved simultaneously to get the desired solution subject to boundary conditons on ψ and to a specified $\Delta x(\psi)$ which, through equation (4.1.5) fixes the field topology. The resulting equilibrium solution then tells us whether the magnetic field is continuous or discontinuous.

Utilizing the above mathematical idea, we now illustrate the formation of discontinuity with a physical example discussed in [58]. Consider a quadrupolar potential magnetic field with $B_x = 0$ in a cartesian domain $-1/2 < y < 1/2$, $0 < z < 1$, shown in the left panel of Figure 4.1. We denote the separatrix as the field line ψ^* and assign the value of unity (separatrix is that field line below which there are two separate field lines connecting the two bipoles forming the quadrupolar structure) $\psi = \psi^* = 1$. For the given potential field and with a specified shear the integro-differential equation given by (4.1.3) and (4.1.5) can be solved iteratively to get the equilibrium solution. Calculations are carried out for different values of the maximum shear Δx_{max}. The corresponding solutions for $B_x(\psi)$ are plotted in the right panel of Figure 4.1 as a function of ψ. The plot shows that the field component B_x changes apruptly in the vicinity of $\psi = \psi^* = 1$, which is prominent for the maximum applied shear $\Delta x_{max} = 0.25$.

Several authors [6, 59, 60] have demonstrated the formation of magnetic discontinuity in a two-dimensional field of Cartesian geometry. The equilibrium solutions exhibiting discontinuities have also been obtained in spherical polar coordinates [61, 62]. Recent works of Janse & Low [63, 64, 65] successfully demonstrate the formation of magnetic discontinuities for both 2D and 3D fields. They deform the initial equilibrium magnetic fields by a simple compression/expansion of the domain under the frozen-in condition and then find the final equilibrium field under the prescribed boundary conditions. Thereafter, they do the footpoints mapping of the field lines for both the initial and final equilibrium field. They interprete that any change in footpoint mappings of the initial and final fields as due to the formation of magnetic discontinuities somewhere in the interior domain. The complete magnetostatic problem has also been addressed by Low [66, 67] to study the influence of pressure and gravity on the formation of magnetic discontinuities.

Parker's original idea that the magnetostatic equilibrium contains magnetic discontinuities generated considerable debate over the years because of the lack of rigorous mathematical proof, since the analytic solution of the integro-differential equation is, in general, possible only for a restricted sets of field topologies. This theory was first challanged by van Ballegooijen [68] and subsequently by many authors [69, 70, 71]. However, some flaws of these challanges are explained in references [72, 73, 74].

4.2 Numerical Study

The analytical demonstration of the discontinuity formation considers only the initial and the final states of the static equilibrium. Incorporating a complete dynamical evolution of the magnetic field analytically is a formidable task because of the inherently nonlinear nature of the MHD equations. For a better understanding of the discontinuity formation, an actual time dependent solution is required, which is doable using numerical methods.

Many numerical experiments [75, 76, 77] were carried out to demonstrate the formation of MDs in a fluid with large electrical conductivity. These experiments consider the initial magnetic field similar to Parker scenario of two parallel end plates; the magnetic field is then shuffled by a prescribed continuous velocity field over a certain time interval and then the fluid motion is stopped. The interlaced magnetic field is then allowed to relax towards the equilibrium. All these earlier numerical simulations are plagued by numerical diffusion and hence do not permit a long simulation run. Therefore, numerical techniques that preserve the high fidelity of frozen-in condition is required for a better demonstration of magnetic discontinuities.

In a recent numerical experiment Bhattacharyya *et al.* [40] successfully demonstrate the formation of magnetic discontinuity as the initial nonequilibrium magnetic field evolves towards the asymptotic equilibrium. This experiment has a novel feature of advecting the magnetic flux surfaces instead of the vector magnetic field. The advantage of this approach is to make the computation cost effective as well as easy to monitor the evolution of magnetic flux surfaces— which is rather a tedious job if we monitor the field lines. The general idea of this work is based on the fact that the intersection of two sets of Euler potentials (EPs), the flux surfaces, represent the magnetic field line. A general untwisted magnetic field $\mathbf{B}$ can be represented as a pair of Euler potentials [40, 78, 79] in the form

$$\mathbf{B} = W(\xi, \zeta)\nabla\xi \times \nabla\zeta, \tag{4.2.1}$$

where $W(\xi, \zeta)$ accounts for the field amplitude and is a function of the Euler potentials ξ and ζ. Following the induction equation, the evolution of these Euler potentials (flux surfaces) then yield the following advection equations

$$\frac{\partial \xi}{\partial t} + \mathbf{u} \cdot \nabla \xi = 0, \tag{4.2.2}$$
$$\frac{\partial \zeta}{\partial t} + \mathbf{u} \cdot \nabla \zeta = 0, \tag{4.2.3}$$

for ξ and ζ. Subject to an initial prescribed sets of Euler potentials $\xi(\mathbf{x}, t = 0)$ and $\zeta(\mathbf{x}, t = 0)$, equations (4.2.2)-(4.2.3) yield the evolution of Euler potentials. A magnetic field line is specified by a pair of constant values of ξ and ζ. For the choice of initial magnetic field in Cartesian coordinates ($-\pi < x < \pi, -\pi < y < \pi, -\pi < z < \pi$), Figure 4.2 depicts the evolution of a set of ζ flux surfaces located at constant plane $z = 0.58\pi$. The field line lies approximately on a constant z plane hence these flux contours represent the local magnetic field lines. The initial unbalanced force squeezes the fluid in between the positive and negative flux contours— the field reversal layer— resulting in outward sweeping and crowding of the outer ζ contours. The continuous deformation of these flux contours then develop two "necks" in the inner ζ contours at $t = 72$ due to asymmetry of the initial flux surfaces. Further squeezing of the fluid will eventually lead to the under-resolved scales at these locations of pinched contours. Subsequently, the numerical dissipation takes over and the resulting spurious magnetic reconnection then develops three distinct closed loops. This reconnection process can be suppressed if the frozen-in condition is rigorously maintained and in that situation the magnetic field becomes discontinuous across the entire field reversal layer. In other words, the numerical simulation resolves the formation of magnetic discontinuities till the threshold of the onset of magnetic reconnection as a result of under-resolved scales. In continuation of this work, Kumar *et al.* [41] investigated the formation of magnetic discontinuity through the evolution of Euler potentials for a twisted magnetic field.

Although the Euler potential representation is a powerful technique to demon-

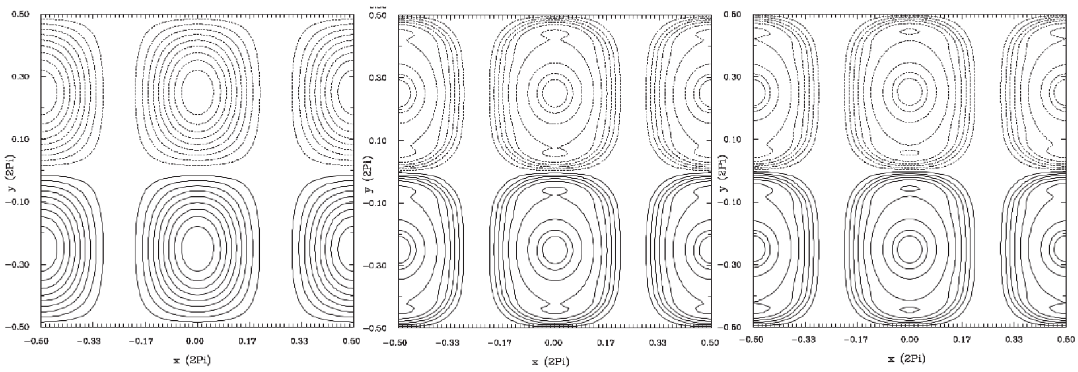

Figure 4.2: Time sequence of $z = 0.58\pi$ cross-sections of the ζ Euler surfaces at t = 0, 72, and 80 (from left to right). The respective positive and negative values are shown with solid and dashed contours with contour interval of 0.1. Noticeable is the formation of three distinct sets of closed loops (in the right end panel) through formation of magnetic discontinuities and their subsequent decay through numerical dissipation. Adapted from [40].

strate the formation of MDs, but its applicability is limited only to non-diffusive evolution. Therefore this particular technique is applicable only to successfully track the flux surfaces up to the formation of MDs and afterwards all the information of Euler potential get lost. To circumvent such difficulties, advection of the magnetic field is then useful to understand the dynamics of magnetic field after the formation of MDs.

Pontin & Huang [80] studied numerically the formation of magnetic discontinuities through volumetric deformation of magnetic field as proposed by Janse & Low [63]. They considered the same initial magnetic field as taken in [63]. However, their results show that MDs appear only when the initial magnetic field contain magnetic nulls (spatial locations where $\mid \mathbf{B} \mid= 0$), which is in contrast with the results of Janse & Low, which demonstrate that MDs develop even in absence of magnetic nulls. A similar kind of work, but with no formation of MDs have been found by Wilmot-Smith *et al.* [81]. In their numerical experiments, they constructed the initial braided magnetic field using analytical expression, however, such braided field can also be realized as the continuous deformation of an uniform magnetic field in Parker scenario. They relax the initial braided magnetic field with its preserved topology towards an asymptotic equilibrium. Their analyses show that the equilibrium does not contain magnetic discontinuities.

The above numerical experiments are in support as well as against of the formation of magnetic discontinuities as suggested by Parker. With results both in favor and against formation of MDs, further investigation is required to settle the issue of the formation of magnetic discontinuities in a fluid with large electrical conductivity.

4.3 Summary

In this chapter we discussed both the analytical and numerical aspects of discontinuity formation in a fluid with large electrical conductivity. This theory of MD formation first proposed by Parker based on magnetostatic equilibrium raised several questions for its validity due to lack of rigorous mathematical proof. Most of the analytical demonstrations of discontinuity formation are carried out primarily for two dimensional magnetic fields to have mathematically tractable solution. Since the analytical techniques do not address the full intermediate dynamics of the magnetic field, numerical methods are required. The numerical approach to demonstrate the formation of MD has a challenging job to maintain the frozen-in condition at very small spatial scale. Numerical experiments that preserve the field topology during the relaxation towards equilibrium demonstrate both presence and absence of magnetic discontinuities in the static equilibrium. Such diverse results of numerical experiments are in general pertinent to the initial field topology under consideration, and hence further numerical simulations are required to address the Parker theory of MD formation.

Chapter 5

Solar Corona as a Prototype Example

The Sun is the source of energy for life on the Earth. It also provides a laboratory to study the physics of other solar-like stars. The energy is generated at the core of the Sun through p-p chain reaction and transported to its surface through the process of radiation and convection, and then to the solar atmosphere. Figure 5.1 depicts the temperature and density distribution in the solar atmosphere. The lowest part of the atmosphere, called the photosphere, is relatively dense and opaque and emits mostly in the visible radiation. A rarer and a transparent region exists at the top of the photosphere, called the chromosphere. From the temperature distribution of the curve, it is seen that the temperature first decreases to a minimum value at the base of the chromosphere and then rises smoothly. Subsequently, there is a rapid enhancement in temperature from $\approx 10^4\ K$ to $\approx 10^6\ K$ over a very thin layer (transition region). The tenuous million-degree temperature component of the atmosphere is called the solar corona. The higher temperature of the solar corona is in general contradiction to the second law of thermodynamics that heat cannot be transferred from low temperature to high temperature. It is widely believed that the transfer of energy from solar surface to the corona is via the solar magnetic field, which, in turn, is generated through dynamo action in the convection zone of the Sun. However, the precise mechanism through which magnetic energy gets dissipated

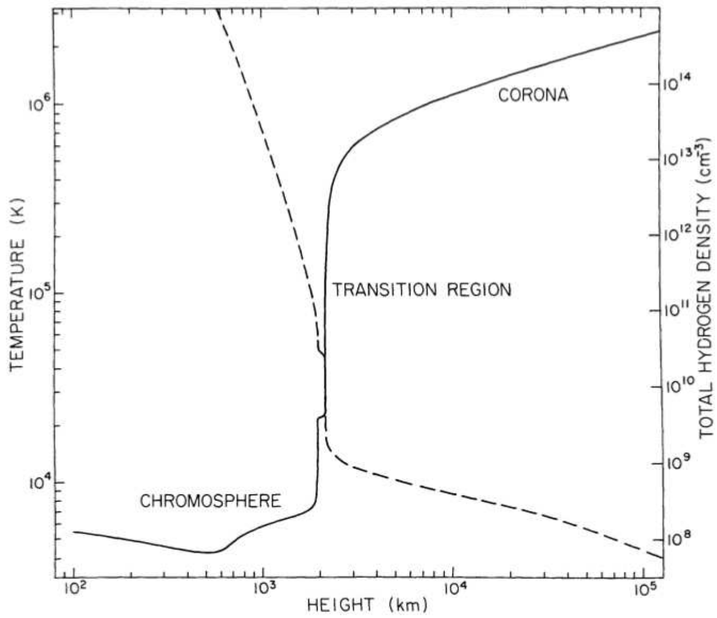

Figure 5.1: Variation of temperature and density with height in the solar atmosphere. Taken from [82].

in the corona is still debated [3]. The formation of magnetic discontinuity is a possible physical mechanism to dissipate the magnetic energy in the solar corona to maintain its million-degree temperature. Here we first survey the general physical conditions of the solar corona. Under these physical conditions, we discuss the possibility of the formation of magnetic discontinuity. Finally we highlight some of the consequences of magnetic discontinuities which are observed in the solar corona.

5.1 General Physical Properties of Corona

The white light emission from the solar corona is through the Thomson scattering of photospheric light by coronal electrons towards the observer, and is much fainter than the photospheric emission. Therefore the corona can be seen in white light only during a total eclipse of the Sun or by occulting the solar surface using a coronagraph. The spectrum of coronal emission lines, e.g. Fe_X and Fe_{XIV}, are indicative of temperature of the order of 10^6 K due to high ionization potentials of the respective ions of these coronal lines [83]. The solar corona emits X-rays

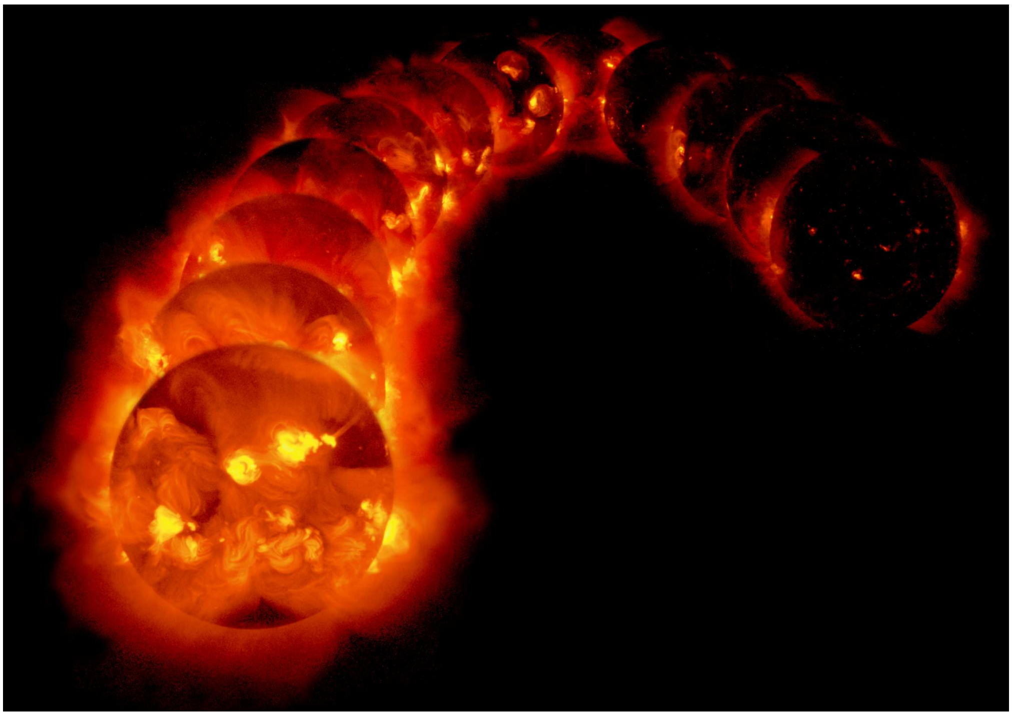

Figure 5.2: A sequence of X-ray images of the Sun, spanning from 1991 to 1995 (from left to right), taken from soft X-ray telescope (SXT) on board Yohkoh. (Image courtesy: Yohkoh)

because of its million-degree temperature. Thus the X-ray emission from the corona then provide an opportunity to observe the coronal features in X-ray regime. Figure 5.2 shows the images of the full Sun in X-ray taken by SXT (soft X-ray telescope) on board Yohkoh satellite. The first image (left) shows a variety of complex looplike structures from which X-ray emission originates. These emitting loops are generally associated with the underlying photospheric magnetic fields of active regions (sunspots), as can be inferred from the variation in X-ray intensity with the solar cycle (varying sunspots number), depicted in Figure 5.2.

From the X-ray image of the Sun it is evident that the solar corona is inhomogeneous and structured. The intensity of the X-ray emission is directly related to the strength of magnetic field. The strong X-ray emission is found in closed coronal loops connecting portions of the opposite magnetic polarity of the active regions. These closed loops appear brighter because they are hotter ($\approx 2 - 3 \times 10^6\ K$) as they confine the relatively higher density of coronal gas.

The life time of these loops are of the order of days to weeks. In the weak magnetic field regions, the coronal gas density is smaller and hence X-ray emission is negligible, resulting in the appearance of dark region (Fig. 5.2, first image from left) in the X-ray image of the Sun, where temperature is $\approx 10^6\ K$. This dark region, referred as the coronal hole, is associated with the open magnetic field lines along which coronal gas escapes into space and accelerates to reach speed of the order of 800 km/s, referred as the solar wind.

The above X-ray observations manifest the importance of solar magnetic fields. The existence of solar magnetic fields was first recognized by Hale from the Zeeman splitting of spectral lines in sunspots, the dark spots over the solar surface. The typical magnetic field of a large sunspot is approximately $2-3\times10^3\ G$. These sunspots generally appear in groups around the equatorial plane, and their magnetic polarities are oppositely directed in the northern and southern hemispheres of the Sun. Also, the reversals in the magnetic polarities take place at every 11 years, called the solar cycle. Though the photospheric magnetic field is routinely measured using the magnetograph which exploits the Zeeman effect. However, the precise measurement of magnetic field in the corona is difficult because the weak magnetic field produces a very low polarization signal. However, above the active regions with relatively strong magnetic field significant polarization signal can be achieved for certain coronal lines. Lin *et al.* [84] measured the coronal magnetic field by observing the longitudinal (line-of-sight) Zeeman effect of coronal emission lines Fe_{XIII} above active regions using the infrared spectropolarimeter. From the measurements of the weak Stokes V circular polarization profiles arising from the longitudinal Zeeman effect, they show the magnetic field strength to be $10-33\ G$. The coronal magnetic field has also been measured from radio observations using gyroresonance emission [85, 86, 87]. A more traditional method to measure the coronal magnetic field is through extrapolation of photospheric magnetic field using potential or force-free model [88, 89]. However these extrapolation techniques show discrepancies in measurements due to various assumptions in the theoretical model under consideration. Furthermore, over EUV observations reveal the signatures of coronal loop oscillations

Table 5.1: Physical properties of the corona

Region	Magnetic field (G)	Number density (m^{-3})	Temperature (K)
Active region	10^2	10^{16}	$2 - 3 \times 10^6$
Coronal hole	$5 - 10$	10^{14}	$1 - 1.5 \times 10^6$

[90, 91, 92]. These oscillations are associated with kink, sausage or torsional MHD modes. Based on oscillation frequency of these coronal loops, magnetic field strength in the corona has been calculated by several authors [91, 93, 94].

X-ray observations provide a way to measure coronal density by estimating emission measure, which is proportional to the line-of-sight integrated squared electron density [2]. In addition, coronal gas density can be measured from coronograph in white-light using the scattering by coronal electrons integrated along the line of sight. Radio observations are also used to determine the coronal density, since emission frequency is related with the electron density. Some physical properties of the solar corona are listed in Table 5.1. An important physical parameter is the plasma β, the ratio of the gas pressure to the magnetic pressure, which determines the relative importance of Lorentz force and the gradient of gas pressure. It is generally believed that in the solar corona, plasma $\beta < 1$. However Gary [95] found that the plasma β is not uniform throughout the solar atmosphere, but varies with height from the solar surface. Figure 5.3 shows the variation of plasma β with height above the two different active regions with magnetic field strengths 2.5×10^3 G (left curve of the shaded region) and 10^2 G (right curve of the shaded region). Since a direct measurement of coronal magnetic field is limited because of observational difficulties, and hence the magnetic field is derived from a theoretical model consistent with various observed data sets. In this model, a parametrized stretched potential field extrapolation technique is used to fit the extrapolated field lines with the observed coronal structures [95, 96]. Subsequently from the best fit of field lines, the magnetic field variation with height is then estimated. The plasma pressure is calculated from the density and temperature profiles which are obtained using emission measure and various

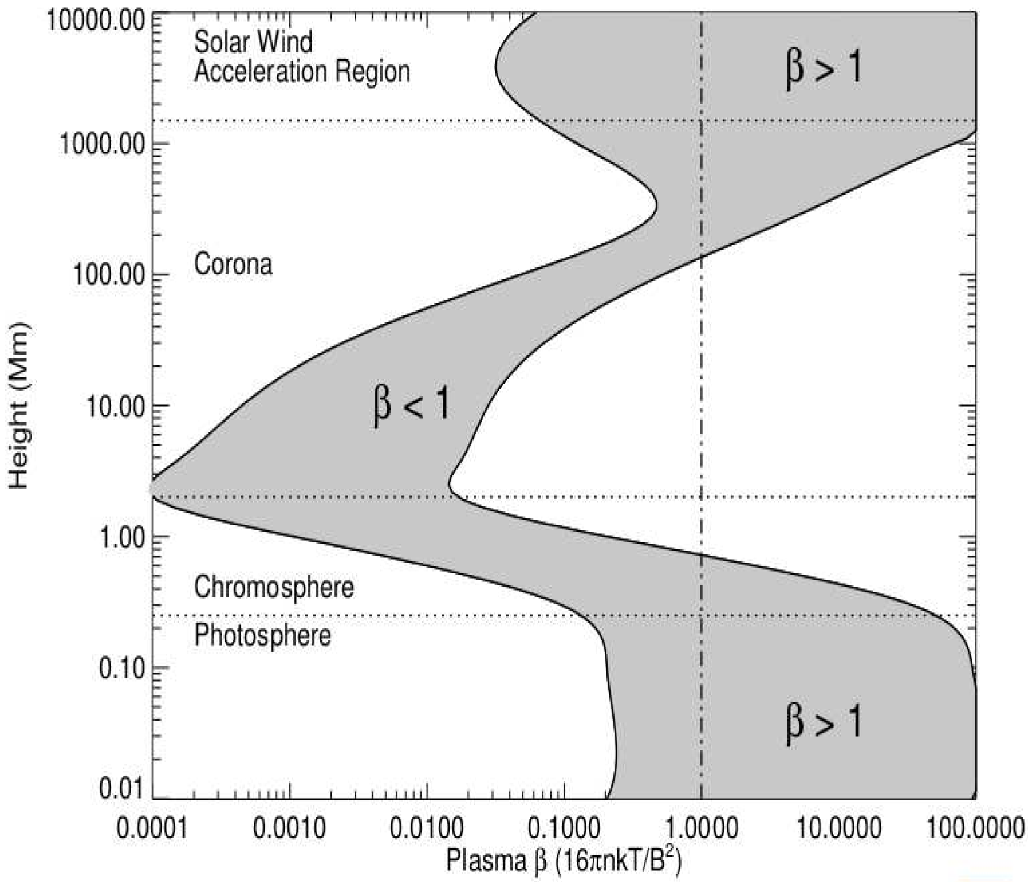

Figure 5.3: Variation of plasma β with height in the solar atmosphere corresponding to magnetic field strengths 2.5×10^3 G (left curve of the shaded region) and 10^2 G (right curve of the shaded region). The plot depicts the predominant magnetic effects in the middle corona where $\beta < 1$. Adapted from [95].

loop models. The resulting height dependent curves of plasma β, shown in Figure 5.3, is then calculated from the ratio of the plasma pressure and the magnetic pressure. It is seen that for the weak field strength the plasma $\beta < 1$ for the middle corona while the upper and the lower corona have plasma $\beta > 1$. The stronger field strength corresponds to the plasma $\beta < 1$. Based on these findings, it is then essential to consider the effects of varying plasma β while modeling the solar atmosphere. In particular, the extrapolation of magnetic field in the solar corona, generally, assumes the low beta plasma approximation. A more reliable extrapolation technique, therefore, must incorporate the whole range of plasma β.

5.2 Theoretical Modeling of Corona: Possibility of MD Formation

At the million degree Kelvin temperature, the coronal gas becomes fully ionized and behaves as a plasma. For such a highly ionized medium, the Spitzer resistivity [2] is $\eta_e \approx 10^{-7}\ \Omega - m$, which implies the coronal medium to have a large electrical conductivity. For a typical coronal loop of an active region with $L = 10^7\ m$, $B = 10^2\ G$, $N = 10^{16}\ m^{-3}$, the Lundquist number $S = 10^{13}$. Because of this high value of Lundquist number, the coronal medium can be modeled as an ideal MHD system where the magnetic field lines are frozen to the fluid elements of plasma. Thus coronal loops are basically the plasma structures confined by the coronal magnetic field lines. Also, the thermal conductivity of the coronal medium possess a high value, $\mathscr{K} \approx 10^5\ W/m - K$, and hence conducts the heat efficiently, especially along the magnetic field.

The elevated temperature of the corona than the lower atmosphere, drives the heat transfer from the corona to the lower atmosphere. The primary mechanism of heat loss from the corona is due to thermal conduction and the radiation. The typical values of the conductive and the radiative fluxes are listed in Table 5.2. The total loss of energy flux from the corona is therefore $\approx 10^7\ erg\ cm^{-2}\ sec^{-1}$. In order to balance this energy loss in the solar corona, some energy input is required. X-ray observations reveal that for an active region the energy flux required to maintain the coronal temperature against the conductive and radiative losses is $10^7\ erg\ cm^{-2}\ sec^{-1}$, providing sufficient heat input to balance the energy loss from the corona. Since the primary source of energy lies at the photospheric convective cells (granules), so the question is what is the mechanism through which the heat input is continuously supplied to the corona.

The convective motion excites various wave modes, for example, acoustic and MHD waves. It is believed that these waves propagate into the solar atmosphere and dissipate their energy to provide the required heat input to the solar corona. In the photosphere, the energy flux associated with an acoustic wave having sound speed v_s is $\mathscr{F}_{Acoustic} = (1/2)\rho v^2 v_s$, where ρ is the mass density of fluid

Table 5.2: Energy losses from the corona

Parameter	Active region	Coronal hole
Conductive flux ($erg\, cm^{-2}\, sec^{-1}$)	$10^5 - 10^7$	6×10^4
Radiative flux ($erg\, cm^{-2}\, sec^{-1}$)	5×10^6	10^4

and v is the velocity fluctuation associated with the convective motion [3]. For typical values of $\rho = 2 \times 10^{-4}\ kg/m^3$, $v = 10^3\ m/s$, $v_s = 10^4\ m/s$, gives $\mathscr{F}_{Acoustic} \approx 10^9\ erg\ cm^{-2}\ s^{-1}$. Thus, the acoustic wave carries sufficient energy flux to heat the corona. However, as this acoustic wave propagate upward in the solar atmosphere, the sound speed increases due to corresponding decrease in density. Nonlinear effects intervenes and acoustic wave develops into a shock wave, which gets dissipated in the chromosphere [97]. Therefore, though the acoustic wave, carries sufficient energy flux to begin with, it fails to reach at the coronal height [98].

The coronal magnetic field lines are rooted to the photospheric surface, and therefore the perturbation of these field lines by the convective motion then generates Alfven waves which propagate along the magnetic field lines. It is only the low frequency (large wavelength) Alfven wave which could reach to the corona, while that of the high frequency waves get dissipated at the lower atmosphere [99]. This Alfven wave mechanism then seems to be a plausible mechanism to supply the necessary heat input to solar corona. For a typical convective cell of length $l = 3 \times 10^5\ m$ with convective velocity $v = 10^3\ m/s$, gives a perturbation time scale $\tau = l/v \approx 300\ s$. In response to such convective perturbation, the coronal loop of an active region with Alfven speed $v_A = 10^6\ m/s$ then produces the wavelength of Alfven wave, $\lambda = v_A\ \tau = 3 \times 10^8\ m$. The longer wavelength of Alfven wave than the length of coronal loops ($\approx 10^7\ m$) then precludes the possibility of heating of such loops via dissipation of Alfven wave [3]. However, a smaller convective cells, if exists, may produce the suitable wavelength of Alfven wave that fits to the length of the coronal loop, and provide efficient heat input [100].

The difficulties associated with wave heating mechanisms then open up a new possibility of supplying the heat input to the corona through formation of magnetic discontinuities (MDs). To begin with, consider a typical coronal loop of an active region with length scale $L = 10^8\ m$ and Alfven speed $v_A = 10^6\ m/s$. For such a loop, the Alfven transit time $\tau_A = L/v_A = 10\ s$ which is much smaller than the convective perturbation time scale of $\approx 300\ s$, implying the quasi-static deformation [7] of coronal magnetic field lines. Further, the coronal field lines are rooted to the photosphere and hence the random swirling of convective motion interlaces the field lines. However the magnetic energy associated with such interlaced coronal magnetic field lines cannot be dissipated due to large electrical conductivity of the coronal medium. For example, the diffusion time scale over a length scale $L = 10^8\ m$ is $\tau_d = L^2/\eta = 10^{16}\ s$, with magnetic diffusivity $\eta = 1\ m^2\ s^{-1}$, which is much longer than the typical life time ($\approx 10^5\ s$) of the observed coronal loops. The diffusion time scale of the order of $10^5\ s$ may be achieved at small spatial scale of the order of $\approx 10^3\ m$, which is difficult to observe due to the limited resolution of telescopes. Alternately, the continuous interlacing of field lines build up Maxwell stresses that push any two portions of the field lines toward each other with declining spatial separation between them along with increasing magnetic field gradients. When the spatial separation reaches to the threshold value, the field gradient becomes large producing a structure with intense current density, called the current sheet (CS), which is dissipated via small, but finite Spitzer resistivity of the coronal plasma to produce efficient heat. However a true mathematical discontinuity in magnetic fields cannot be achieved due to large but finite electrical conductivity of coronal medium. Also at the location of the current sheets, field lines are highly diffusive and changes their field topology through magnetic reconnection. Therefore the formation of magnetic discontinuity and subsequent reconnection weakens the strength of initial interlaced field lines. The continued convective motion again interlaces the field lines to the threshold limit to generate new magnetic discontinuities and the onset of reconnection. This ubiquitous process of MD formation as a result of an interplay between the Maxwell stresses and the work done by the convective motion, may supply the continuous heat input to the million-degree corona.

A quantitative measure of the reconnection rate is required to understand the dissipation mechanism at the location of magnetic discontinuity. Parker [101] and Sweet [102] analytically estimated the reconnection rate for a two-dimensional geometry of magnetic field undergoing steady-state reconnection. Figure 5.4 depicts the schematic of two oppositely directed magnetic fields $\pm B_0$ embedded in an incompressible conducting fluid with density ρ and small electrical resistivity η_e. These oppositely directed field lines are pushed in the y-direction toward $y = 0$ line (where $B(x, 0) = 0$) with fluid speed v_{in} over a characteristic length $2L$. Because of small but finite electrical resistivity, a finite width 2δ of diffusion region (shaded area) develops in which field lines reconnect and outflow in the x-direction with fluid speed v_{out}. It is assumed that the reconnection process is quasi-steady. Under this condition the sum of the fluid pressure p and the magnetic pressure $B_0^2/2\mu_0$, across the diffusion region will remain constant. The pressing of the two regions of oppositely directed magnetic fields then enhances the fluid pressure at $y = 0$ line by an amount $B_0^2/2\mu_0$, followed by a simultaneous decline in magnetic pressure to zero at each side ($x = \pm L$) of the diffusion region. The imbalance in pressure between $x = 0$ and $x = \pm L$, expels the fluid out along x directions with speed $v_{out} = v_A \equiv B_0/\sqrt{\mu_0 \rho}$, where v_A is the Alfven speed. The gradient in magnetic field across the diffusion region of width δ generates electric current density, $j_z = B_0/\mu_0\delta$, which produces heat via Joule dissipation, $H = \eta_e \delta j_z^2 \equiv \eta_e B_0^2/\mu_0^2\delta$. Steady state condition demands that the energy loss through Joule dissipation must be balanced by the inflow of magnetic energy, $v_{in} B_0^2/2\mu_0$ into the diffusion region, yielding the relation

$$\eta = \frac{v_{in}\delta}{2} \quad , \tag{5.2.1}$$

where $\eta = \eta_e/\mu_0$ is the magnetic diffusivity. Further, since the fluid is incom-

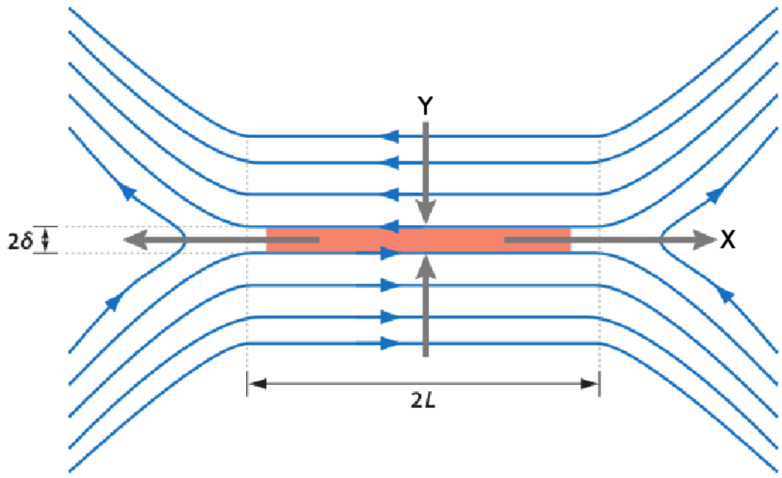

Figure 5.4: The schematic shows the geometry of two magnetic field configuration of Sweet-Parker reconnection. Oppositely directed magnetic fields are pushed toward each other over a length $2L$ and reconnect in a diffusion region (shaded area) of width 2δ. Taken from [20].

pressible, and hence the rate at which mass is entering into the diffusion is equal to the mass leaving the current sheet. This gives

$$v_{in} L = v_A \delta \quad , \tag{5.2.2}$$

The reconnection rate is the ratio of inflow speed to the outflow speed, which is obtained by using equations (5.2.1)-(5.2.2) as

$$\frac{v_{in}}{v_A} = \frac{\delta}{L} = \sqrt{\frac{2}{S}} \tag{5.2.3}$$

in terms of Lundquist number $S = v_A \ L/\eta$. Using the Sweet-Parker scenario of reconnection, the characteristic diffusion time scale for a typical coronal loop is $\tau_d = L/v_{in} \equiv L\sqrt{S}/\sqrt{2}v_A \approx 5 \times 10^7 \ s$, which is much smaller than that obtained using passive diffusion of solar corona, yet, larger than the life time of loops. In order to achieve a faster reconnection rate, Petschek [103] suggested that the length of the diffusion region must be smaller than that of Sweet-Parker scenario,

Table 5.3: X-ray classification of solar flares

Class	Energy flux ($erg\, cm^{-2}\, sec^{-1}$)
A	10^{-5}
B	10^{-4}
C	10^{-3}
M	10^{-2}
X	10^{-1}

and estimated the reconnection rate proportional to $1/log(S)$.

5.3 Some Observed Coronal Phenomena

The formation of magnetic discontinuity and subsequent reconnection have many consequences often observed in the solar atmosphere. In the following we discuss some of those consequences.

5.3.1 Solar Flares

Solar flares are sudden and explosive phenomena observed in the solar atmosphere, releasing energy of the order of $\approx 10^{28} - 10^{32}$ erg in a very short time scale of few minutes. The sudden release of energy is accompanied by the emission of waves over a wide electromagnetic spectrum, e.g. X-rays, white light, radio, and γ-rays. This radiation come from the corona and the chromosphere.

Solar flares are classified into different categories based on intensity of X-ray emission, by measuring the peak energy flux of X-rays in $1 - 8$ $\mathring{A}$ using the GOES satellite, listed in Table 5.3. Another classification of flares is based on the topological structures of the magnetic fields, e.g. compact flare and eruptive flare. Compact flare occurs in a single small coronal loop which remains unchanged in shape and position throughout the flare event, and is also known as the confined flare. Such a compact flare causes footpoint brightening in the loop when observed in H_α on the Sun's disk. Compact flares sustain for a short time duration. Eruptive flare mostly occurs in large coronal loops along the polarity

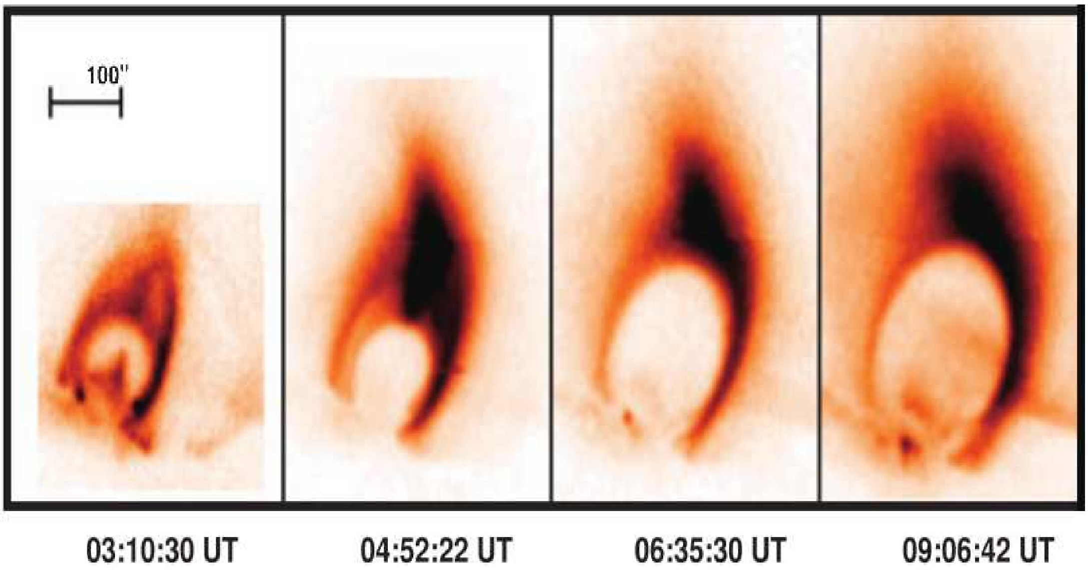

Figure 5.5: Sequence of soft X-ray images of a long-duration event (LDE) flare occurred on February 21, 1992, taken by soft X-ray telescope (SXT) on board Yohkoh satellite. Noticeable is the cusp-shaped loop structure with continuous increase in both height and footpoint separation. Adapted from [104].

inversion line (PIL) of the magnetic field. Such eruptive flares are observed in H_α image of the Sun as two bright ribbons on the solar disc, and are referred as the two-ribbon flares. These flares are associated with a rising arcade of post-flare loops. Eruptive flares sustain for a long time duration.

Multi-wavelength observations of a solar flare show mainly three phases of temporal evolution that are the preflare phase, the impulsive phase and the main phase. In the preflare phase, a relatively slow increase in radiation is observed which show the initial signature of the activity, also called the precursor phase. This phase may be caused due to some triggering mechanism located at the flaring site itself or away from it. The impulsive phase is characterized by rapid and intense emissions in hard X-rays, radio, γ-rays, EUV, and white-light. In this impulsive phase most of the energy stored in the magnetic field is released. In the main phase of a flare the energy released during the impulsive phase is transferred to other regions of the solar atmosphere. Also, topological changes in field lines are observed in this main phase of the flare. For example, post-flare loops are seen during the main phase of two-ribbon flare, rising upward slowly into the solar corona [105].

Figure 5.5 depicts the sequence of X-ray images of an eruptive flare of long-duration event (LDE). This flare was observed on February 21, 1992 by SXT on board Yohkoh. The significant feature seen in this flare is the cusp-shaped loop structures. Moreover the apparent height of the cusp-shaped loop and the distance between the footpoints of the loop increases continuously [106]. This observation is a signature of the formation of magnetic discontinuities and their subsequent reconnection that may have occurred above the cusp-shaped loop.

5.3.2 Solar Prominences

Prominences are relatively cool and dense plasma structures that are suspended in the solar atmosphere. They are commonly observed in H_α above the solar limb. The same structures appear dark when seen against the solar disk, and is known as filaments. They are always found above the polarity inversion lines (PILs) or neutral lines separating opposite polarities of the photospheric magnetic field.

There are primarily two types of prominences— active and quiescent. The active region prominences are found in the neighborhood of the active regions where magnetic field is strong, while the quiescent prominences are located in the vicinity of quiet regions where magnetic field is weak.

Prominences/filaments mostly appear as curtains of vertical thread-like structures. These vertical threads connect the horizontal long axis of the prominence to the photosphere. The long axis of the prominence is known as the spine and those vertical threads are called the barbs. Figure 5.6 shows an H_α image of the prominence above the solar limb [107]. In this image the horizontal long axis and vertical threads of plasma structures are clearly visible.

Now the crucial question is how prominences form and support the dense plasma in the solar atmosphere. It is believed that prominences are dipped magnetic structures where the upward Lorentz force support the dense plasma against gravity [108, 109]. A twisted magnetic flux rope is widely accepted model for the prominence because its helical field lines provide support for the dense plasma of the prominence [110, 111, 112]. Magnetic reconnection is a

Figure 5.6: Prominence observed in H_α from Big Bear Solar Observatory (BBSO). Taken from [107].

possible mechanism to generate such dipped and helical magnetic structures [113, 114, 115].

5.3.3 Solar Tornadoes

Solar tornadoes are rotating vertical magnetic structures observed in the solar atmosphere. These structures basically appear as funnel-shaped due to the helical geometry of magnetic field lines. Solar tornadoes have close resemblance with terrestrial tornadoes but caused by completely different physical mechanism [116].

There are various physical processes that can lead to the formation of solar

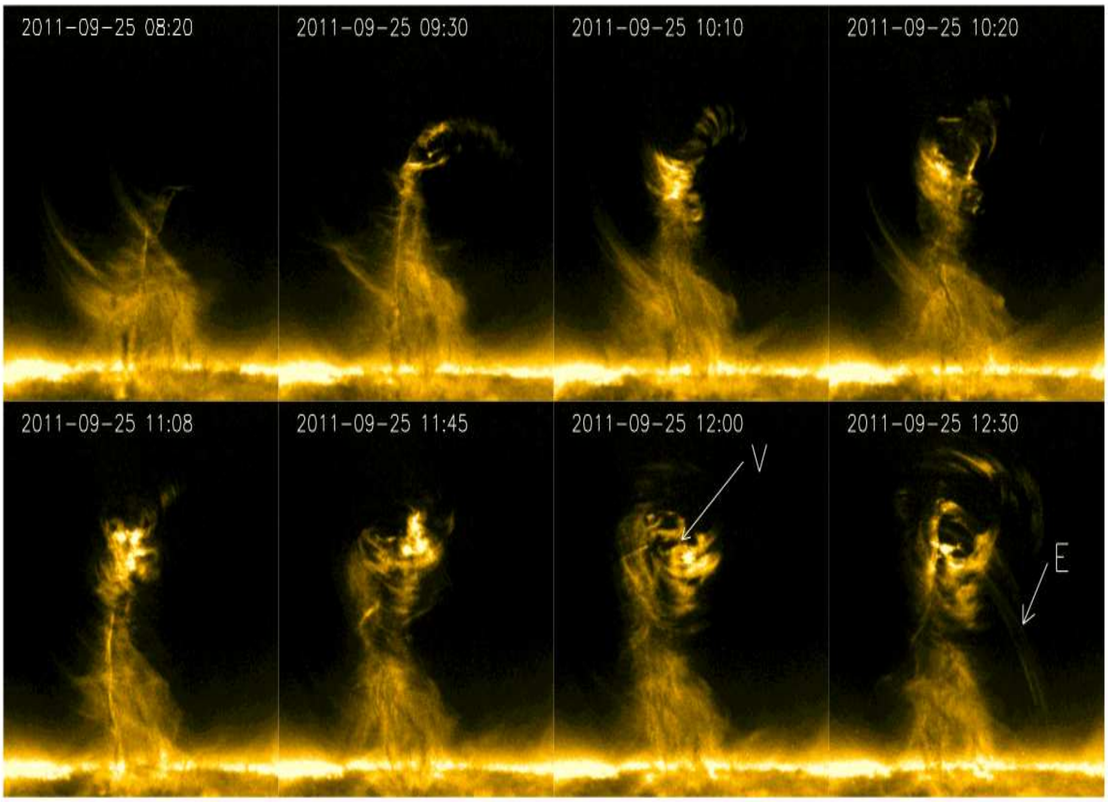

Figure 5.7: Temporal evolution of a solar tornado observed in 171 $\mathring{A}$ using AIA/SDO for approximately four hours. Counterclockwise rotation of helical structures can be noticed. Adapted from [117].

tornadoes. The role of photospheric vortex flows in generating tornado has been investigated by Wedemeyer-Böhm *et al.* [118]. The expansion of prominence cavity may also generate tornado-like motion [116, 117, 119, 120]. The possible role of magnetic reconnection in generation of solar tornadoes has been discussed [117]. Figure 5.7 shows the temporal evolution of a solar tornado observed on September 25, 2011 by AIA instrument on board SDO in 171 $\mathring{A}$ wavelength. The event starts with a narrow helical structures in which material is upwelling into the coronal cavity, possibly caused due to upward expansion of the prominence. These helical structures rise and fall back along curved trajectories, indicating that the motions are along curved magnetic field lines. The swirling motions of material around the prominence suggests the presence of helical magnetic fields, which becomes prominent after 9:30 UT. A helix-like structure with few turns can be seen at 10:10 UT. The sudden appearance of a similar tightly wound helix is observed at about 11:08 UT, and a less tightly wound helix is apparent at 11:45 UT. At 12:00 UT, a tangled helix at the top of the tornado shows a complex structure. In such a tangled structure, marked with symbol V, reconnection may take place. As a result of this reconnection, apparent downflows, marked with symbol E, are observed at 12:30 UT.

5.3.4 Coronal Mass Ejections

Coronal mass ejections (CMEs) are explosive expulsions of large amount of plasma and magnetic field from the solar corona into interplanetary space. CMEs are often observed with a coronagraph in white light. Figure 5.8 displays a time sequence of white-light images, taken from the coronagraph on board the NASA Solar Maximum Mission (SMM) satellite [121]. The CME originates from a preexisting helmet streamer that slowly rises and expands to break the looplike structures, leading to an eruption with an expulsion of huge mass ($\approx 10^{15}\ g$) at a speed of the order of 500 km/s. The CME has a three-part structure— a bright frontal loop, a dark cavity, and a bright core— that can be clearly seen in the panel c of Figure 5.8. Moreover, the three part structure of the CME can be identified with the bright dome, the dark cavity and the quiescent prominence of the pre-eruption helmet streamer [122]. The cavity appears dark because of the low plasma density, which is surrounded by a strong magnetic field.

Magnetic reconnection plays a crucial role in driving the CME. It is widely believed that the cavity magnetic field is associated with the twisted magnetic flux rope, which is fully detached from the lower atmosphere [122]. Such twisted flux rope is surrounded by an arcade of bipolar closed and open field lines rooted to the solar surface. The magnetic flux rope may become unstable by some means, e.g. loss of equilibrium or magnetic reconnection, resulting in rise of the flux rope which lifts the mass in the leading front and forces the closed bipolar fields of the frontal loop to open up by stretching. Magnetic reconnection occurs in stretched field lines, which provides extra magnetic free energy to the rising flux rope, leading to an explosive rise of the flux rope to drive CME.

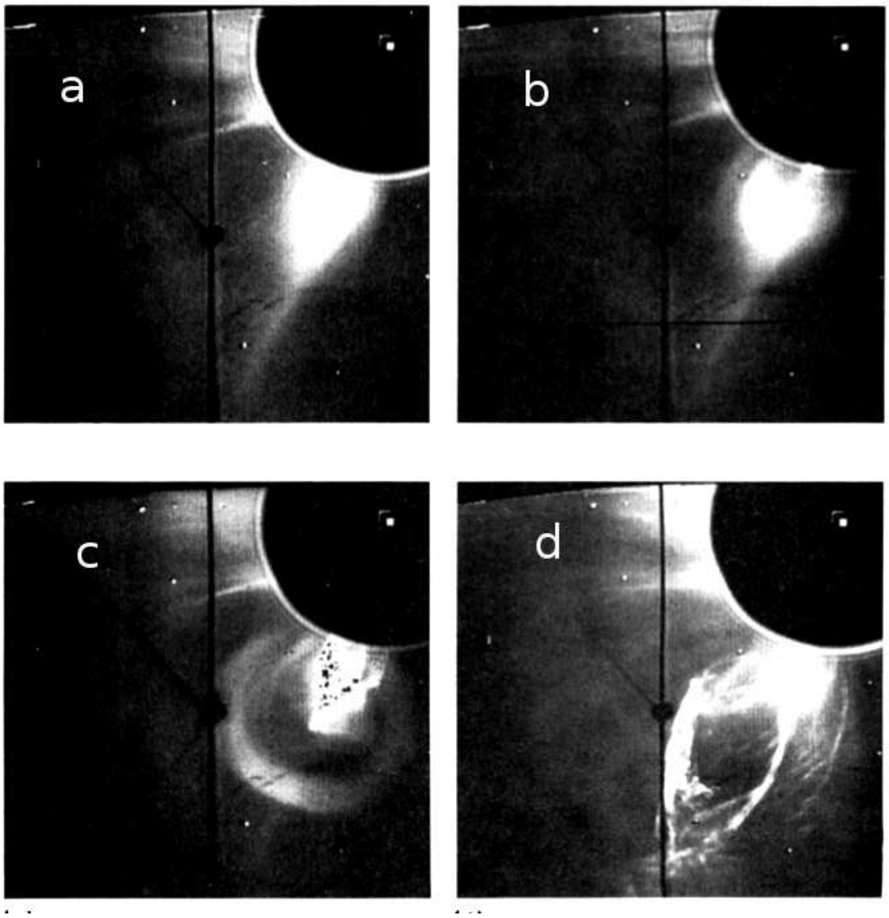

Figure 5.8: CME observed in white light on 18 August 1980 at (a) 10:04 UT, (b) 11:43 UT, (c) 12:15 UT, and (d) 13:09 UT, using the NASA Solar Maximum Mission (SMM) coronograph. The images display the three-part structure of the CME and its initiation and eruption. Taken from [121].

Simultaneously, the open stretched field lines below the flux rope gets reclosed as a result of reconnection.

5.4 Summary

The large but finite electrical conductivity of the solar corona provides a unique laboratory where the underlying physics of magnetic discontinuities can be understood in detail. In this chapter we discussed the general physical properties, like temperature, density and magnetic field, of the solar corona. The million degree temperature of the solar corona is an outstanding problem since a long time. We highlighted some of the possible heating mechanism that can maintain the corona to its million degree temperature. Acoustic wave which carries sufficient energy flux gets dissipated in the chromosphere before reaching to the solar corona. Alfven wave can reach to the coronal height, but is difficult to dissipate in the solar corona. We discussed the possibility of the formation of magnetic discontinuities under coronal conditions. Magnetic discontinuities develop as a result of quasi-static deformation of coronal magnetic fields. Some of the observed coronal phenomena which manifests the consequences of the formation of magnetic discontinuities and their subsequent reconnection, are presented.

Chapter 6

Equilibrium as a Result of Discontinuity Formation

In the previous chapter we have seen that the continuous interlacing of the coronal magnetic fields or loops in response to convective motion builds up Maxwell stresses. These magnetic stresses push the field lines close enough to create magnetic discontinuities. The subsequent reconnection results in quasi-static equilibrium. This equilibrium is further perturbed by convective motions and the same process repeats to evolve the magnetofluid towards the terminal or final states of equilibrium. Such an ongoing dynamical process that always settles the magnetofluid to its terminal state of equilibrium is called relaxation [123].

Under the large electrical conductivity of the coronal medium, the relaxation of coronal magnetic field dissipates the magnetic energy whereas the magnetic field lines remain frozen to the fluid elements to a good approximation. Thus the lowering of magnetic energy subject to constraints of flux-freezing is fundamentally similar to the mathematical problem of variational calculus where an integral is minimized subject to the constraint of another integral [123]. It turns out that the terminal equilibrium can be analytically obtained by formulating a suitable variational problem.

In this chapter we first introduce the variational principle to obtain the equilibrium using single-fluid MHD for an isolated system. The equilibrium so obtained is the linear force-free field with zero plasma β [124]. However, we have seen in the previous chapter that finite plasma β exists in the solar corona [95]. Incorporating such finite β in the equilibrium may not be possible using the single-fluid MHD. The reason is that the invariant associated with fluid velocity of single-fluid MHD has the same decay rate to that of the minimizer under consideration, and therefore the variation problem cannot be constructed [125]. Such difficulties are circumvented by adopting the invariants obtained using two-fluid plasma model [125, 126]. We develop a variational problem to obtain the equilibrium for an open system like the solar corona using two-fluid plasma model. Finally, we explore some of the topological features of the equilibrium magnetic fields.

6.1 Single-fluid Equilibrium

In this section we use the methods of variational calculus to obtain the equilibrium for an isolated system using the single-fluid MHD. Before proceeding further, let us look at the concept of magnetic helicity.

6.1.1 Magnetic Helicity

In an ideal magnetofluid, the field lines are frozen to the fluid elements and hence the linkage or connectivity of field lines is preserved. Such linkage of field lines is referred as the magnetic topology. A quantitative measure of the linkage of field lines is given by the magnetic helicity [127]

$$K = \int_V \mathbf{A} \cdot \mathbf{B} \, d\tau, \tag{6.1.1}$$

where $\mathbf{A}$ is the vector potential for the magnetic field $\mathbf{B}$, satisfying $\mathbf{B} = \nabla \times \mathbf{A}$. The integral is taken over the whole volume of interest, i.e. all field lines lie inside the volume V. This closed volume integral is a necessary requirement for helicity to be gauge invariant, and hence a physically meaningful quantity. To see this, the integral (6.1.1) under the gauge transformation $\mathbf{A} \rightarrow \mathbf{A} + \nabla\chi$, where

χ is a scalar quantity, becomes

$$
\begin{aligned}
K' &= \int_V (\mathbf{A} + \nabla\chi) \cdot \mathbf{B} \; d\tau \\
&= \int_V \mathbf{A} \cdot \mathbf{B} \; d\tau + \int_V \nabla \cdot (\chi \mathbf{B}) \; d\tau \\
&= K + \int_S \chi \mathbf{B} \cdot \hat{\mathbf{n}} \; dS,
\end{aligned}
\tag{6.1.2}
$$

where the Gauss-divergence theorem has been employed to convert the volume integral to the surface integral for the second term on the right hand side. Since all the field lines are enclosed within the volume, the normal component of $\mathbf{B}$ vanishes over the boundary S, i.e. $\mathbf{B} \cdot \hat{\mathbf{n}} = 0$. Thus $K' = K$; the magnetic helicity is gauge invariant.

For an open system where $\mathbf{B} \cdot \hat{\mathbf{n}} \neq 0$, i.e. the field lines penetrate the boundary, the expression (6.1.1) for the magnetic helicity becomes gauge dependent. Berger & Field [128] introduced the concept of relative magnetic helicity K_{rel} by subtracting the helicity of a reference field $\mathbf{B}_{ref}$, having the same distribution of $\mathbf{B}$ on the boundary surface S, given by

$$
K_{rel} = \int_V \mathbf{A} \cdot \mathbf{B} \; d\tau - \int_V \mathbf{A}_{ref} \cdot \mathbf{B}_{ref} \; d\tau. \tag{6.1.3}
$$

Here the reference vector potential $\mathbf{A}_{ref}$ is defined as $\mathbf{B}_{ref} = \nabla \times \mathbf{A}_{ref}$. The above representation of relative helicity is gauge invariant as suggested by Berger & Field [128] and Finn & Antonsen [129].

6.1.2 Formulation of the Variational Problem

In order to formulate a variational problem for finding the equilibrium state, we consider an isolated (or closed) magnetofluid with large electrical conductivity having low β value, i.e. magnetic forces dominate over all other forces. In such a system the magnetic energy W_M decay faster than the magnetic helicity K, and therefore methods of variational calculus can be employed to construct a suitable variational problem.

To begin with, let us first calculate the decay rate of magnetic helicity K to be written as

$$\frac{dK}{dt} = \int_V \left(\frac{\partial \mathbf{A}}{\partial t} \cdot \nabla \times \mathbf{A} + \mathbf{A} \cdot \nabla \times \frac{\partial \mathbf{A}}{\partial t} \right) d\tau. \tag{6.1.4}$$

Using vector identities and the relation $\mathbf{E} = -\nabla\phi - \partial\mathbf{A}/\partial t$, equation (6.1.4) takes the form of

$$\frac{dK}{dt} = \int_V \left[-2\mathbf{E} \cdot \mathbf{B} - \nabla \cdot \left(2\phi\mathbf{B} + \mathbf{A} \times \frac{\partial \mathbf{A}}{\partial t} \right) \right] d\tau. \tag{6.1.5}$$

On employing the Gauss-divergence theorem, this expression becomes

$$\frac{dK}{dt} = \int_V -2\mathbf{E} \cdot \mathbf{B}\, d\tau - \int_S \left(2\phi\mathbf{B} + \mathbf{A} \times \frac{\partial \mathbf{A}}{\partial t} \right) \cdot \hat{\mathbf{n}} dS, \tag{6.1.6}$$

where the second integral on the right hand side is taken over the surface S of the volume V. This integral vanishes since the field lines do not penetrate the surface S, and therefore

$$\frac{dK}{dt} = -2 \int_V \mathbf{E} \cdot \mathbf{B}\, d\tau. \tag{6.1.7}$$

Using Ohm's law, $\mathbf{E} + \mathbf{u} \times \mathbf{B} = \eta_e \mathbf{J}$, equation (6.1.7) can be written as

$$\frac{dK}{dt} = -2\eta_e \int_V \mathbf{J} \cdot \mathbf{B}\, d\tau. \tag{6.1.8}$$

Thus magnetic helicity is a conserved quantity for an ideal MHD as $\eta_e = 0$.

Now consider the decay rate of magnetic energy W_M, written as

$$
\begin{aligned}
\frac{dW_M}{dt} &= -\int_V \frac{\mathbf{B}}{\mu_0} \cdot (\nabla \times \mathbf{E})\; d\tau \\
&= -\int_V \left[\frac{1}{\mu_0}\nabla \cdot (\mathbf{E} \times \mathbf{B}) + \eta_e J^2\right]\; d\tau \\
&= -\int_V \eta_e J^2\; d\tau - \int_S \frac{1}{\mu_0}\left(\mathbf{E} \times \mathbf{B}\right) \cdot \hat{\mathbf{n}} dS \\
&= -\eta_e \int_V J^2\; d\tau,
\end{aligned}
\tag{6.1.9}
$$

where surface integral vanishes since the field lines are enclosed within the volume V. Thus for an ideal MHD ($\eta_e = 0$), the magnetic energy is also a conserved quantity like the magnetic helicity. However, this ideal limit is only of mathematical interest, and is not realized in practice. We have already seen that the generation of magnetic discontinuity in a magnetofluid with large electrical conductivity is associated with an intense electric current density $\mid \mathbf{J} \mid$. Therefore from relations (6.1.9) and (6.1.8), it is evident that the decay rate of magnetic energy is faster than that of magnetic helicity, and hence variational problem can be constructed with magnetic helicity as an invariant of motion. Thus the terminal state of equilibrium is obtained by solving the following variational equation

$$
\delta\left[W_M - \alpha K\right] = \delta\left[\int_V \frac{B^2}{2\mu_0}\; d\tau - \alpha \int_V \mathbf{A} \cdot \mathbf{B}\; d\tau\right] = 0, \tag{6.1.10}
$$

with α as an undetermined Lagrange multiplier [124]. Variation with respect to $\mathbf{A}$ gives the following equation

$$
\nabla \times \mathbf{B} = \alpha \mathbf{B}. \tag{6.1.11}
$$

This is the force-free equation (the Lorentz force $\mathbf{J} \times \mathbf{B} = 0$) with constant α and zero fluid velocity. Magnetic fields satisfying equation (6.1.11) are called Taylor states or Woltjer-Taylor states in honor of the pioneering work by J. B. Taylor

[124] and L. Woltjer [130]. This relaxation theory has profound applications in Laboratory plasmas to predict the equilibrium states [131]. Heyvaerts & Priest [132] extended the Taylor theory for an open system like the solar corona to explain the coronal heating problem. Nandy *et al.* [133] have studied the possible signature of Taylor-like relaxation process in the magnetic fields of flare-productive solar active regions.

6.2 Two-fluid Equilibrium

The single-fluid equilibrium obtained in the previous section is static force-free with zero plasma β. However, as we have discussed in the previous chapter that the solar atmosphere has nonuniform distribution of plasma β— i.e. only the middle corona has low β while the upper and lower corona have $\beta > 1$. Furthermore, mass motion of coronal plasma has been observed [134]. These observations along with the long-lived [135, 136] structures of coronal loops motivate us to incorporate the flow in the terminal states of equilibrium. To achieve this, two-fluid plasma model is adopted. We set up the variational problem for an open system like the solar corona to obtain the terminal states of equilibrium with flow. Before we proceed further let us first introduce the concept of generalized helicity obtained using the two-fluid plasma model for both isolated and open systems.

6.2.1 Generalized Helicity

Recalling the two-fluid momentum balance equation (2.1.2) from chapter 2, which, in absence of collision terms, reads as

$$m_\alpha n_\alpha \left[\frac{\partial \mathbf{u}_\alpha}{\partial t} + (\mathbf{u}_\alpha \cdot \nabla)\mathbf{u}_\alpha\right] = -\nabla p_\alpha + q_\alpha n_\alpha \left(\mathbf{E} + \mathbf{u}_\alpha \times \mathbf{B}\right). \tag{6.2.1}$$

Where $\alpha \equiv e, i$, denotes the fluid species, i.e. electrons and ions. Using the expression $\mathbf{E} = -\nabla\phi - \partial\mathbf{A}/\partial t$ and vector identities, this can be written as

$$m_\alpha n_\alpha \left[\frac{\partial \mathbf{u}_\alpha}{\partial t} + \nabla\left(\frac{u_\alpha^2}{2}\right) - \mathbf{u}_\alpha \times (\nabla \times \mathbf{u}_\alpha)\right]$$
$$= -\nabla p_\alpha - q_\alpha n_\alpha \left[-\nabla\phi - \frac{\partial \mathbf{A}}{\partial t} + \mathbf{u}_\alpha \times (\nabla \times \mathbf{A})\right]. \tag{6.2.2}$$

After rearranging terms, we have

$$\frac{\partial}{\partial t}(m_\alpha \mathbf{u}_\alpha + q_\alpha \mathbf{A}) - \mathbf{u}_\alpha \times [\nabla \times (m_\alpha \mathbf{u}_\alpha + q_\alpha \mathbf{A})]$$
$$= -\nabla\left(\frac{m_\alpha u_\alpha^2}{2} + q_\alpha \phi\right) - \frac{\nabla p_\alpha}{n_\alpha}. \tag{6.2.3}$$

Now defining the canonical momentum to be $\mathbf{P}_\alpha = m_\alpha u_\alpha + q_\alpha \mathbf{A}$, equation (6.2.3) can be written as

$$\frac{\partial \mathbf{P}_\alpha}{\partial t} + (\nabla \times \mathbf{P}_\alpha) \times \mathbf{u}_\alpha = \nabla h, \tag{6.2.4}$$

where all the terms on the right hand side of the equation (6.2.3) has been subsumed into the scalar h. We designate the canonical vorticity as $\mathbf{\Omega}_\alpha = \nabla \times \mathbf{P}_\alpha = m_\alpha \boldsymbol{\omega}_\alpha + q_\alpha \mathbf{B}$, where $\boldsymbol{\omega}_\alpha = \nabla \times \mathbf{u}_\alpha$ is the fluid vorticity. On taking the curl of equation (6.2.4) gives

$$\frac{\partial \mathbf{\Omega}_\alpha}{\partial t} + \nabla \times (\mathbf{u}_\alpha \times \mathbf{\Omega}_\alpha) = 0. \tag{6.2.5}$$

This evolution equation for canonical vorticity $\mathbf{\Omega}_\alpha$ is analogous to that of the induction equation (2.1.12) of ideal MHD. Thus the canonical vorticity field lines are frozen to the fluid elements of plasma in spirit of the flux-freezing of magnetic field lines. This is a more generalized version of the flux-freezing since it accounts for the mass flow. To quantify the linkage of generalized vorticity field line, we define the generalized helicity [125, 126]

$$K_\alpha^{G^{iso}} = \int_V \mathbf{P}_\alpha \cdot \mathbf{\Omega}_\alpha \, d\tau, \tag{6.2.6}$$

for an isolated system. It is to be noted that the helicity associated with the electron is simply the magnetic helicity due to negligible electron mass.

The generalized helicity for an open system [137, 138] can be expressed as

$$K_\alpha^G = \int_V \mathbf{P}_\alpha \cdot \mathbf{\Omega}_\alpha \, d\tau - \int_V \mathbf{P'}_\alpha \cdot \mathbf{\Omega'}_\alpha \, d\tau, \tag{6.2.7}$$

where the primed variables $\mathbf{P'}_\alpha$ and $\mathbf{\Omega'}_\alpha$ are similar to the corresponding unprimed variables except that their constituting vectors $\mathbf{u'}_\alpha$ and $\mathbf{A'}$ are the reference fields which differ from $\mathbf{u}_\alpha$ and $\mathbf{A}$ inside the volume of interest and may be the same or different outside, depending on the topology of the magnetic field exterior to the volume of interest. Under the gauge transformations $\mathbf{A} \rightarrow \mathbf{A} + \nabla\chi$ and $\mathbf{A'} \rightarrow \mathbf{A'} + \nabla\chi$, where χ is an arbitrary gauge, the relation (6.2.7) takes the following form

$$K_\alpha^{G'} = K_\alpha^G + \int_S q_\alpha \chi \left[\mathbf{\Omega}_\alpha - \mathbf{\Omega}'_\alpha\right] \cdot \hat{\mathbf{n}} dS. \tag{6.2.8}$$

where the surface integral is over the region of interest. It is immediately seen from the above expression (6.2.8) that the generalized helicity defined by equation (6.2.7) is gauge invariant provided the boundary condition

$$(\mathbf{\Omega}_\alpha - \mathbf{\Omega}'_\alpha) \cdot \hat{\mathbf{n}} = 0, \tag{6.2.9}$$

is obeyed at all points on the surface S.

6.2.2 Formulation of the Variational Problem

In order to construct the variational problem for an open system like the solar corona, we consider Cartesian geometry with $z = 0$ plane representing the solar surface whereas positive half-plane $z \geq 0$ corresponds to the solar corona. We also consider the periodic boundaries in the x and y directions. With this, the generalized helicity expressed by equation (6.2.7) along with the boundary condition (6.2.8) is a suitable choice for the coronal magnetic field, where the region of interest is the positive half-plane $z \geq 0$.

Since the coronal magnetofluid has large electrical conductivity, the formation of magnetic discontinuities and subsequent reconnection converts magnetic energy into heat and kinetic energy. Also, the coronal medium has large fluid Reynolds number [2] and hence an intense vorticity is generated at small spatial scales which is dissipated by viscosity [139]. Because of the dissipation of both magnetic and kinetic energies, the total energy

$$W_T = \int_V \left[\frac{B^2}{2\mu_0} + \frac{\rho_i u_i^2}{2}\right] \, d\tau, \tag{6.2.10}$$

is an appropriate minimizer to formulate the variational problem. Here we have assumed an electron-proton magnetofluid with constant density and neglected the electron mass. It is also to be noted that the total energy is a positive definite quantity and hence has a well defined lower bound.

A comparison of the decay rates of total energy W_T given by equation (6.2.10) and the generalized helicity K_α^G given by equation (6.2.7) can be carried out by calculating their respective decay rates as follows

$$\frac{dW_T}{dt} = -\eta_e \int_V J^2 \, d\tau - \mu \int \mid \nabla \times \mathbf{u}_i \mid^2 \, d\tau, \tag{6.2.11}$$

$$\frac{dK_\alpha^G}{dt} = -\eta_e \int_V \mathbf{J} \cdot \mathbf{\Omega}_\alpha \, d\tau + \mu \int_V \mathbf{\Omega}_\alpha \cdot \nabla^2 \mathbf{u}_\alpha \, d\tau. \tag{6.2.12}$$

It is readily seen from the above expressions (6.2.11)-(6.2.12) that the decay rate of total energy varies with the spatial scale L as L^{-2} while that of generalized helicities vary as L^{-1}. Intuitively for small spatial scale, the total energy decays faster than the generalized helicities of electrons and ions. Thus the generalized helicities corresponding to electrons and ions can be treated as invariants of motion. Therefore the terminal states of equilibrium is obtained by solving the variational equation

$$\delta\left[W_T + \sum_{\alpha=i,e} \lambda_\alpha K_\alpha^G\right] = 0, \tag{6.2.13}$$

with λ_α as undetermined Lagrange multipliers corresponding to the fluid species. After plugging the respective values in the above expression and taking the first order variation of $\mathbf{A}$ and $\mathbf{v}$, which are independent of each other, we obtain the following sets of Euler-Lagrange equations

$$\nabla \times \mathbf{B} + (\lambda_i + \lambda_e)\mathbf{B} + \lambda_i \nabla \times \mathbf{u} = 0, \tag{6.2.14}$$

$$\mathbf{u} + \lambda_i \nabla \times \mathbf{u} + \lambda_i \mathbf{B} = 0. \tag{6.2.15}$$

This two-fluid equilibrium state is more general than that of single-fluid equilibrium (6.1.11), because it couples both the plasma flow velocity and the magnetic field. Eliminating $\mathbf{u}$ in favor of $\mathbf{B}$ from equations (6.2.14)-(6.2.15), gives the equation for magnetic field as

$$\nabla \times \nabla \times \mathbf{B} + \frac{\lambda_i \lambda_e + 1}{\lambda_i} \nabla \times \mathbf{B} + \frac{\lambda_i + \lambda_e}{\lambda_i} \mathbf{B} = 0. \tag{6.2.16}$$

The solution of this equation lead to magnetic field structures, which contain more information than that of the linear force-free equation (6.1.11).

6.2.3 Equilibrium Solutions: 2D & 3D

To solve equation (6.2.16) let us expand $\mathbf{B}$ in terms of Chandrasekhar-Kendall (C-K) eigenfunctions [140] as

$$\mathbf{B} = \sum_{j=1,2} \gamma_j \mathbf{Y}_j, \tag{6.2.17}$$

where

$$\nabla \times \mathbf{Y}_j = \alpha_j \mathbf{Y}_j, \tag{6.2.18}$$

On normalizing $\mathbf{B}$ with γ_1, the magnetic field can be represented as

$$\mathbf{B} = \mathbf{Y}_1 + \gamma \mathbf{Y}_2, \tag{6.2.19}$$

where $\gamma = \gamma_2/\gamma_1$. The eigenvalues α_j of equations (6.2.18) represent the force-free parameters and the γ denotes the non force-free parameter, which defines the deviation of the magnetic field $\mathbf{B}$ from the force-free state. In Cartesian geometry a convenient representation for C-K eigenfunction is

$$\mathbf{Y}_j = \nabla \times (\phi_j \hat{\mathbf{e}}_y) + \frac{1}{\alpha_j} \nabla \times \nabla \left(\phi_j \hat{\mathbf{e}}_y\right), \tag{6.2.20}$$

where $j = 1, 2$, and ϕ_j is a three dimensional scalar function and $\hat{\mathbf{e}}_y$ is an unit vector in the y direction. Substitution of the above representation in equations (6.2.18) yields the well known Helmholtz equations

$$\nabla^2 \phi_j + \alpha_j^2 \phi_j = 0, \tag{6.2.21}$$

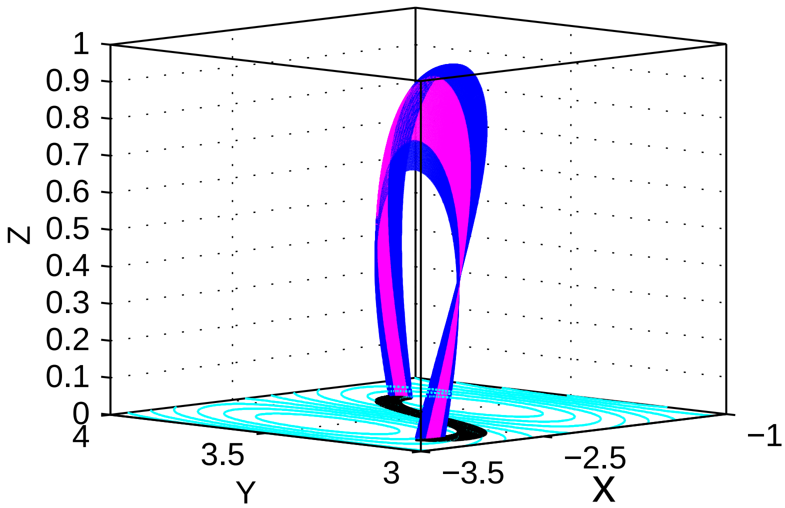

Figure 6.1: Three dimensional magnetic ribbons for a non force-free state with $\gamma = 0.25$ and $\alpha = 3.7$. The projection on the xy plane represents a forward sigmoidal structure.

Since the magnetic field must decay at infinite distance away from the solar surface, we assume an exponentially decaying solution in the z direction. For a two dimensional (2D) magnetic field with y symmetry, ϕ is given by

$$\phi_j(x, z) = \cos\left(x\sqrt{k_j^2 + \alpha_j^2}\right) exp(-k_j z), \tag{6.2.22}$$

Substituting this expression in equation (6.2.20) and using equation (6.2.19), the magnetic field components are obtained as

$$B_x = (1 + \gamma) \cos\left(x\sqrt{1 + \alpha^2}\right) exp(-z), \tag{6.2.23}$$

$$B_y = (1 - \gamma)\, \alpha \cos\left(x\sqrt{1 + \alpha^2}\right) exp(-z), \tag{6.2.24}$$

$$B_z = -\,(1 + \gamma)\sqrt{1 + \alpha^2} \sin\left(x\sqrt{1 + \alpha^2}\right) exp(-z), \tag{6.2.25}$$

In writing the above form, we have assumed the simplest non force-free state characterized by $\alpha_1 = -\alpha_2 = \alpha$, $k_1 = k_2 = k$. Also, the magnetic field $\mathbf{B}$, the position vector $\mathbf{r}$ and α are re-defined as $\mathbf{B}/k$, $k\mathbf{r}$ and α/k, respectively.

Solving equation (6.2.16) in three dimensions (3D), we consider the same solution procedure as in two dimensional case by assuming absence of y symmetry, and therefore the function ϕ takes the following form

$$\phi_j(x,y,z) = \cos\left(x\sqrt{\frac{k_j^2+\alpha_j^2}{2}}\right)\cos\left(y\sqrt{\frac{k_j^2+\alpha_j^2}{2}}\right) exp(-k_j z). \quad (6.2.26)$$

With the same normalization as in the two dimensional case, the magnetic field components are given by

$$\begin{aligned}
B_x &= \left[(1+\gamma)\cos\left(x\sqrt{\frac{1+\alpha^2}{2}}\right)\cos\left(y\sqrt{\frac{1+\alpha^2}{2}}\right) + \frac{(1-\gamma)(1+\alpha^2)}{2\alpha}\right. \\
&\quad \left.\times \sin\left(x\sqrt{\frac{1+\alpha^2}{2}}\right)\sin\left(y\sqrt{\frac{1+\alpha^2}{2}}\right)\right]\exp(-z), && (6.2.27) \\
B_y &= \left[(1-\gamma)\frac{\alpha^2-1}{2\alpha}\right. \\
&\quad \left.\times \cos\left(x\sqrt{\frac{1+\alpha^2}{2}}\right)\cos\left(y\sqrt{\frac{1+\alpha^2}{2}}\right)\right]\exp(-z), && (6.2.28) \\
B_z &= -\sqrt{\frac{1+\alpha^2}{2}}\left[(1+\gamma)\sin\left(x\sqrt{\frac{1+\alpha^2}{2}}\right)\cos\left(y\sqrt{\frac{1+\alpha^2}{2}}\right)\right. \\
&\quad \left.-\frac{1-\gamma}{\alpha}\cos\left(x\sqrt{\frac{1+\alpha^2}{2}}\right)\sin\left(y\sqrt{\frac{1+\alpha^2}{2}}\right)\right]\exp(-z). && (6.2.29)
\end{aligned}$$

6.2.4 Topological Properties of Equilibrium Solutions

In the following we present the nature of the 2D and 3D equilibrium solutions in terms of magnetic field topology. Two important parameters are α and γ. Magnetic field lines given by equations (6.2.23)-(6.2.25) are contained in a 2D plane and hence such 2D fields are sheared. It can be easily checked the shearing nature of the field lines from equations (6.2.23)-(6.2.25) by calculating the slope of the projected field lines on the xy-plane, which traces a straight line with constant slope. With $\gamma = 0$, equations (6.2.23)-(6.2.25) represents a 2D sheared force-free field, where the amount of shearing is given by the parameter α.

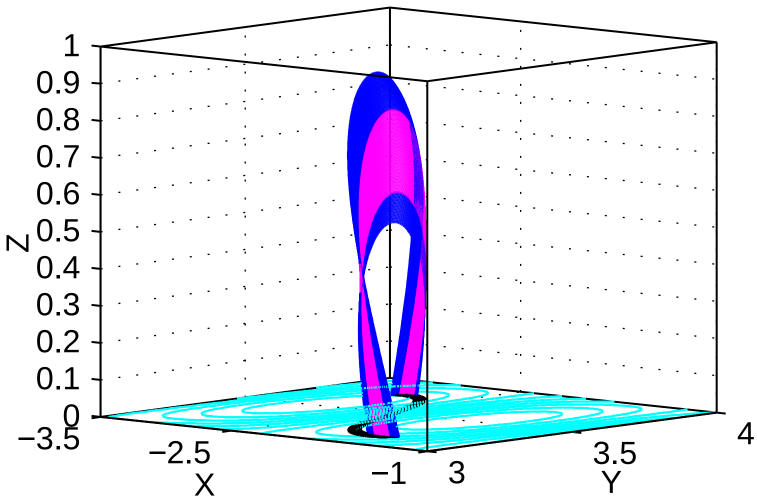

Figure 6.2: Three dimensional magnetic ribbons for a non force-free state with $\gamma = 0.25$ and $\alpha = -3.7$. The projection on the xy-plane represents a backward sigmoidal structure.

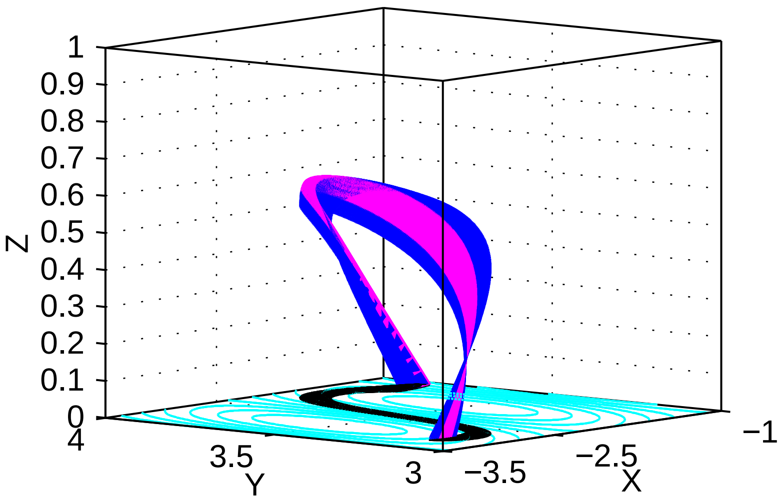

Figure 6.3: Three dimensional magnetic ribbons for a force-free state characterized by $\gamma = 0$ and $\alpha = 3.7$.

3D magnetic fields given by equations (6.2.27)-(7.3.1) are topologically more complex than that of 2D fields. Depending on the value of α and γ, it is possible to explore various topological properties of non force-free, force-free, and potential magnetic fields. Figure 6.1 depicts a set of non force-free magnetic field lines plotted in the form of magnetic ribbons with $\gamma = 0.25$ and $\alpha = 3.7$. The projection of these ribbons on the xy-plane generates a forward sigmoidal structure

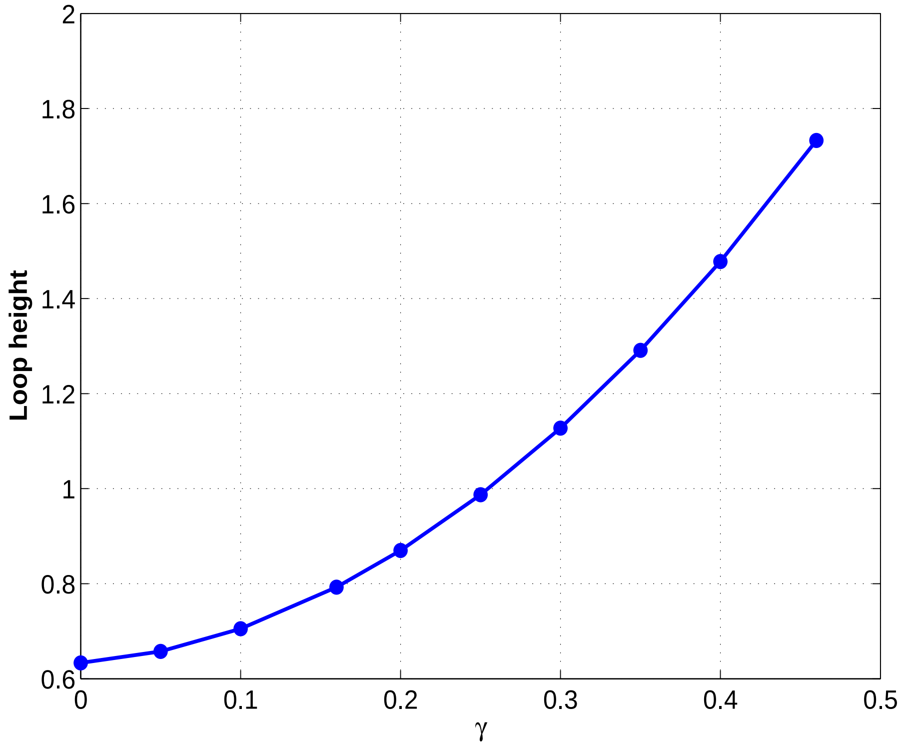

Figure 6.4: Variation of loop height with the non force-free parameter γ for $\alpha = 3.7$.

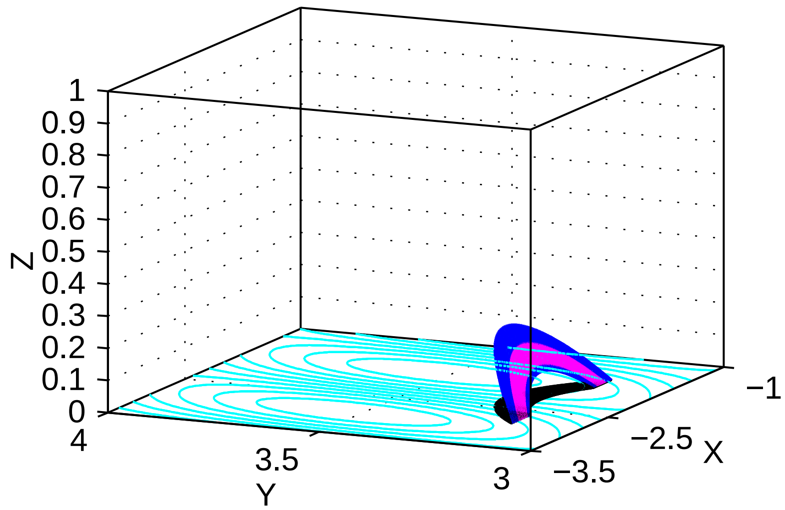

Figure 6.5: Three dimensional magnetic ribbons for the potential state defined by $\alpha = 0$ and $\gamma = 0$.

that confirms the twisted nature of the magnetic field lines. In Figure 6.2 we have plotted the same non force-free state with $\alpha = 3.7$. The backward sigmoidal structure on the xy-plane reveals that the field lines constituting the magnetic ribbons for this case are of opposite twist compared to the field lines belonging to the positive α ribbons. Figure 6.3 represents a set of magnetic ribbons for the force-free state obtained with $\gamma = 0$ and the same α value as in the forward sigmoidal structures shown in Figure 6.1. In comparison to the non force-free ribbons, the force-free ribbons are found to attain lesser height with a more pronounced sigmoidal structures. It is consistently found that by increasing the non force-free parameter γ, the loop height also increases as shown in Figure 6.4. This feature is in qualitative agreement with the general notion that the upper corona is non force-free [95]. A set of magnetic ribbons depicted in Figure 6.5 belongs to the potential magnetic field characterized by $\gamma = \alpha = 0$. As expected, these are of zero twist and least height compared to both the force-free and the non force-free ribbons.

6.3 Summary

Terminal states of equilibrium are accessible as a result of discontinuity formation in magnetic fields. In this chapter we first discussed the general concept of magnetic helicity in the framework of single-fluid MHD. It is shown that the magnetic helicity is a conserved quantity in the ideal MHD limit. However, in a magnetofluid with large electrical conductivity it decays slowly in comparison to its counterpart magnetic energy, and therefore considered to be an invariant of motion. Based on the method of variational calculus the equilibrium state is obtained for single-fluid MHD, which is linear force-free state with zero plasma flow. The observed high β and finite plasma flow in the solar atmosphere motivates to model the flow coupled equilibrium. To achieve this, generalized helicity is obtained using two-fluid plasma model for an isolated system, which couples the flow and the magnetic field. This concept of generalized helicity is extended for an open system like the solar corona to obtain the equilibrium. We presented 2D and 3D solutions of the equilibrium. The various topological properties of the equilibrium magnetic field were discussed. Although the techniques of variational calculus provide a way to obtain the terminal state of equilibrium, it does not provide any information of intermediate dynamics. The next chapter is devoted to study the details of dynamics.

Chapter 7

Initial Value Problems Relevant to Coronal Dynamics

7.1 Introduction

An arbitrarily interlaced continuous magnetic field frozen into a fluid with large electrical conductivity and undergoing evolution, develops magnetic discontinuity in the asymptotic states of equilibrium [3]. Under the large electrical conductivity the magnetic flux remains conserved across the fluid surface [40]. Because of this flux-freezing, a magnetic flux surface everywhere tangential to the magnetic field **B**, once identified with a particular fluid surface will maintain this identity throughout subsequent evolution of the fluid. This equivalence in fluid and flux surfaces enables to partition the magnetofluid into contiguous magnetic subvolumes each entrapping its own magnetic flux system [36, 40]. Consider the case when two such magnetic subvolumes approach each other. They can then come into direct contact by squeezing out the intervening subvolumes. Under favorable conditions the component of magnetic field tangential to the common surface of juxtaposition then becomes discontinuous, thereby developing the magnetic discontinuity (MD) [3]. For such a discontinuous magnetic field the Ampere's law gives electric current density **J**, contained entirely in the plane across which the magnetic field is discontinuous. Thus, a current sheet (CS) is formed. Hereafter we use the two terms MD and CS interchangeably.

However in a real magnetofluid (e.g. the coronal medium) with large but finite electrical conductivity, the diffusivity becomes quite significant at the site of magnetic discontinuity due to the very small spatial scale. The resulting magnetic reconnection (MR) is then localized in space and decays out the MD. Once the MD is decayed, the characteristic scale becomes once again large and the post-reconnection magnetic field lines are frozen to the reconnection outflow [141]. These magnetic field lines with their changed topology are then expected to push further onto field lines located away from the primary reconnection site, eventually leading to secondary reconnections due to local reduction of spatial scale at new sites. Furthermore, the changed topology of magnetic field lines defines new contiguous subvolumes entrapping the magnetic flux, thus enabling new subvolumes coming into contact by ejecting interstitial subvolume. Altogether, this culminates into a series of magnetic reconnection events affecting the dynamics repetitively in time. Presumably, this process continues until the total ordered energy of the magnetofluid achieves an allowable lower limit. Clearly, it is imperative to explore the importance of repeated MRs in shaping up the global dynamics of the magnetofluid.

A successful numerical simulation in this direction primarily requires maintaining the flux-freezing to a high fidelity in between two consecutive MRs [36, 40, 41]. The other requirement is the "switching on" of a magnetic diffusivity, localized and concurrent with the diminishing of the length scale, to onset reconnection [141]. To achieve these requirements, we propose the following hybrid numerical scheme which utilizes a seamless transition from Direct Numerical Simulation (DNS) to Implicit Large Eddy Simulation (ILES) and back [42, 141].

To begin with, let us consider a magnetic field embedded in an incompressible, thermally homogeneous fluid with infinitely large electrical conductivity, relaxing towards the terminal state under the influence of viscosity [36, 40, 141]. The dynamics is then governed by the relevant MHD equations

$$\rho \left[\frac{\partial \mathbf{u}}{\partial t} + (\mathbf{u} \cdot \nabla) \mathbf{u} \right] = -\nabla p + \frac{1}{\mu_0} (\nabla \times \mathbf{B}) \times \mathbf{B} + \mu \nabla^2 \mathbf{u}, \tag{7.1.1}$$

$$\nabla \cdot \mathbf{u} = 0, \tag{7.1.2}$$

$$\frac{\partial \mathbf{B}}{\partial t} = \nabla \times (\mathbf{u} \times \mathbf{B}), \tag{7.1.3}$$

$$\nabla \cdot \mathbf{B} = 0, \tag{7.1.4}$$

in standard notations, where ρ and μ are uniform density and coefficient of viscosity respectively. The assumption of incompressible flow is justified a posteriori by the simulations which result in small fluid velocity compared to the Alfven velocity. In its analytical form, equation (7.1.4) is redundant in the sense that it is implied for all time by the induction equation (7.1.3) when the initial field is solenoidal, but it is certainly useful to check the accuracy of the computations. The magnetic and velocity fields are bounded in the computational domain, satisfying conditions that the net magnetic and velocity fluxes through the boundaries of the computational domain are individually zero. The evolution starts from an arbitrary topology of magnetic field $\mathbf{B}(\mathbf{x}, t = 0) = \mathbf{B}_0(\mathbf{x})$ with the fluid at rest, $\mathbf{u}(\mathbf{x}, t = 0) = 0$. As the evolution progresses, the change in total magnetic energy W_M is given by

$$\frac{dW_M}{dt} = -\int \frac{1}{\mu_0} [(\nabla \times \mathbf{B}) \times \mathbf{B}] \cdot \mathbf{u} \, d\tau, \tag{7.1.5}$$

accounting for the work done on the fluid by the Lorentz force. This work done by the Lorentz force is then converted to the kinetic energy W_K which is further dissipated by viscosity, as follows

$$\frac{dW_K}{dt} = \int \frac{1}{\mu_0} [(\nabla \times \mathbf{B}) \times \mathbf{B}] \cdot \mathbf{u} \, d\tau - \int \mu \left| \nabla \times \mathbf{u} \right|^2 \, d\tau. \tag{7.1.6}$$

Therefore the change in total energy, $W_T = W_M + W_K$, of the magnetofluid can be written as

$$\frac{dW_T}{dt} = -\int \mu \left|\nabla \times \mathbf{u}\right|^2 \; d\tau. \tag{7.1.7}$$

It is immediately seen from this expression that the total energy of the magnetofluid decreases monotonically due to the viscous drag till the magnetofluid achieves the terminal state with zero fluid velocity. This terminal state corresponds to the magnetostatic equilibrium since the magnetic field cannot decay to zero because of flux freezing [36]. In this relaxation process, the topology of field lines is preserved throughout the relaxation and therefore, the field topology in the magnetostatic equilibrium is same as that of the initial field $\mathbf{B}_0$. However, magnetostatic equilibrium can be realized only in the asymptotic terminal state. In practice, an approximate balance between the Lorentz force, pressure gradient and the viscous drag determines the quasi-steady terminal state characterized by a small kinetic energy. For an initially complex magnetic topology, formation of CSs are then expected as the magnetofluid relaxes to the terminal quasi-steady state. Consequently the magnetic field gradient sharpens locally up to a threshold determined by the grid resolution and numerical techniques employed. This process generates under-resolved scales, with associated numerical artifacts such as spurious oscillations. In standard large eddy simulation, the under-resolved scales are filtered out with the aid of explicit subgrid-scale models [47]. An alternative and effective way of filtering out the under-resolved scales is to utilize the apt numerical diffusivity of nonoscillatory finite-volume differencing, mimicking the action of explicit subgrid scale turbulence models [142]. The dissipation of under-resolved scales through this diffusivity then results in MRs that are colocated and concurrent with the CSs. Post reconnection, the field is well resolved so the computation is back again in its DNS (direct numerical simulation) mode, and allows for further development of CSs as the field lines frozen in the reconnection outflow push onto another set of magnetic field lines. Such seamless transitions from a DNS to an ILES (implicit large eddy simulation) and back, then imitates physical MRs in a high Lundquist number magnetofluid in terms of being colocated and concurrent to the development of CSs— opening up a way to explore formation of CSs and their influence on magnetofluid evolution through repetitive MR events [141].

In this chapter our goal is to numerically investigate the formation of magnetic discontinuities and the role of subsequent magnetic reconnections in generating various magnetic structures as the magnetofluid relaxes towards the quasi-equilibrium. For the purpose, we consider two sets of numerical experiments based on suitable initial value problems (IVPs) with complex magnetic topology for an isolated and an open system, respectively. The initial magnetic fields are topologically equivalent to the coronal magnetic fields. In the first set of numerical experiments for an isolated system, our aim is to only demonstrate the formation of magnetic discontinuities and the possible natural sites where discontinuities are expected to appear. In the second set of numerical experiments for an open system, we study the role of repeated MRs in generating various complex magnetic structures, topologically similar to the magnetic structures in the solar corona.

The above objectives are accomplished by solving the MHD equations in standard MKS units. Such calculations are reliable within the scope of our study, i.e., to understand the basic topological effects of the relaxation process in a qualitative manner. It is to be noted that, in general, the MHD equations are usually solved in its dimensionless form, but the usefulness of such calculation is important only when one tries to make a quantitative comparison with some actual observations. Irrespective of solving the MHD equations in its dimensionless or dimensional form, the general behavior of the simulated MHD flows depends on the associated value of the Lundquist number S of the magnetofluid under consideration. That is to say, if the S value is the same for both dimensionless and the dimensional systems, then the corresponding MHD flows will be dynamically similar. The only advantage of using the dimensionless form of MHD equations is that it is easier to make a quantitative comparison with the realistic situation utilizing the appropriate scaled parameters. However, such a quantitative comparison with a real physical scenario by solving the MHD equations in its dimensional form is cumbersome, and only a qualitative comparison would be possible. With these general ideas, we now emphasize the relevance of our numerical experiments to the solar corona. In presence of viscosity and resistivity, the dimensionless form of MHD equations read as

$$\rho' \left[\frac{\partial \mathbf{u}'}{\partial t'} + (\mathbf{u}' \cdot \nabla')\,\mathbf{u}'\right] = -\nabla' p' + (\nabla' \times \mathbf{B}') \times \mathbf{B}' + \frac{1}{S_v}\nabla'^2 \mathbf{u}', \quad (7.1.8)$$

$$\nabla' \cdot \mathbf{u}' = 0, \quad (7.1.9)$$

$$\frac{\partial \mathbf{B}'}{\partial t'} = \nabla' \times (\mathbf{u}' \times \mathbf{B}') + \frac{1}{S}\nabla'^2 \mathbf{B}', \quad (7.1.10)$$

$$\nabla' \cdot \mathbf{B}' = 0, \quad (7.1.11)$$

where the transformation to dimensionless form is carried out by the appropriate choice of reference parameters $(L_0, B_0, \rho_0, v_A, \tau_A, p_0)$ as follows

$$\mathbf{x}' \equiv \mathbf{x}/L_0, \mathbf{B}' \equiv \mathbf{B}/B_0, \rho' \equiv \rho/\rho_0, \mathbf{u}' \equiv \mathbf{u}/v_A, t' \equiv t/\tau_A,$$
$$p' \equiv p/p_0 \equiv p\mu_0/B_0^2, \nabla' \equiv L_0\nabla, \frac{\partial}{\partial t'} \equiv \tau_A \frac{\partial}{\partial t}. \quad (7.1.12)$$

Here v_A and τ_A are the Alfven velocity and the Alfven time, respectively, and primed variables are dimensionless. On the right hand sides of equations (7.1.8) and (7.1.10) appear two dimensionless parameters, the viscous Lundquist number $S_v \equiv \frac{\rho_0 L_0 v_A}{\mu}$ and the Lundquist number $S \equiv \frac{L_0 v_A}{\eta}$, respectively, where μ is the viscosity and η is the magnetic diffusivity. With the chosen reference parameters to coronal values, it is immediately seen that the solution of equations (7.1.8)-(7.1.11) will yield the similar kind of MHD flows to that in the solar corona only when the computational model employs the values of both S_v and S to be the same as in the corona. Thus only those simulations which are performed with the actual values of both S_v and S essentially provide a realistic comparison with the solar corona in a quantitative manner. If however either of S_v or S do not match with the actual coronal values then, obviously, the simulated flows may not be quantitatively realistic. An important point to be noted that the computational requirements put constraint over the choice of the parameters $(\mu', \eta', \rho', L', t')$— related by the relations $\frac{\mu' \Delta t'}{\rho' \Delta L'^2} \leq 1$ and $\frac{\eta' \Delta t'}{\Delta L'^2} \leq 1$, where $\Delta L' = L'/N$ with N as the grid resolution— for the numerical solution to be stable. Clearly, for a given grid resolution we need to adjust the other parameters to satisfy the above stability conditions. Under these adjustments of computational parameters, it is then impossible to match the values of all the physical variables to the actual coronal values. As a result of this, computational model does not have the same values of S_v and S to that in the solar corona. The desired values of S_v and S, as in the corona, can only be achieved by increasing the grid resolution, which is practically unattainable with the available computational resources. Till date, we hardly obtain the Lundquist number of the order of $\approx 10^{3-4}$ for a given computational model. However, in the actual corona the Lundquist number is of the order of $\approx 10^{13}$. Evidently, we cannot make a realistic quantitative comparison between the computational model and the solar corona as their values differ by many orders of magnitude. In other words, although the dimensionless treatment of MHD allows one to make a quantitative comparison but, in principle, the lack of the desired values of S_v and S moots the question of a realistic comparison.

In the light of above discussions we note that the deviations of our numerical experiments from the corona then would only be reflected in the numerical values of two dimensionless numbers S and S_v. We further note that in our computations, S is effectively infinite except for the locations of MRs. The residual dissipation responsible for these MRs being intermittent in time and space, a quantification of it is only meaningful in the spectral space, where — in analogy to the eddy-viscosity of explicit subgrid-scale models for turbulent flows — it only acts on the shortest modes admissible on the grid [143]; in particular, in the vicinity of steep gradients in simulated fields. Also, in our computations $S_v \approx 10$, whereas an approximate value of the same parameter in the corona is 10^{11}. This deviation in S_v only affects the time scale over which the magnetofluid evolves and has no direct consequence on the change in magnetic topology. The assumptions of constant fluid density and thermal homogeneity are also not compatible with the actual corona. However, in our simulations the uniform density being valid within one scale height which is quite large in the corona on account of large coronal temperature. Altogether then, the relevance of our computations to different coronal structures are only in terms of their similarities in magnetic topology. Also, our results can only be interpreted in a qualitative manner and not suitable for a quantitative comparison with the actual corona.

7.2 Numerical Experiments- I: Isolated System

7.2.1 Initial Value Problem

The initial magnetic field is assumed to be a superposition of two linear force-free fields which are relevant to general magnetic morphology of the solar corona, and also mimics a possible scenario of flux emergence as envisioned in reference [144]. To construct the initial value problem (IVP), let $\mathbf{B}_1$ and $\mathbf{B}_2$ be two linear force free fields satisfying

$$\begin{aligned} \nabla \times \mathbf{B}_1 &= \alpha_1 \mathbf{B}_1, \\ \nabla \times \mathbf{B}_2 &= \alpha_2 \mathbf{B}_2, \end{aligned} \tag{7.2.1}$$

with torsion coefficients α_1 and α_2 representing the magnetic circulations per unit flux for $\mathbf{B}_1$ and $\mathbf{B}_2$ [31] respectively. A overlapped magnetic field is then created by a linear superposition of $\mathbf{B}_1$ and $\mathbf{B}_2$, written as

$$\mathbf{B}' = \mathbf{B}_1 + \gamma \mathbf{B}_2, \tag{7.2.2}$$

where γ is a constant weighting factor related to the relative amplitudes of the two superposed fields and represents the deviation of $\mathbf{B}'$ from its force-free configuration. The field lines for $\mathbf{B}'$ are also twisted, as can easily be verified by noting $\mathbf{J}' \cdot \mathbf{B}' \neq 0$ except for the trivial case of $\mid \mathbf{B}_1 \mid = \mid \mathbf{B}_2 \mid = 0$.

The Lorentz force exerted by $\mathbf{B}'$ is then given by

$$\mathbf{J}' \times \mathbf{B}' = \frac{1}{\mu}\gamma(\alpha_1 - \alpha_2)\mathbf{B}_1 \times \mathbf{B}_2. \tag{7.2.3}$$

For an isolated system (or a triply periodic domain) in Cartesian geometry, the components of $\mathbf{B}'$ are

$$\begin{aligned}
&B'_x = k_1k_2\cos(k_1x)\cos(k_2y)\sin(k_3z) - \alpha_1k_3\sin(k_1x)\\
&sin(k_2y)cos(k_3z) + \gamma[l_1l_2\cos(l_1x)\cos(l_2y)\sin(l_3z)\\
&-\alpha_2l_3\sin(l_1x)sin(l_2y)cos(l_3z)],\\
&B'_y = (k_1^2 + k_3^2)\sin(k_1x)\sin(k_2y)\sin(k_3z) + \gamma[(l_1^2 + l_3^2)\\
&\sin(l_1x)\sin(l_2y)\sin(l_3z)],\\
&B'_z = k_2k_3\sin(k_1x)\cos(k_2y)\cos(k_3z) + \alpha_1k_1\cos(k_1x)\\
&\sin(k_2y)\sin(k_3z) + \gamma[l_2l_3\sin(l_1x)\cos(l_2y)\cos(l_3z)\\
&+\alpha_2l_1\cos(l_1x)\sin(l_2y)\sin(l_3z)],
\end{aligned} \tag{7.2.4}$$

with $\alpha_1 = \sqrt{k_1^2 + k_2^2 + k_3^2}$ and $\alpha_2 = \sqrt{l_1^2 + l_2^2 + l_3^2}$; the triplets $k = \{k_1, k_2, k_3\}$ and $l = \{l_1, l_2, l_3\}$ representing different modes. From equation (7.2.3) then for conditions $k = l$ or $\gamma = 0$, $\mathbf{B}'$ is force-free. We consider $\mathbf{B}'(x, y, z) = \mathbf{H}(x, y, z)$, characterized by $k = \{1, 1, 1\}\ m^{-1}$, $l = \{2, 2, 2\}\ m^{-1}$ and $\gamma = 0.5$, as the initial magnetic field in our simulations.

In the following we describe the magnetic topology of $\mathbf{H}$ in terms of magnetic nulls and separators [145], since CSs are expected to form at the neighborhood of these structures [146]. Also it is to be noted that CS formation in three dimensions can also occur in absence of nulls [147]. Panel a of Figure 7.1 illustrates all possible nulls of $\mathbf{H}$ in the computational domain of volume $(2\pi)^3\ m^3$. In this and subsequent figures, the arrows in colors red, green and blue represent the directions x, y, and z respectively. The illustrations of magnetic nulls use the condition $\mathbf{B} = 0$ at the null points. For the purpose, we define a Gaussian function

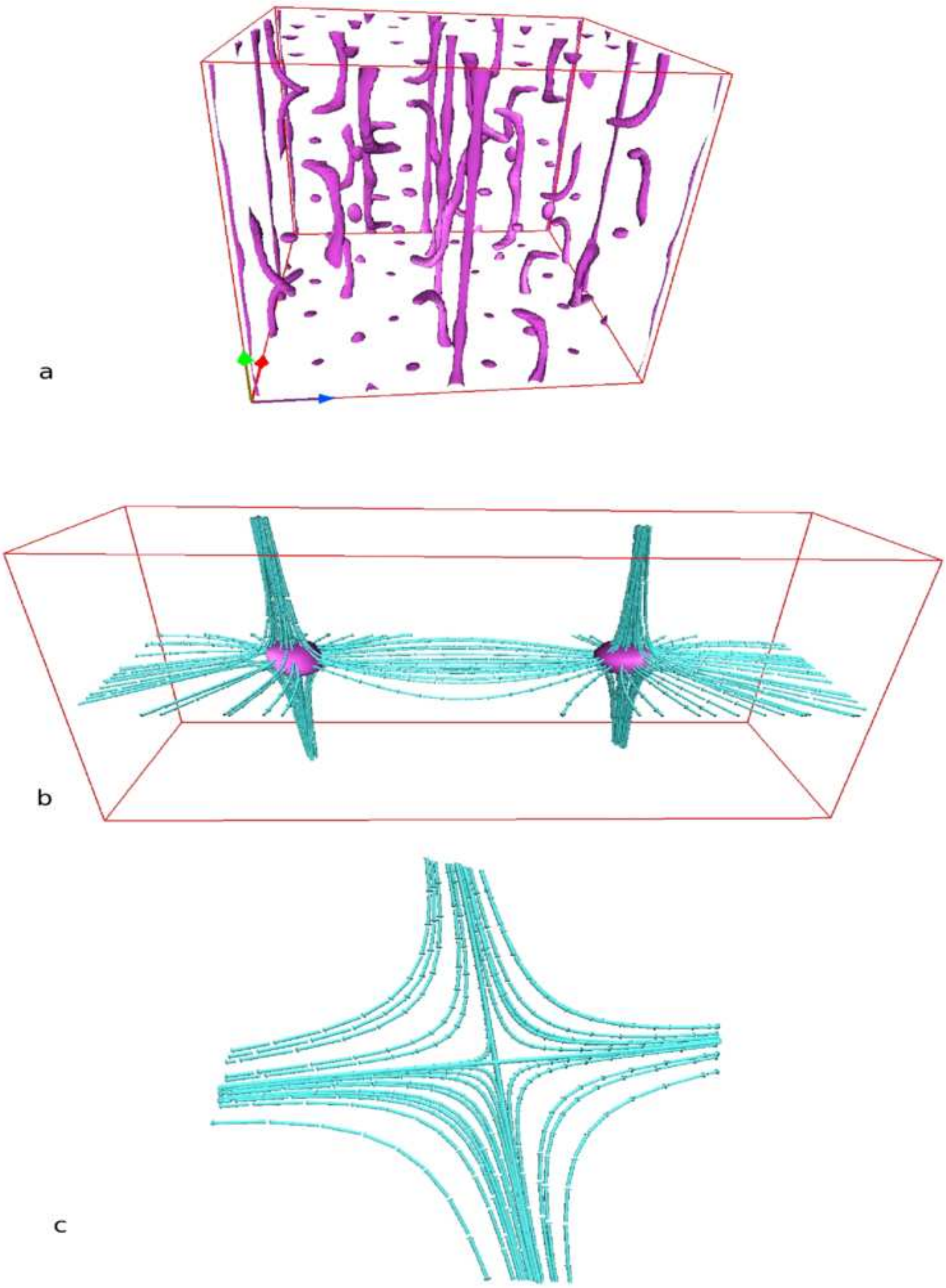

Figure 7.1: Panel a shows magnetic nulls represented by isosurfaces of $\mathbf{H}$ with parameters $H_0 = 0.01\ T$ and $\Delta H_0 = 0.05\ T$ for $k = \{1, 1, 1\}\ m^{-1}, l = \{2, 2, 2\}\ m^{-1}$ and $\gamma = 0.5$. A pair of 3D nulls with corresponding spine axes and fan planes are shown in panel b. The field topology along with separatices near the 2D null located at $x = \pi\ m, y = 3\pi/2\ m, z = \pi\ m$ is depicted in panel c which is of X-ype geometry.

$$\psi(x,y,z) = exp\left[-\sum_{i=x,y,z}\frac{(H_i(x,y,z)-H_0)^2}{\Delta H_0}\right]. \tag{7.2.5}$$

where $\sqrt{\Delta H_0}$ determines width of the Gaussian and H_0 represents a particular isovalue of $H_x, H_y,$ and $\mathrm{H_z}$. By choosing $H_0 \approx 0$ and a small ΔH_0, the function $\psi(x,y,z) \neq 0$ only if $H_i \approx H_0$ for each i. The three dimensional (3D) nulls are then the points where the three isosurfaces $H_x = H_0, H_y = H_0, H_z = H_0$ intersect. It should be noted that at the immediate vicinity of a 3D null all the three components of magnetic field are nonzero. Similarly, a two dimensional (2D) null in a 3D coordinate space can be described as a line of intersection between H_x and H_y isosurfaces with isovalue H_0 where $H_0 \approx 0\ T$. Using the above technique, in panel a of Figure 7.1 we have depicted both 3D and 2D nulls of $\mathbf{H}$ for parameters $H_0 = 0.01\ T$ and $\Delta H_0 = 0.05\ T$.

In panel b of Figure 7.1, we have plotted magnetic field lines about a pair of 3D nulls along with their spine axes and overlapping fan structures. From equations (7.2.4), it can easily be seen that $H_x = H_y = H_z = 0\ T$ at $x = z = \pi\ m$ rendering the corresponding $y = 0\ m$ to $y = 2\pi\ m$ line, hereafter referred as y-line, to be a neutral line. Further insight can be gained by expanding the field components in a Taylor series in the immediate neighborhood of $x = \pi\ m,\ z = \pi\ m$ for a constant y. Retaining only the first order terms, equations (7.2.4) reduce to

$$\begin{aligned}
H_x &= -(x-\pi)[\alpha_1 k^2 \sin(ky_0) + \gamma\alpha_2 l^2 \sin(ly_0)] \\
&\quad + (z-\pi)[k^3 \cos(ky_0) + \gamma l^3 \cos(ly_0)], \\
H_y &= 0, \\
H_z &= (x-\pi)[k^3 \cos(ky_0) + \gamma l^3 \cos(ly_0)] \\
&\quad + (z-\pi)[\alpha_1 k^2 \sin(ky_0) + \gamma\alpha_2 l^2 \sin(ly_0)].
\end{aligned} \tag{7.2.6}$$

The components H_x and H_z given by equations (7.2.6) have point antisymmetry about coordinates $x = z = \pi\ m$ along the y-line, rendering every point on it to be a X-type neutral point. It is also to be noted that only points $y =$

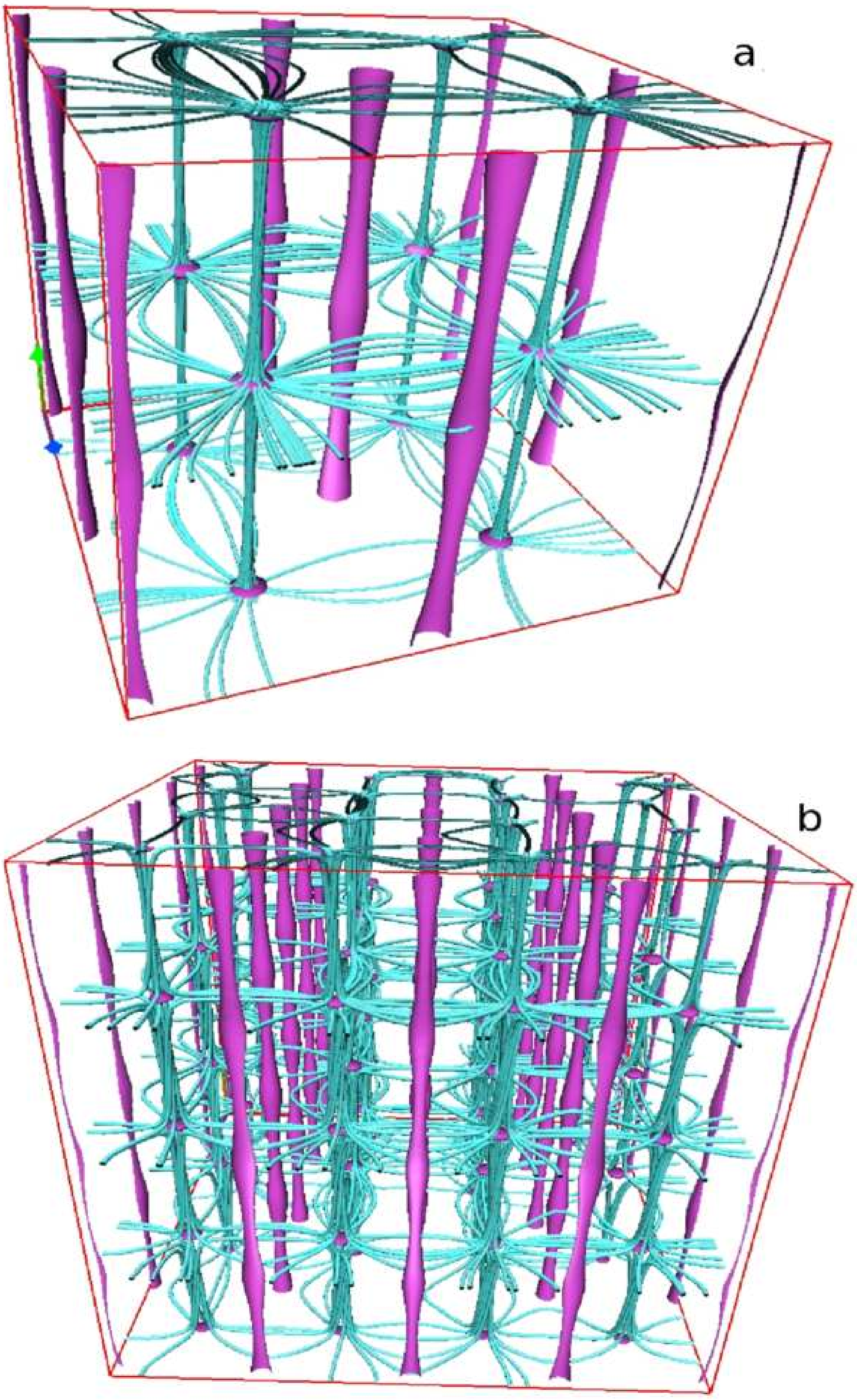

Figure 7.2: Panels a and b depict the magnetic nulls represented by isosurfaces with parameters $H_0 = 0.01\ T$ and $\Delta H_0 = 0.05\ T$ of force-free magnetic fields $\mathbf{B}_1$ and $\mathbf{B}_2$ separately. The connectivity of field lines in the neighborhood of these nulls are shown by solid lines.

$0, \pi, 2\pi$ m are rotationally symmetric about the y line which can easily be verified by interchanging x and z. Figure 7.1, panel c shows the magnetic configuration of one such X-type neutral point located at $y = \pi$ m. In addition to these 3D and 2D nulls, a set of 2D X-type neutral points in the form of shoe-shaped structures are present in $\mathbf{H}$ as shown in panel a, Figure 7.1. These shoe-shaped nulls originate because of the superposition as can be verified by comparing panel a of Figure 7.1 with panels a and b of Figure 7.2 showing complete absence of such nulls in $\mathbf{B}_1$ and $\mathbf{B}_2$ drawn separately for $k = \{1, 1, 1\}$ m^{-1} and $l = \{2, 2, 2\}$ m^{-1}. It is to be noted that the individual torsion coefficients defined by mode numbers k and l fixes the angle between the two superposing fields and also play a possible role in determining the complexity of $\mathbf{H}$ by increasing the number of magnetic nulls.

7.2.2 Simulation Results and Discussions

Direct numerical simulations are carried out with $\mathbf{H}$ as the initial condition. The domain size is $(2\pi)^3$ m^3, resolved with 128^3 uniform grid resolution. The temporal increment $\Delta t = 0.004$ s. The density is set to $\rho = 1$ kg m^{-3}. The magnetofluid is evolved from rest (with zero fluid velocity). The boundary conditions are employed to be periodic in all three directions of Cartesian domain. To highlight the role of unbalanced force in formation of CSs, the results are presented for two different viscosities $\mu_1 = 0.004$ m^2 s^{-1} and $\mu_2 = 0.0035$ m^2 s^{-1}, with same initial magnetic field and hence Lorentz force.

To understand the overall dynamics of the magnetofluid, in panels a and b of Figure 7.3 we have plotted time evolution of the normalized average magnetic and kinetic energies for 128^3 uniform grid resolution. The solid and dashed lines correspond to viscosities $\mu_2 = 0.0035$ m^2 s^{-1} and $\mu_1 = 0.004$ m^2 s^{-1}, respectively. The panels show a rise in kinetic energy at the expense of magnetic energy along with two distinct peaks in kinetic energy at $t = 6$ s and $t = 160$ s respectively while the system relaxes from the initial static state. Panels c and d of Figure 7.3 illustrate the corresponding evolution of spatially averaged current density $<\mid \mathbf{J} \mid>$ and maximum current density $\mid \mathbf{J}_{max} \mid$. Both plots show an almost symmetric sharp rise and decay about $t = 6$ s followed by an intermediate phase

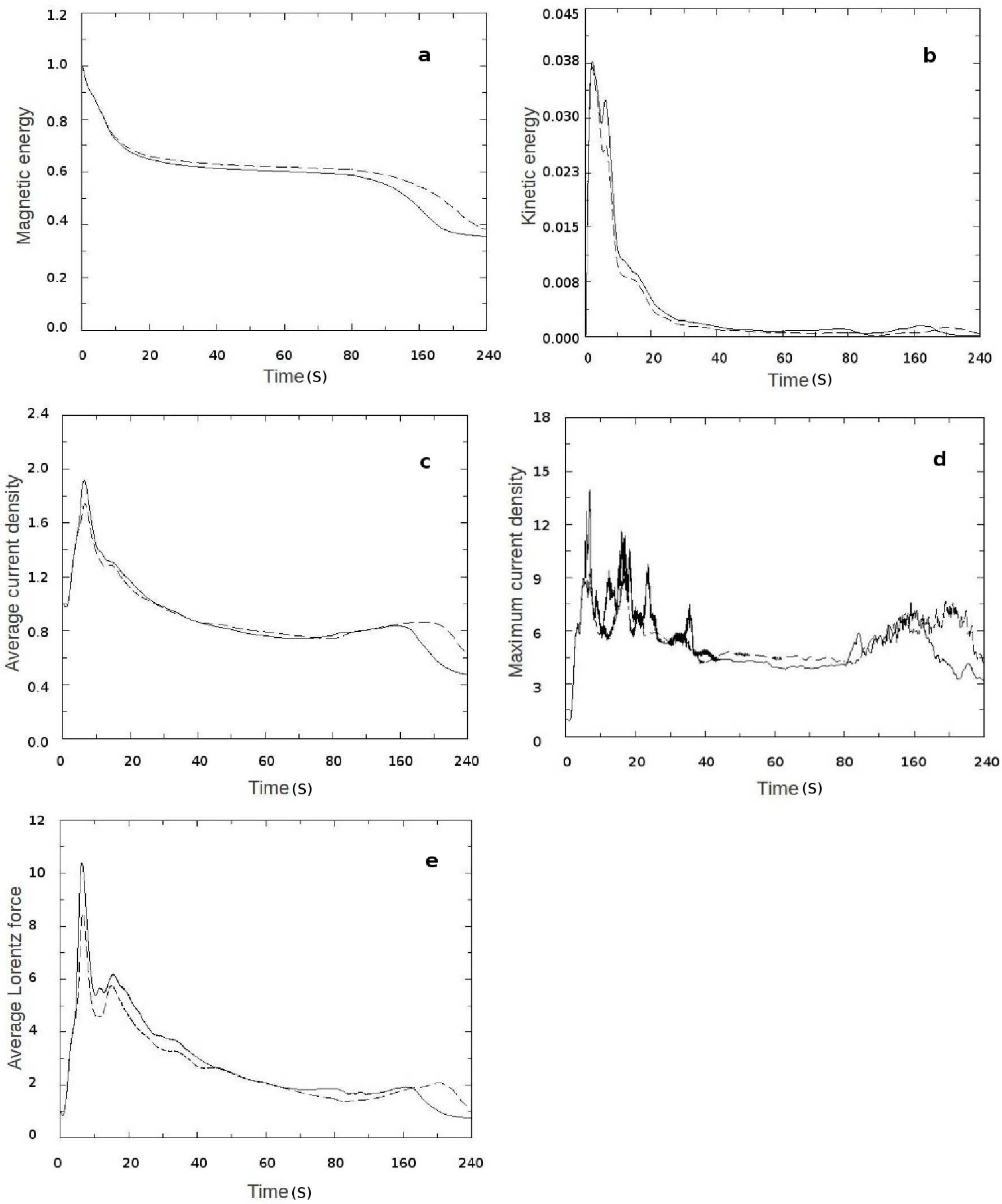

Figure 7.3: History of magnetic energy (panel a), kinetic energy (panel b), $<\mid \mathbf{J} \mid>$ (panel c), $\mid \mathbf{J}_{max} \mid$ (panel d), grid averaged Lorentz force (panel e), for viscosities $\mu_2 = 0.0035\ m^2\ s^{-1}$ (solid lines) and $\mu_1 = 0.004\ m^2\ s^{-1}$ (dashed lines). The magnetic and kinetic energies are normalized with the initial total energy whereas $<\mid \mathbf{J} \mid>$, $\mid \mathbf{J}_{max} \mid$ and grid averaged Lorentz force are normalized with their respective initial values. For better clarity in representing the peaks, the time axis is morphed to $t' = s_0 t$ with $s_0 = 4$ from $t = 0\ s$ to $t = 80\ s$ and $s_0 = 1$ for $t > 80\ s$ to $t = 240\ s$.

of quasi-steady state. A feeble second peak is formed at $t = 160$ s which is once again nearly symmetric. The formation of such peaks in current density can generally be attributed to formation of CSs and their subsequent decay by magnetic reconnection [148]. Since in our simulations the decay of CSs is entirely due to numerically assisted reconnection, the two peaks in current density require further clarifications.

To verify numerical accuracy of the computational model, before, during and after the formation of peaks in current density, in panels $a-c$ of Figure 7.4 we have plotted the energy budget for magnetic (solid line), kinetic (dashed line), and total (dotted line) energies (normalized to initial total energy) by calculating the numerical deviations in computed energy balance equations from their analytically correct expressions given by equations (7.1.5)-(7.1.7) for $\mu = \mu_2$. In Figure 7.4, panel a plots the numerical deviations over the whole computational time whereas panels b and c highlight their peak values for better clarity. The plots show a maximal numerical deviation of magnitude 0.1 in magnetic energy balance from its analytically correct value of zero during formation of the first peak in current density confirming the possibility of the magnetic reconnection at $t = 6$ s. After the first peak, the model regains its desired numerical accuracy, loosing it again by a marginal amount during formation of the second peak in current density (panel c, Fig. 7.4). This almost accurate maintenance of energy balance in the intermediate phase along with numerically acceptable small deviations at the peaks then provides the necessary basis to assume the MPDATA generated residual magnetic diffusivity in response to under-resolved magnetic field, to be intermittent and adaptive. A seamless transition from DNS to ILES is then a possibility where the under-resolved scales are removed by this residual diffusivity and the evolution is well resolved over the whole computational time; a property of MPDATA which has already been well studied for Navier-Stokes flow of a neutral fluid [149]. The reconnection in the computational model then reasonably mimics a physical reconnection in presence of a real diffusivity.

To further understand the global dynamics, in panel e of Figure 7.3 we have plotted the magnitude of Lorentz force averaged over the computational domain.

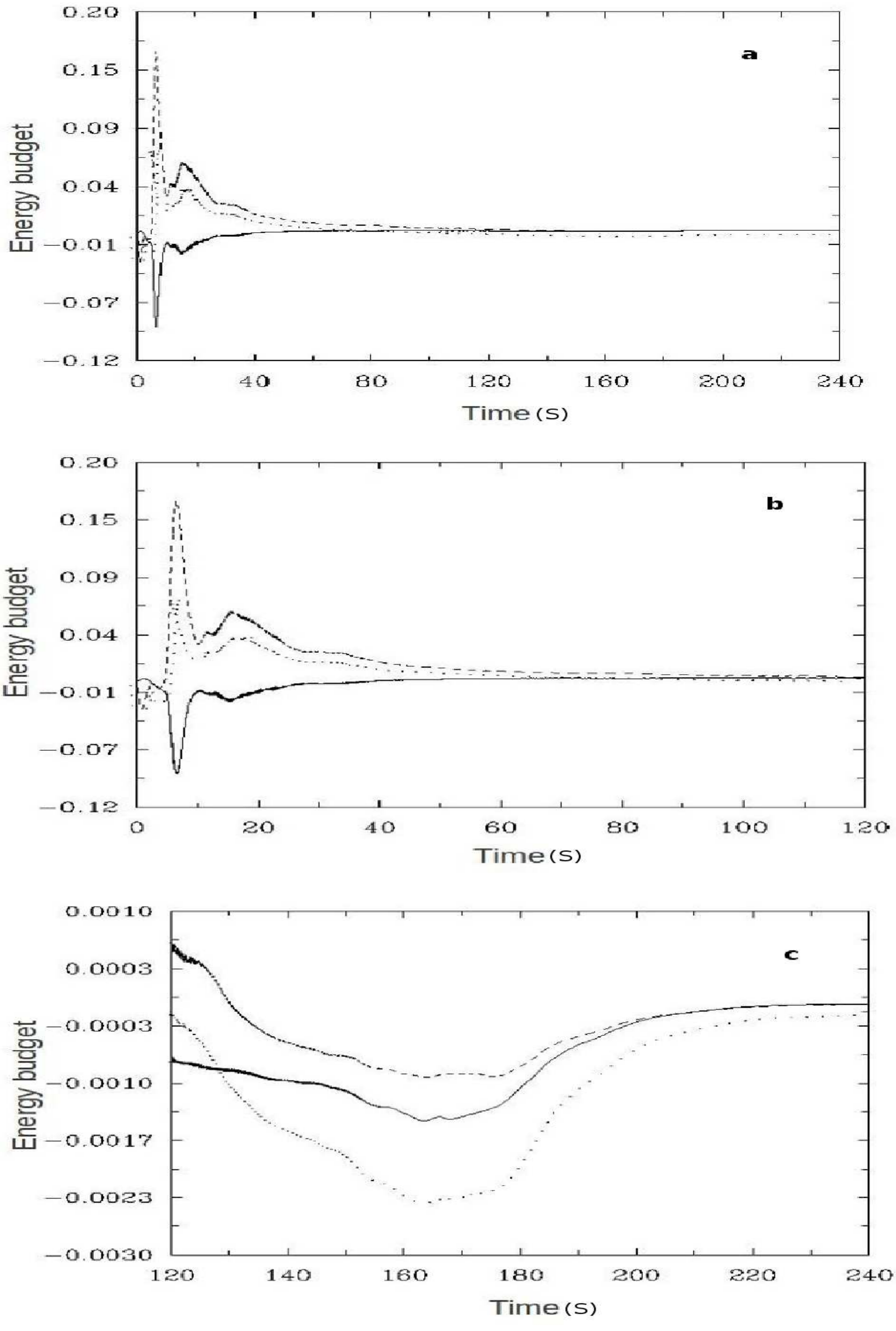

Figure 7.4: History of energy budget for total (dotted line), kinetic (dashed), and magnetic (solid) energies (each normalized with the initial total energy) for viscosity $\mu = 0.0035\ m^2\ s^{-1}$, drawn for full computational domain (panel a) and localized at the two peaks of current density (panel b and panel c).

The plot shows an initial sharp rise just before the first peak in current density after which it decreases substantially. At the end of the quasi-steady state, the Lorentz force once again rises marginally before the second peak in **J** followed by a decay.

From the above discussions and noting that a zero Lorentz force describes a force-free field while the simulated reconnection mimics the physical reconnection, the following picture evolves. The initial nonzero Lorentz force pushes the magnetofluid resulting in an increase in kinetic energy at the expense of magnetic energy. As the magnetofluid is pushed by the initial Lorentz force the magnetic field gradients sharpen forming CSs, till the characteristic length scale over which the magnetic field varies goes below the model resolution. The consequent reconnection then lowers the magnetic energy and hence magnitude of **B**, while dissipation of smaller scales reduce the gradient of **B** and hence magnitude of current density **J**. The combined effect is that of lowering the volume averaged Lorentz force, vide panel *e* of Figure 7.3, which may describe an incomplete Taylor relaxation [124]. In the intermediate phase the magnetofluid evolves quasisteadily in response to this small Lorentz force. At $t = 160\ s$ the second peak is formed, once again through CS formations and their eventual decay as is evident from the corresponding loss of numerical accuracy in the energy balance equations (vide Fig. 7.4, panel *c*). An important observation in this regard is the large difference in amplitude between the two peaks in spite of their common origin, i.e., the loss in model resolution. A more overt evidence of CS formation is obtained by direct volume rendering (DVR) of $\mid \mathbf{J} \mid$ (Fig. 7.5) which depicts the initial three dimensional structure of current density to become almost two dimensional as the current density peaks and generates small scales. The formation of CSs depends significantly on viscosity as can be inferred from panel *c* of Figure 7.3 where the peaks in current density appear at two different times for viscosities $\mu = 0.0035\ m^2\ s^{-1}$ and $\mu = 0.004\ m^2\ s^{-1}$. This is in accordance with our physical expectation that with the same Lorentz force, a highly viscous plasma will take longer time than an otherwise less viscous plasma to be pushed till the smallest model resolution is achieved.

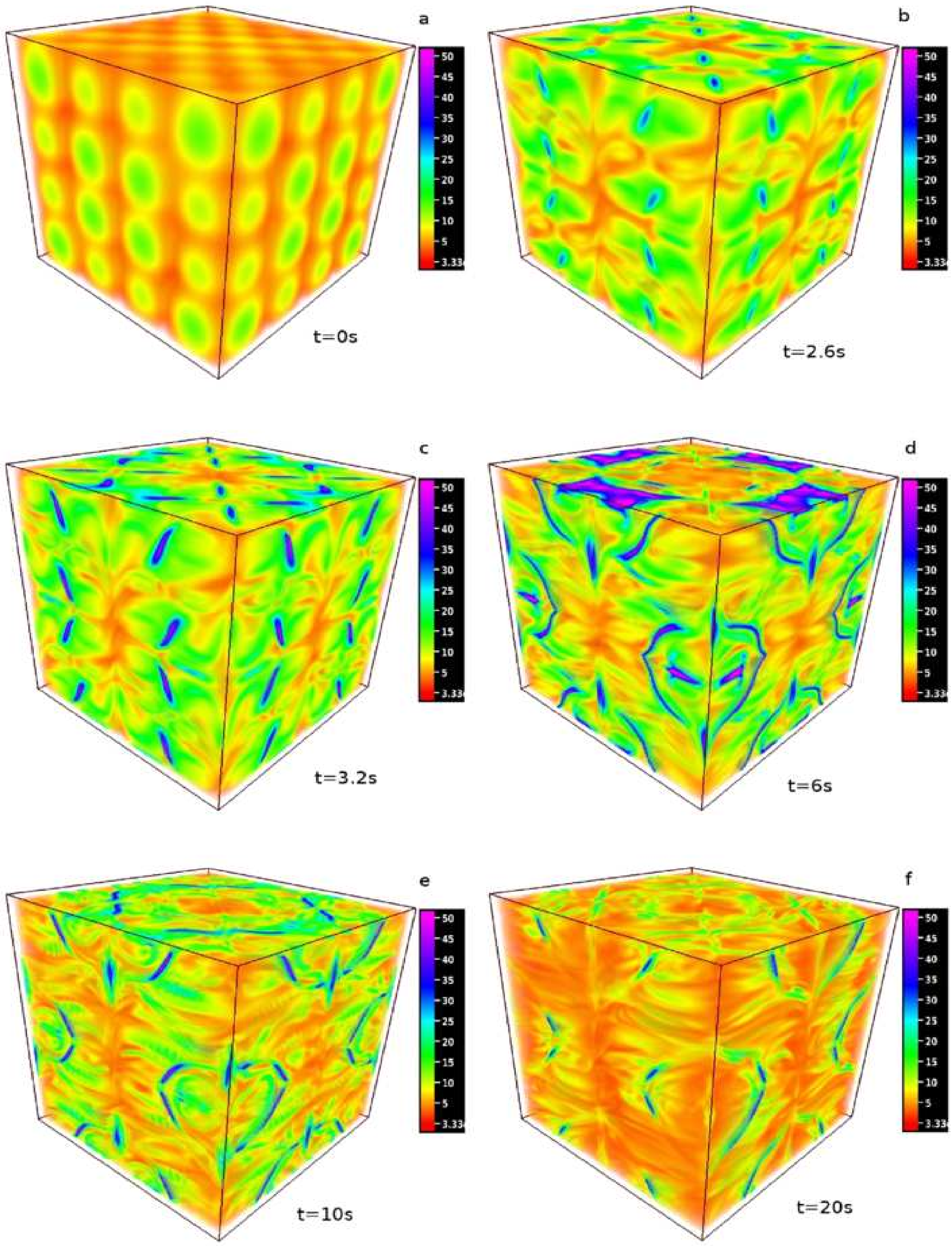

Figure 7.5: Time sequence of direct volume rendering of $<|\ \mathbf{J}\ |>$ for 128^3 uniform grid and viscosity $\mu = 0.0035\ m^2\ s^{-1}$. The color code represents the magnitude of $<|\ \mathbf{J}\ |>$ (in $A\ m^{-2}$). Figures depict growth and decay of the current density.

Further insight into the dynamics of these CSs are obtained by understanding evolution of magnetic fields and current densities near the two and three dimensional nulls depicted in Figure 7.1, panel a. The following analyses correspond to simulations with viscosity $\mu = \mu_2$ and uniform grid resolution of 128^3. Figure 7.6 plots the time sequence of magnetic field lines at the neighborhood of a pair of 3D nulls. Each time frame is overplotted with a selected isosurface of $\mathbf{J}$ having a value which is 40% of $\mid \mathbf{J} \mid_{max}$ (J40) at the first peak in current density. The initial unbalanced Lorentz force pushes the magnetofluid and hence the spine axes and fan surfaces toward each other, thereby developing gradient in magnetic field at the separator. This increased gradient in magnetic field results in a growth of current density as observed at $t = 6\ s$ which is cotemporal with the first current density peaks in Figure 7.3, panel c. The appearance of the J40 isosurface near $t = 6\ s$ at the separator is a direct evidence of CS formation. The decay of CSs after $t = 6\ s$ is due to the reconnection as pushing of the magnetofluid is continued below the model resolution.

The collapse of shoe-shaped nulls also have significant contribution to the first peak in current density. Each point on a shoe-shaped null is an X-type neutral point while the loci of such points trace a curved line in 3D space. Figure 7.7 shows the evolution of a pair of shoe-shaped nulls. This pair spans along the y-axis near $x = \pi/2\ m, z = \pi\ m$. During evolution, CSs are developed first at the maximum curvature region of the shoe-shaped pair followed by CS formations at other regions. Most of the current density is observed to grow near the maximum curvature region, cotemporally with first peaks in current densities at $t = 6\ s$. Formation and decay of CSs away from the maximum curvature region of a shoe-shaped null is observed to be near $t = 16\ s$ and is approximately cotemporal with the second spike in numerical deviation of magnetic energy balance plotted in Figure 7.4, panel b.

In Figure 7.8 we have illustrated the evolution of 2D nulls overplotted with the isosurface of 40% of $\mid \mathbf{J} \mid_{max}$ at the second peak in current density. The CSs for these 2D nulls are observed to be cotemporal with the second peak in current density at the neighborhood of $t = 160\ s$. In the following, we describe

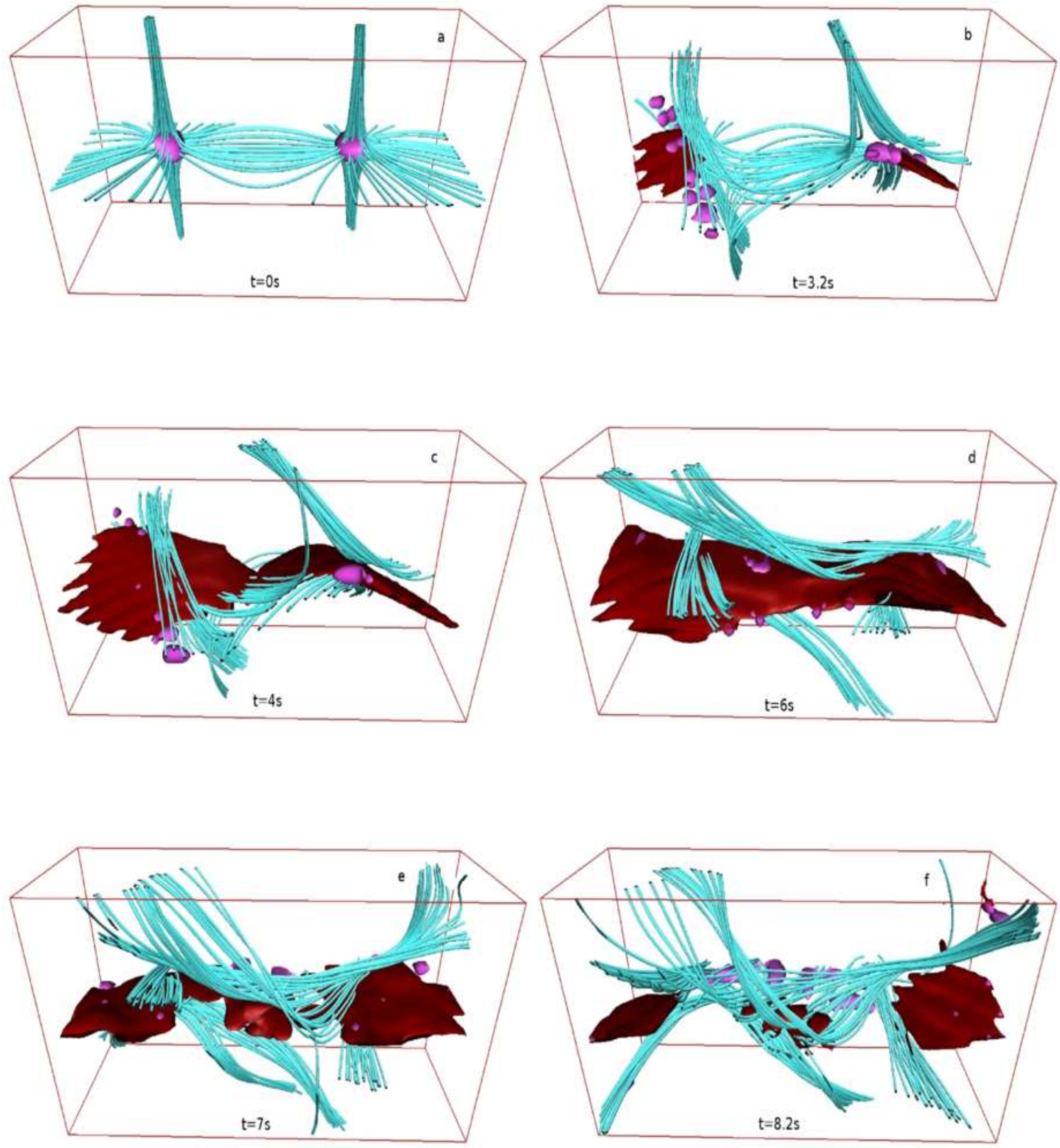

Figure 7.6: Time evolution of 3D magnetic nulls and corresponding spine and fan surfaces, overplotted with isosurface (in red) of current density having a magnitude of 40% of its peak value highlighting the locations where current sheets are forming.

a possible physical scenario resulting in this delayed collapse. It can easily be checked that the x and z components of the initial Lorentz force is zero only in the immediate neighborhood of the null line at $x = z = \pi\ m$. In response to

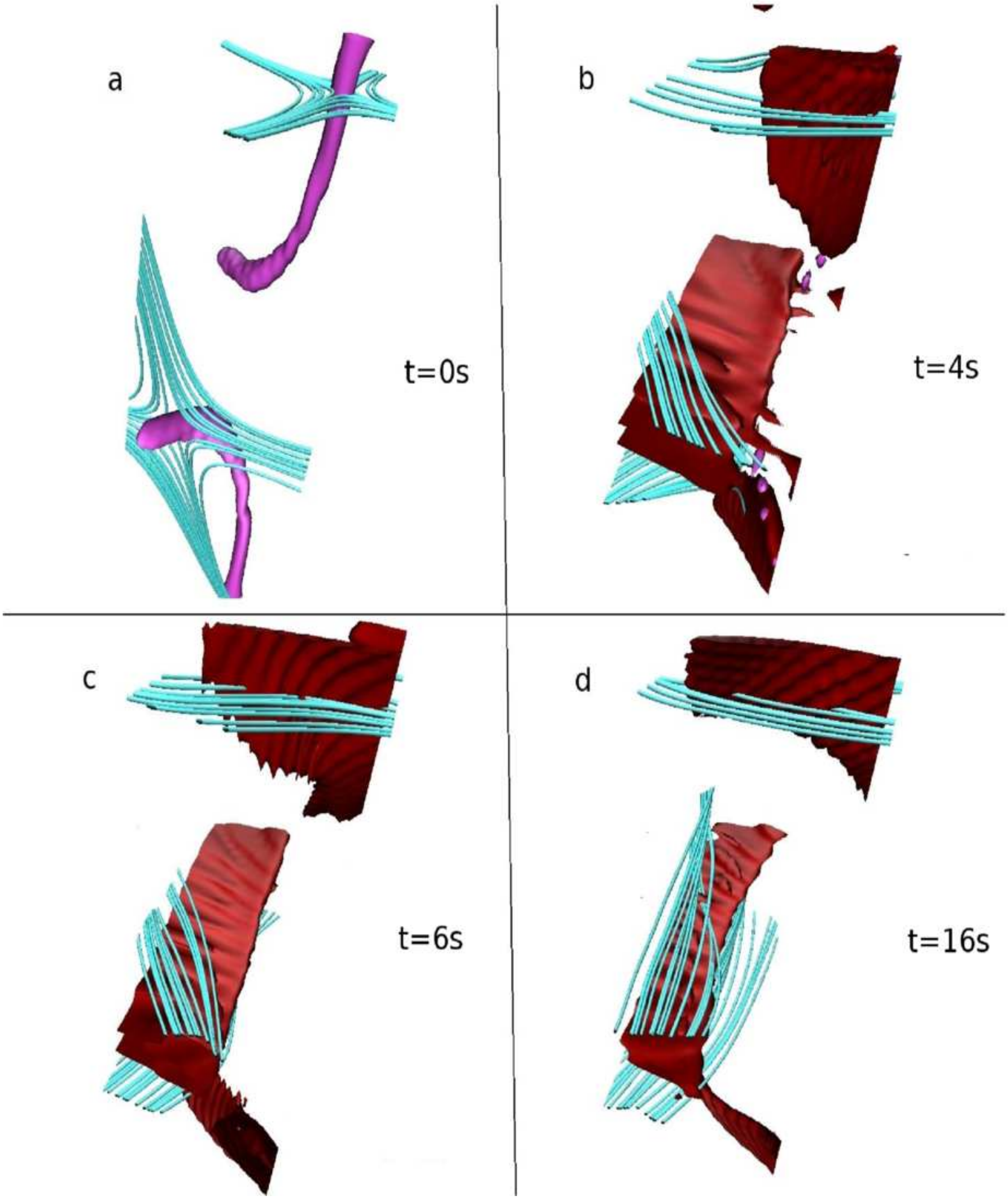

Figure 7.7: History of a pair of adjacent shoe-shaped magnetic nulls and neighboring field lines, overplotted with the same isosurface as in Figure 7.6 to visualize current sheet formations. The viscosity and grid resolution are $\mu = 0.0035\, m^2\, s^{-1}$ and 128^3 respectively.

this nonzero Lorentz force the magnetofluid rotates with larger angular velocity which increases in an outward direction from the y-line and deforms magnetic field lines inhomogeneously at the plane of the 2D null. This increase in rotational kinetic energy is cotemporal with the increase in average kinetic energy plotted in panel *b* of Figure 7.3. The curvature of magnetic field lines and hence the magnetic tension then increases locally around the null at the expense of kinetic energy of plasma motion. This increased magnetic tension then pushes back the plasma in opposite direction at the quasi-steady phase of evolution where the kinetic energy and hence the force acting on a fluid element is almost zero. The resulting motion is the observed to-and-fro oscillations of the field lines near the 2D null depicted in panels *b* and *c* of Figure 7.8. More importantly, during each back and forth rotation a fraction of kinetic energy is dissipated via viscosity. When this kinetic energy is mostly dissipated i.e, at the onset of the quasi-steady phase, the rotational oscillations cease and the X-type configuration remains with asymmetric field structure (Fig. 7.8, panel *d*) having different curvatures of magnetic field in adjacent quadrants. Because of this asymmetry, the imbalance in magnetic tension then pushes the magnetofluid from two opposite quadrants towards each other. Subsequently, due to the frozen-in condition, the magnetic pressure and hence field intensity increases locally at the high curvature region at each quadrant. When the field intensity becomes sufficiently strong, the optical analogy dictates the magnetic field lines to become concave toward this local maximum along with the development of an appreciable current density. Panel *e* of Figure 7.8 depicts such concave field lines as anticipated in [3]. The boundary of the overplotted ellipse traces the field lines to provide a ready reckoning of this concavity. Finally, at $t = 160$ s the X-type neutral point is squashed to two Y-type neutral points with an extended CS, shown in Figure 7.8, panel f. This squashing is more effective in our calculations since the flow is volume preserving, so that a compression along two quadrants would result in stretching of the perpendicular quadrants. Since at different constant $y-$planes the field lines have different orientations in the neighborhood of a null, the corresponding CS is twisted (Fig. 7.9) and decays through the reconnection to generate the second peak in current density.

The above process of CS formation through squashing together two initially separate regions of field (two quadrants of an X-type null), producing a gap in the

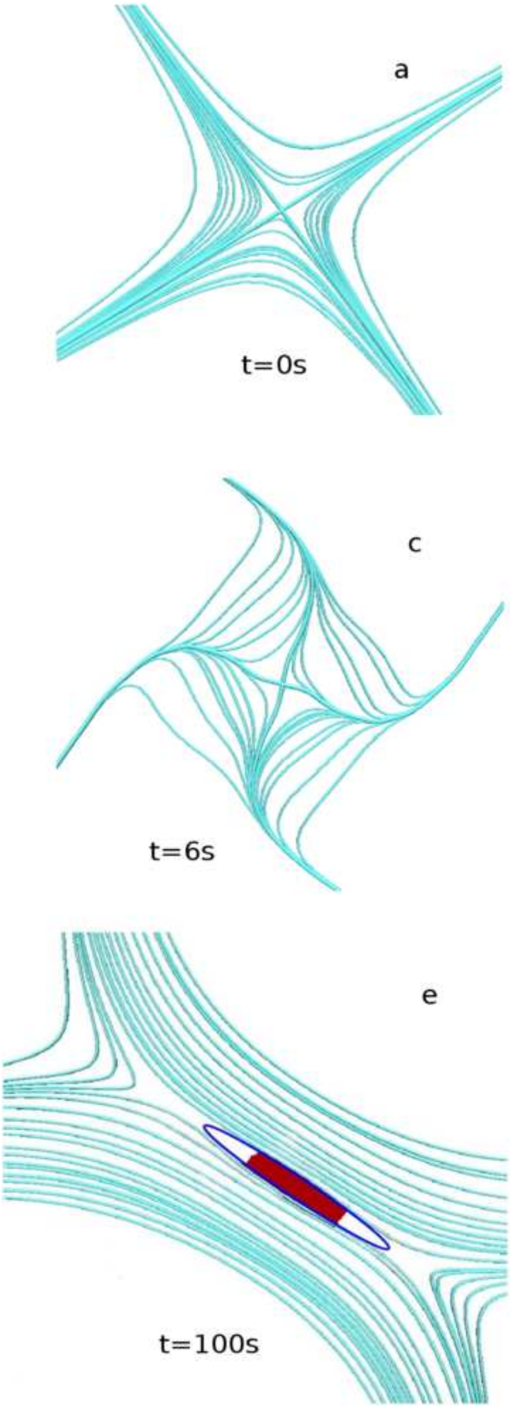

Figure 7.8: Panels $a-f$ illustrate the time evolution of a representative 2D magnetic null located at $x = \pi\ m, y = 3\pi/2\ m, z = \pi\ m$ and null fields overplotted with isosurfaces (in red) of 40% of $\mid \mathbf{J} \mid_{max}$ at the second peak in current density, appearance of which at $t = 160\ s$ confirms the formation of current sheet at the Y-type null. The concavity of the field lines is marked by ellipse, shown in panel e.

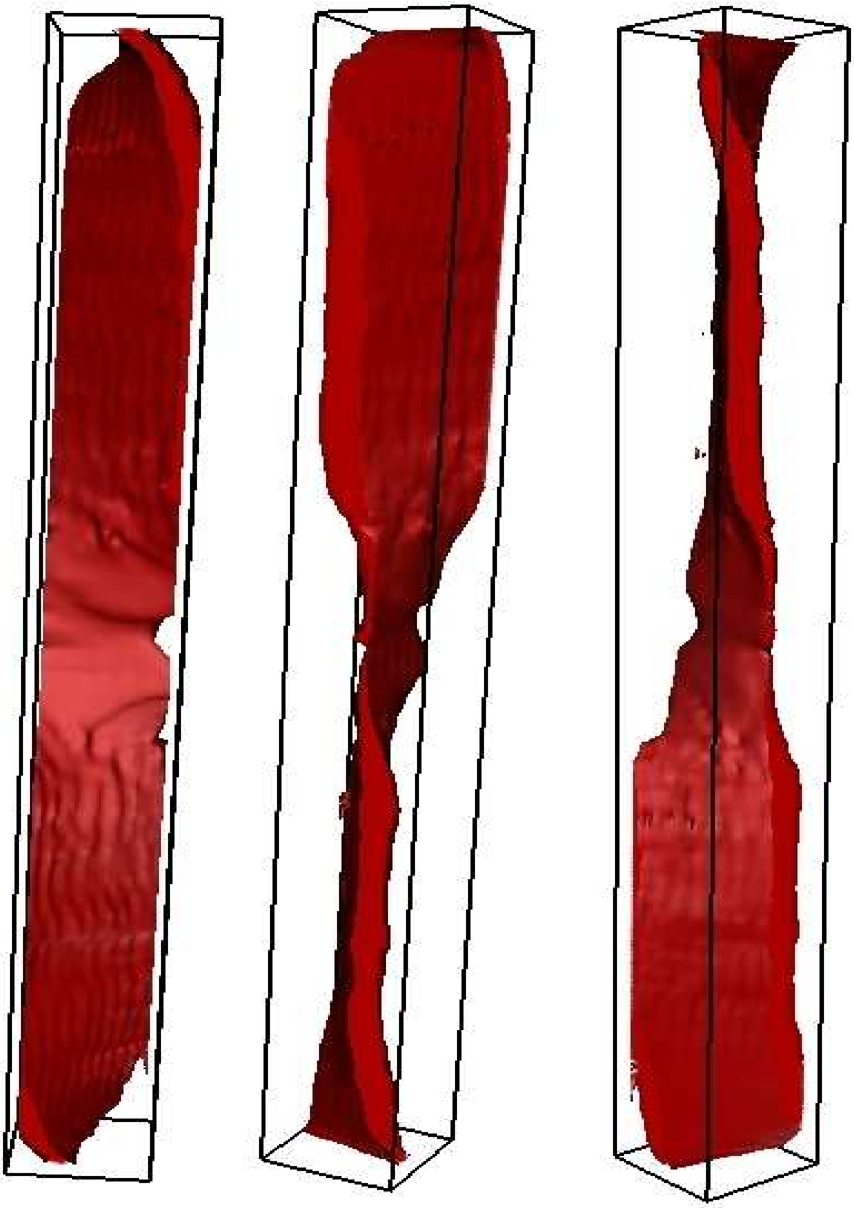

Figure 7.9: Current sheet along y and $x = z = \pi\ m$ at $t = 160\ s$ represented by the same isosurface of current density as in Figure 7.8, plotted for three different viewing angles to emphasize its twisted nature.

intervening flux surfaces (the region of exclusion marked by the ellipse) converting an X-type null to two Y-type nulls then raises the important question on the relative effects of viscosity and magnetic diffusivity in determining the thickness of the CS. The hydrodynamics of these thinning CSs has been studied analytically by solving Navier-Stokes equations in an idealized scenario of two flux surfaces approaching each other under differential kinetic pressure [3]. The minimum thickness of a CS was found to be determined by magnetic diffusivity instead of viscosity even in the case of the latter being larger in magnitude. Simulations presented here do not have the scope to explore this finding because of an absence of physical resistivity, however a coarse estimation is possible. We note that the thickness of the CS formed in panel f of Figure 7.8 is actually limited by the fixed grid resolution of the 128^3 computation that is otherwise well resolved. Scales at the grid resolution are dumped selectively by the residual dissipation of MPDATA [143]. This is apparent from the peaked profile of the numerical deviations in both magnetic and kinetic energy balances in the neighborhood of $t = 160\ s$, plotted in Figure 7.4, panel c. The smallest scales then are the ones below which the residual dissipation dominates and the numerical deviations in energy balance decrease. Assuming the effect of residual dissipation on kinetic and magnetic energy rates to be comparable, the observed higher value of numerical deviation in change in magnetic energy over kinetic energy makes magnetic diffusion to be more effective than its viscous counterpart as concluded in reference [3]. But above arguments are only qualitative and require further numerical investigations.

7.3 Numerical Experiments- II: Open System

7.3.1 Initial Value Problem

As a continuation of the simulations presented in previous section for an isolated system, here we perform the simulations for an open system. For the purpose, the initial magnetic field is again constructed by superposing two linear force-free fields $\mathbf{B}_1$ and $\mathbf{B}_2$ satisfying equations (7.2.1). A solution of equation (7.2.2) for an open system pertaining to the magnetic loops observed in the solar corona is discussed in chapter 6 and in the reference [137]. For completeness in presentation, here we rewrite the components of $\mathbf{B}'$ which is obtained for the positive half-space ($z \geq 0$) of a Cartesian coordinate system having periodicity along the laterals (x and y) as

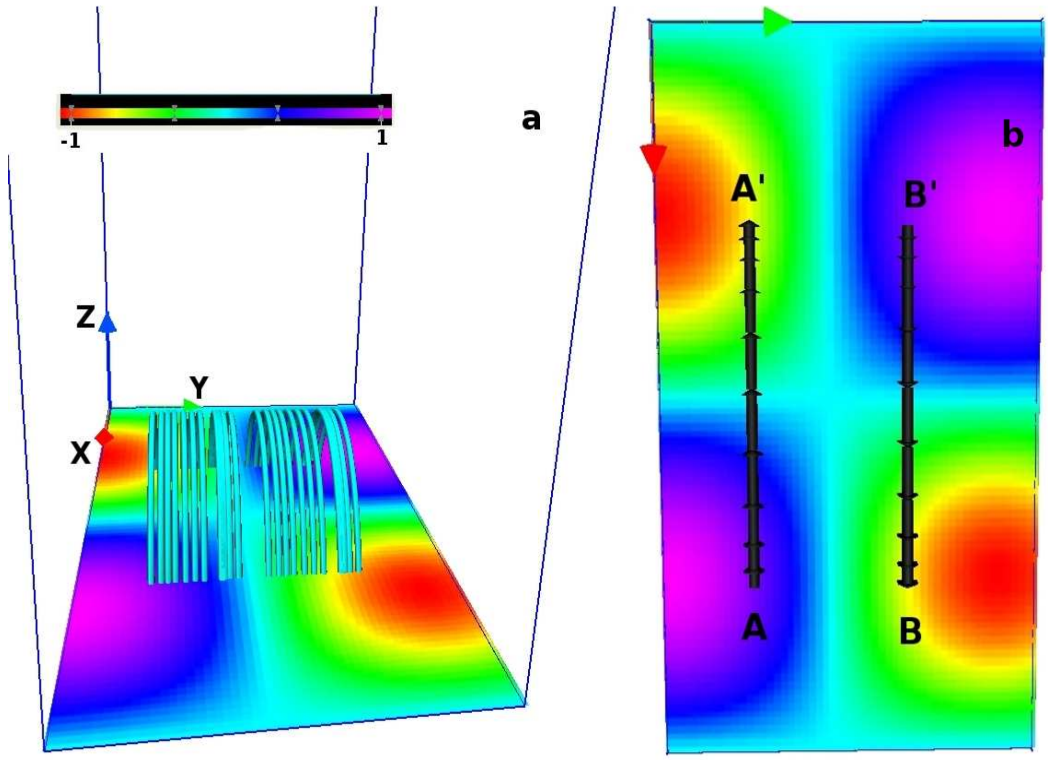

Figure 7.10: Panel a represents the geometry of magnetic field lines for initial field $\mathbf{H}^1$. In panel b, we plot the projections of a selected pair of field lines on the xy-plane at $z = 0\ m$. The symbols $A,\ A'$ and $B,\ B'$ mark two opposite polarity footpoint pairs. The projections being straight lines, confirm that the field lines for $\mathbf{H}^1$ are untwisted. Both panels are overlaid with contours of H_z^1 to indicate the polarities of footpoints. The color code represents the magnitude of H_z^1 (in T).

$$
\begin{aligned}
B_x &= B_0\Bigg[(1+\gamma)\cos\left(x\sqrt{\frac{1+\alpha^2}{2}}\right)\cos\left(y\sqrt{\frac{1+\alpha^2}{2}}\right) \\
&\quad + \frac{(1-\gamma)(1+\alpha^2)}{2\alpha}\sin\left(x\sqrt{\frac{1+\alpha^2}{2}}\right)\sin\left(y\sqrt{\frac{1+\alpha^2}{2}}\right)\Bigg]\exp(-z), \\
B_y &= B_0\Bigg[(1-\gamma)\frac{\alpha^2-1}{2\alpha} \\
&\quad \times\cos\left(x\sqrt{\frac{1+\alpha^2}{2}}\right)\cos\left(y\sqrt{\frac{1+\alpha^2}{2}}\right)\Bigg]\exp(-z), \\
B_z &= -B_0\sqrt{\frac{1+\alpha^2}{2}}\Bigg[(1+\gamma)\sin\left(x\sqrt{\frac{1+\alpha^2}{2}}\right)\cos\left(y\sqrt{\frac{1+\alpha^2}{2}}\right) \\
&\quad - \frac{1-\gamma}{\alpha}\cos\left(x\sqrt{\frac{1+\alpha^2}{2}}\right)\sin\left(y\sqrt{\frac{1+\alpha^2}{2}}\right)\Bigg]\exp(-z),
\end{aligned} \tag{7.3.1}
$$

where B_0 is an arbitrary constant amplitude. In chapter 6, we have established that the field line topology depends on the parameters α and γ. Noting this importance, in the following we discuss three cases of gradually increasing geometric complexity, with the interacting sets of magnetic field lines of $\mathbf{B}'$ characterized by different values of α and γ and, thus, distinct topology and footprint geometry. The case i is the simplest, assuming mirror symmetry and untwisted field lines. In the case ii, the mirror symmetry of the case i is disturbed by a relative translation of the reflected magnetic field lines (hereafter, glide symmetry) yet the field lines are kept untwisted. The translation is so chosen as to keep the amplitude of the magnetic field at $z = 0$ plane equal but opposite in sign, before and after the symmetry operation. Finally, in case iii the glide symmetry is maintained but the field lines are twisted.

A. Case i: $\alpha = 1$ **and** $\gamma = 1$

With B_0 set to 0.5, the components of $\mathbf{B}'$ are then

$$\begin{aligned} H_x^1 &= \cos(x)\cos(y)\exp(-z), \\ H_y^1 &= 0, \\ H_z^1 &= -\sin(x)\cos(y)\exp(-z). \end{aligned} \tag{7.3.2}$$

The differential equation satisfied by the field lines of a general magnetic field $\mathbf{B}$ in Cartesian coordinates being

$$\begin{aligned} \frac{dx}{ds} &= \frac{B_x}{\mid \mathbf{B} \mid}, \\ \frac{dy}{ds} &= \frac{B_y}{\mid \mathbf{B} \mid}, \\ \frac{dz}{ds} &= \frac{B_z}{\mid \mathbf{B} \mid}, \end{aligned} \tag{7.3.3}$$

with ds as the invariant length; the magnetic field lines of $\mathbf{H}^1$ are tangential to y-

constant surfaces, as depicted in panel a of Figure 7.10. In different illustrations presented here, generally the y direction is restricted to $[0, \pi\ m]$ since similar structure and dynamics is repeated in the region $[\pi, 2\pi\ m]$. Also, The existence of two field reversal layers at $y = \pi/2\ m$ and $y = 3\pi/2\ m$ is evident from equations (7.3.2). The polarity inversion lines (PILs), defined as the lines on which $B_z = 0\ T$ on the xy-plane at $z = 0\ m$, are straight lines; located at $x = \pi\ m$ and are perpendicular to the field reversal layers.

The field lines being co-planar with y-constant planes, are untwisted and exert a Lorentz force $\mathbf{L}^1$

$$
\begin{aligned}
L_x^1 &= 0,\\
L_y^1 &= 2\sin(y)\cos(y)\exp(-2z),\\
L_z^1 &= 0.
\end{aligned}
\tag{7.3.4}
$$

Two observations are noteworthy. In contrast to the magnetic fields of isolated system used in the section 7.2, the bipolar field lines lack any two or three dimensional neutral point. Second, the location of footpoints (intersections of field lines with the xy-plane at $z = 0\ m$) with opposite polarities satisfy mirror symmetry across the field reversal layers. For better clarity, in panel b we depict projections of two field lines situated at either side of the field reversal layer at $y = \pi/2\ m$, on the xy-plane at $z = 0\ m$. The corresponding pairs of footpoints are denoted by symbols A, A' and B, B' respectively. These projections being straight lines, additionally confirms $\mathbf{H}^1$ to be untwisted. Further, both panels are overlaid with contours of H_z^1 to depict polarities of footpoints located at different regions.

B. Case ii. $\alpha = 1$ **and** $\gamma = 0.8$

We set the amplitude $B_0 = 0.5$. The corresponding $\mathbf{B}'$, termed $\mathbf{H}^2$, then has components

$$
\begin{aligned}
H_x^2 &= [0.9\cos(x)\cos(y) + 0.1\sin(x)\sin(y)]\exp(-z),\\
H_y^2 &= 0,\\
H_z^2 &= -[0.9\sin(x)\cos(y) - 0.1\cos(x)\sin(y)]\exp(-z).
\end{aligned}
\tag{7.3.5}
$$

and yields a Lorentz force

$$
\begin{aligned}
L_x^2 &= 0,\\
L_y^2 &= 1.6\sin(y)\cos(y)\exp(-2z),\\
L_z^2 &= 0.
\end{aligned}
\tag{7.3.6}
$$

Figure 7.11, panel a, illustrates the magnetic field lines of $\mathbf{H}^2$ overlaid with contours of H_z^2 at the xy-plane at $z = 0\ m$. From the figure, it is explicit that the field lines are untwisted as before — once again because of $H_y^2 = 0$, but in contrast to the Case i the PILs are curved lines. While constructing the field lines, the glide symmetry is ensured by demanding the footpoints reflected about the xz-plane at $y = \pi/2\ m$ to be relatively displaced by an amount Δx in the x-direction, implying the identities

$$
\begin{aligned}
H_x^2(x, y, 0) &= -H_x^2(x + \Delta x, \pi - y, 0),\\
H_z^2(x, y, 0) &= -H_z^2(x + \Delta x, \pi - y, 0),
\end{aligned}
\tag{7.3.7}
$$

to make $|\mathbf{H}^2|_{z=0}$ equal for a pair of opposite polarity footpoints, before and after the symmetry operation. To calculate this Δx we plot variations of $H_x^2(x, y, 0)$ and $-H_x^2(x, \pi - y, 0)$ with x, for a given y. The plots then generate two spatially shifted sinusoidal curves, illustrated in panel b of Fig. 7.11. We then identify the Δx with this spatial shift — the offset required to exactly superimpose one curve on the other. A similar procedure using plots of $H_z^2(x, y, 0)$ and $-H_z^2(x, \pi - y, 0)$

yields the same Δx. The magnetic field lines illustrated in panel a of Figure 7.11 are constructed with $y = 2\pi/5\ m$ and a relative displacement $\Delta x = \pi/5\ m$. The presence of an identical glide plane at $y = 3\pi/2\ m$ is apparent because of the periodicity in the y-direction.

C. Case iii. $\alpha = \sqrt{7}$ **and** $\gamma = .5$

The components of $\mathbf{B}'$, with a selection of $B_0 = 1$, are

$$\begin{aligned} H_x^3 &= [1.5\cos(2x)\cos(2y) + \frac{2}{\sqrt{7}}\sin(2x)\sin(2y)]\exp(-z), \\ H_y^3 &= [\frac{1.75}{\sqrt{7}}\cos(2x)\cos(2y)]\exp(-z), \\ H_z^3 &= -[3\sin(2x)\cos(2y) - \frac{1}{\sqrt{7}}\cos(2x)\sin(2y)]\exp(-z). \end{aligned} \tag{7.3.8}$$

exerting a Lorentz force

$$\begin{aligned} L_x^3 &= [-12\sin(2x)\cos(2x)\cos^2(2y)]\exp(-2z), \\ L_y^3 &= [4\sin(2y)\cos(2y)1 + 3\sin^2(2x)]\exp(-2z), \\ L_z^3 &= [-12\cos^2(2x)\cos^2(2y)]\exp(-2z), \end{aligned} \tag{7.3.9}$$

the lateral components of which at the xy-plane at $z = 0\ m$ are plotted in panel d of Figure 7.11. The selection of $\alpha = \sqrt{7}$ is made to keep the computational domain size and hence, the fluid Reynolds number R_F, same as in the previous cases while maintaining the periodicity of the lateral boundaries. The magnetic field lines are illustrated in panel c of Figure 7.11. As opposed to the cases i and ii, $H_y^3 \neq 0$ makes the field lines twisted and hence, their projections on the xy-plane at $z = 0\ m$ are curved lines (Fig. 7.11, panel c). Also, similar to the earlier case, the opposite polarity footpoints satisfy a glide symmetry where one of the reflection planes is located at $y = \pi/4\ m$ and the translation Δx is determined by the identities

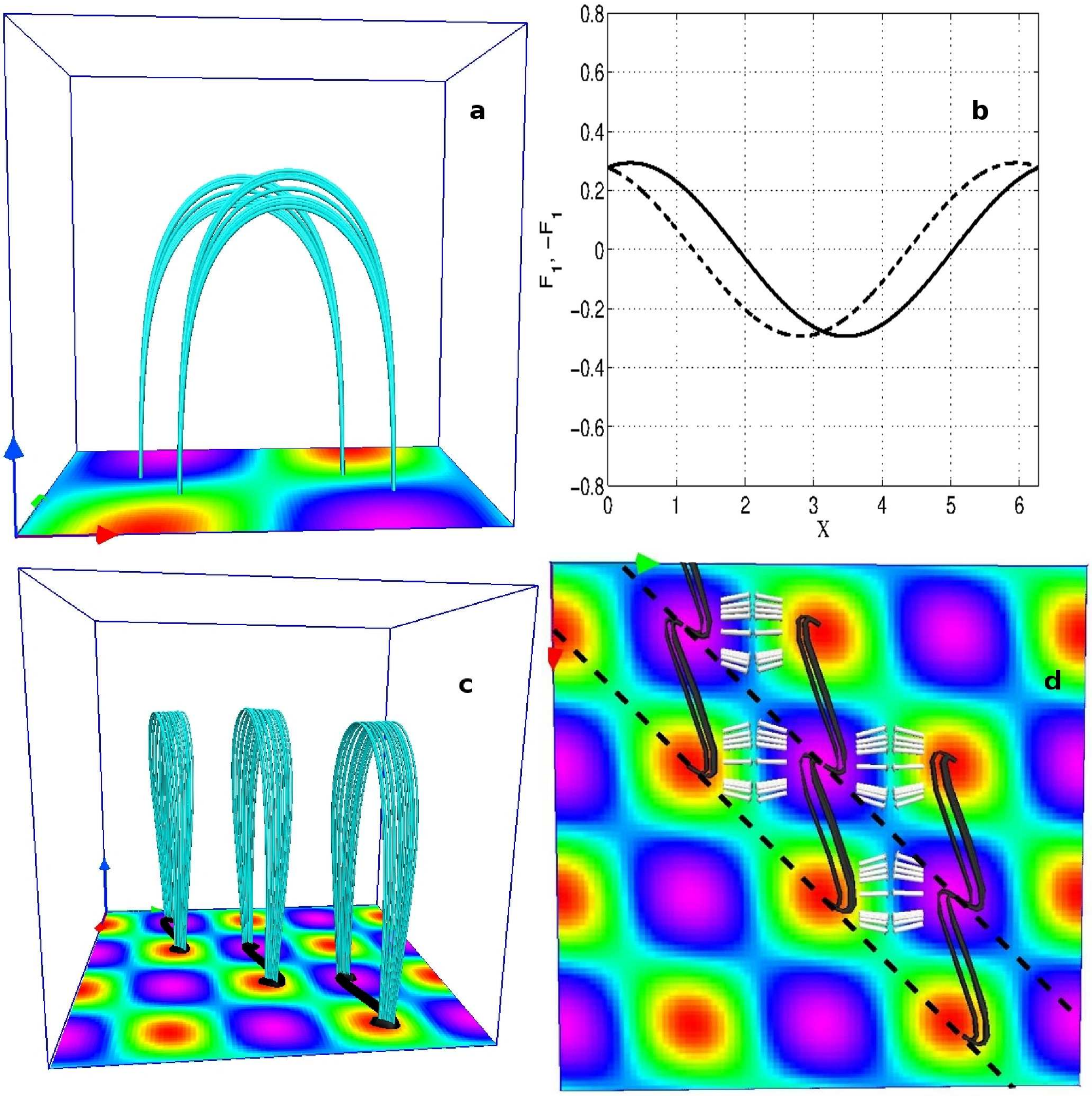

Figure 7.11: Panels a and c illustrate the field lines for initial fields $\mathbf{H}^2$ and $\mathbf{H}^3$ respectively, overlaid with contours H_z^2 and H_z^3 — represented by similar color codes as used in Figure 7.10 with values $-1\ T \leq H_z^2 \leq 1\ T$ and $-3.4\ T \leq H_z^3 \leq 3.4\ T$. Noteworthy is the projections of field lines (in black) of $\mathbf{H}^3$ on the xy-plane at $z = 0\ m$ — to be curved lines, which confirms the corresponding field lines to be twisted. In Panel b the solid line corresponds to $F_1 \equiv H_x^2(x, y, 0)$ (in T) and the dashed line corresponds to $F_2 \equiv -H_x^2(x, \pi - y, 0)$ (in T) with x (in m), for $y = 2\pi/5\ m$. The relative displacement of these two curves gives the shift $\Delta x = \pi/5\ m$. In panel d, we re-plot the projections of $\mathbf{H}^3$ (in Black) on the xy-pane at $z = 0\ m$ overlaid with the vector plots of horizontal component of the Lorentz force $\mathbf{L}^3$ (in Gray). The intersections of the dashed lines with the projections, mark the locations of footpoints of $\mathbf{H}^3$.

$$\begin{aligned} H_x^3(x,y,0) &= -H_x^3(x+\Delta x, \pi/2 - y, 0), \\ H_z^3(x,y,0) &= -H_z^3(x+\Delta x, \pi/2 - y, 0). \end{aligned} \tag{7.3.10}$$

Following the procedure employed in case ii, auxiliary calculations give $\Delta x = \pi/20\ m$ for footpoint coordinate $(x, y, z) = (4\pi/5, 7\pi/20, 0\ m)$. The other glide planes are located at $y = 3\pi/4, 5\pi/4,$ and $7\pi/4\ m$.

We consider the fields $\mathbf{H}^1$, $\mathbf{H}^2$ and, $\mathbf{H}^3$ as the initial magnetic fields for the numerical experiments for an open system.

7.3.2 Simulation Results and Discussions

The simulations are carried out in the $(2\pi)^3$ m^3 domain, resolved with 96^3 uniform grid intervals $\Delta x = \Delta y = \Delta z = 2\pi/95\ m$. The duration times of the simulations for the cases i, ii, and iii, respectively, $T = 48, 128, 128$ s, are resolved with the same temporal increment $\Delta t = 0.032$ s. The density is set to $\rho = 1$ kg m^{-3} and $\mu = 0.004$ m^2 s^{-1}. For the field initial conditions specified in (7.3.2), (7.3.5) and (7.3.8), the magnetofluid is evolved from rest. The lateral boundaries are selected to be periodic. At the vertical boundaries the normal component of mass and magnetic flux is kept fixed to zero. The results of the simulations for the three cases are presented in the following.

A. Case i. $\alpha = 1$ **and** $\gamma = 1$

The overall dynamics of the magnetofluid is demonstrated by the plot of normalized kinetic energy with time (Fig. 7.12). The development of the peak, located at $t \approx 8\ s$, is attributed to an arrest of magnetofluid acceleration by viscous drag. Noticeable is the quasi-steady phase of the evolution, approximately coinciding with the period $t \in (24, 32)$ s. The Figure 7.14 illustrate snapshots of field lines in their important phases of evolution.

To facilitate an understanding of the magnetofluid dynamics, we refer to panel b of Figure 7.10. From equations (7.3.4), the initial Lorentz force $\mathbf{L}^1$ acting

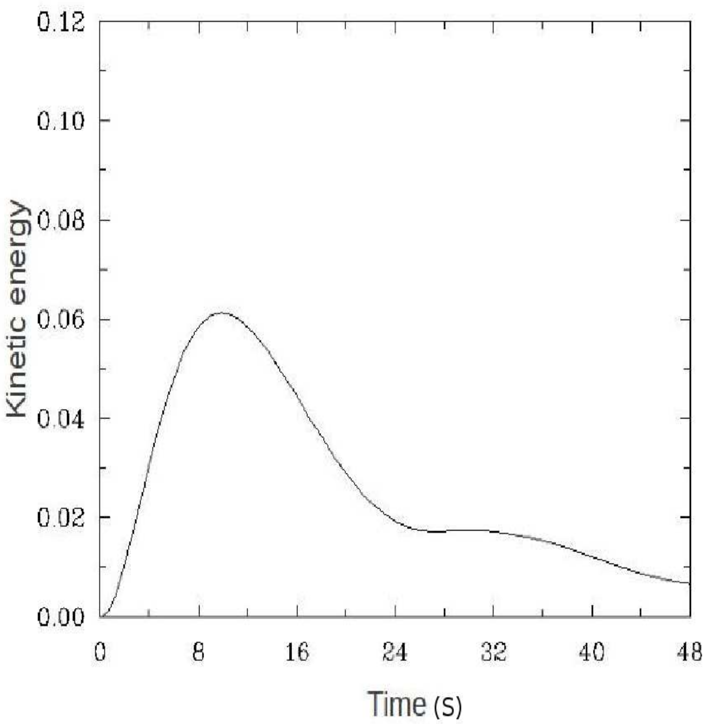

Figure 7.12: History of kinetic energy (normalized to the total initial energy) as the magnetofluid relaxes from the initial state $\mathbf{H}^1$. Important are development of the peak at $t = 8\ s$ and the quasi-steady phase of evolution for $t \in (24, 32)$ s.

along the y-direction, pushes the field lines with footpoint pairs AA' and BB' simultaneously toward the field reversal layer at $y = \pi/2\ m$. Since the magnitude of $\mathbf{L}^1$ for a given field line is maximum at the footpoints (from equations (7.3.4)), the relative approach of any other mirror symmetric points lying on field lines joining $A,\ A'$ and $B,\ B'$ is slower than the relative approach of A toward B and A' toward B'. As a result, two simulatenous reconnections take place between A, B and A', B'; onset by a local sharpening of field gradient — indicated by the rise and fall of the electric current density at the field reversal layer (Fig. 7.13) before and after the reconnections. Such reconnections repeated in time then culminate into generating a magnetic island, complete with the development of two X-type nulls — marked in the Figure 7.14 (panel b) by the symbol $X1$. It is important to note that the post-reconnection open field lines are of quadrupolar geometry. Also from panels c and d, it is apparent that the concavity of the open field lines increases concurrently with an increase in the number of closed field

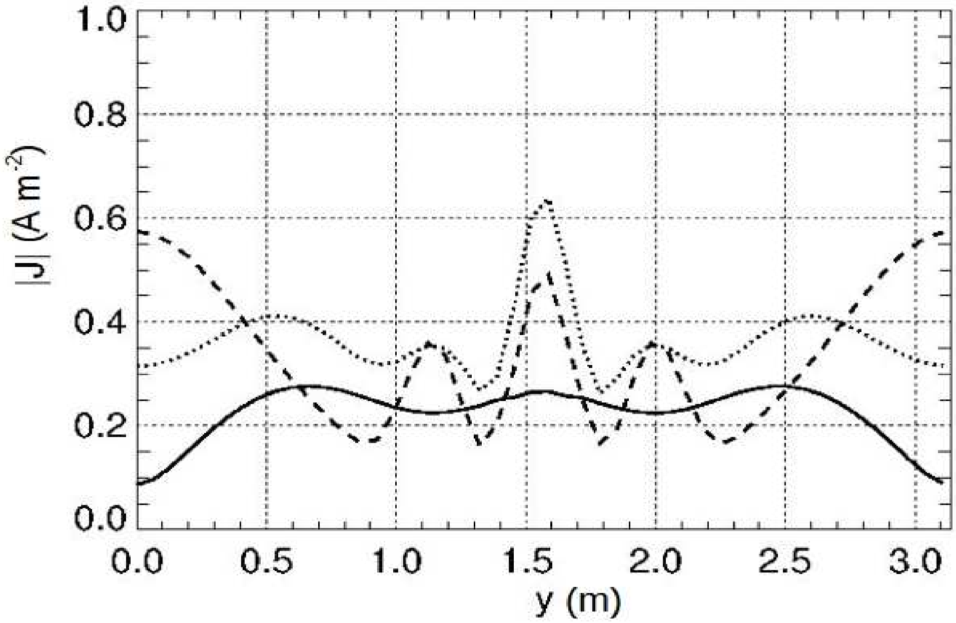

Figure 7.13: Variation of current density | **J** | with y at three time instants; $t = 0$ s (solid line), $t = 1.2$ s (dotted line) and $t = 2.5$ s (dashed line). The plotted | **J** | is calculated for $x = 3\pi/2$ $m, z = 0$ m. The observed rise and fall of | **J** | at the field reversal layer $y = \pi/2$ m is indicative of a CS formation and its subsequent decay.

lines constituting the island. Since an increase in number of closed field lines intensifies $| \mathbf{H}^1 |$ at the island, the increased concaveness of open field lines is then a direct consequence of the Parker's optical analogy [3].

In Figure 7.15 we present magnetic field lines at instances $t = 1.2$ s, $t = 6$ s, and $t = 12$ s, projected on the $x = 3\pi/2$ m plane. The separatrices are drawn in color magenta. Noticeable is the ascend of this X-type neutral point in the vertical direction along with a concurrent increment of the separation between footpoints of the reconnected field lines below the X-type null. Such an ascend of X-type neutral point is also observed in the context of solar flares [105, 106, 150, 151]. A plausible rationale for this ascend, within the scope of our computation is presented in the following.

In our scenario of repeated reconnections, at the initial stages of its evolution,

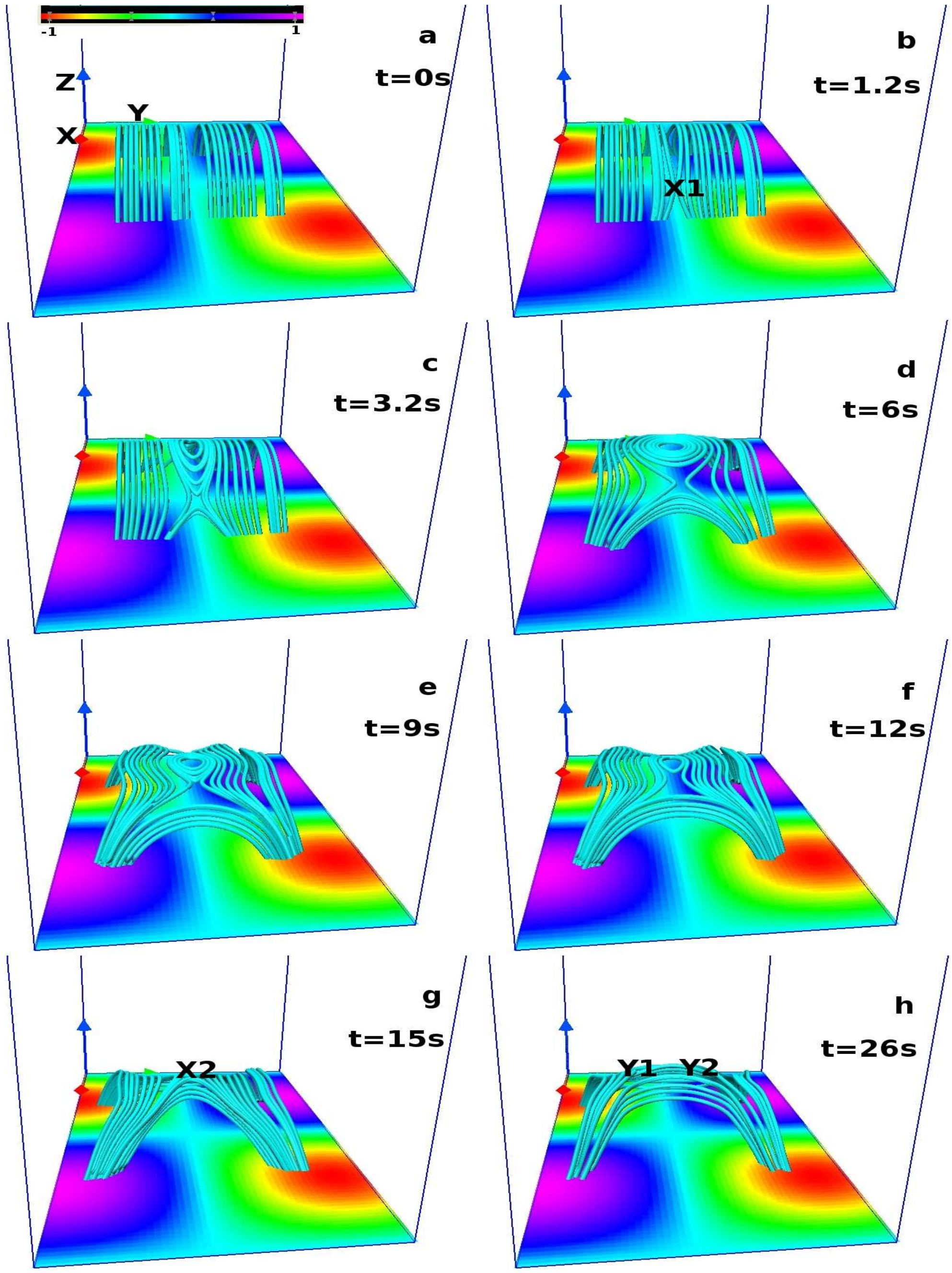

Figure 7.14: Magnetic field lines of $\mathbf{H}^1$ in their important phases of evolution. Each panel of the figure is further overlaid with contours of H_z^1 (color code represents the magnitude in T) at the xy-plane at $z = 0\ m$. Noteworthy are the formations of two X-type nulls (one of the nulls is marked with symbol X1 in panel b), and magnetic island which is most prominent in panel d. Panels g and h mark the onset of a new X-type null (denoted by the symbol X2) which is further squashed into two Y-type neutral points (marked with symbols $Y1$ and $Y2$) at $t = 26\ s$. We also note, this generation of two Y-type nulls are concurrent with the quasi-steady phase of the evolution.

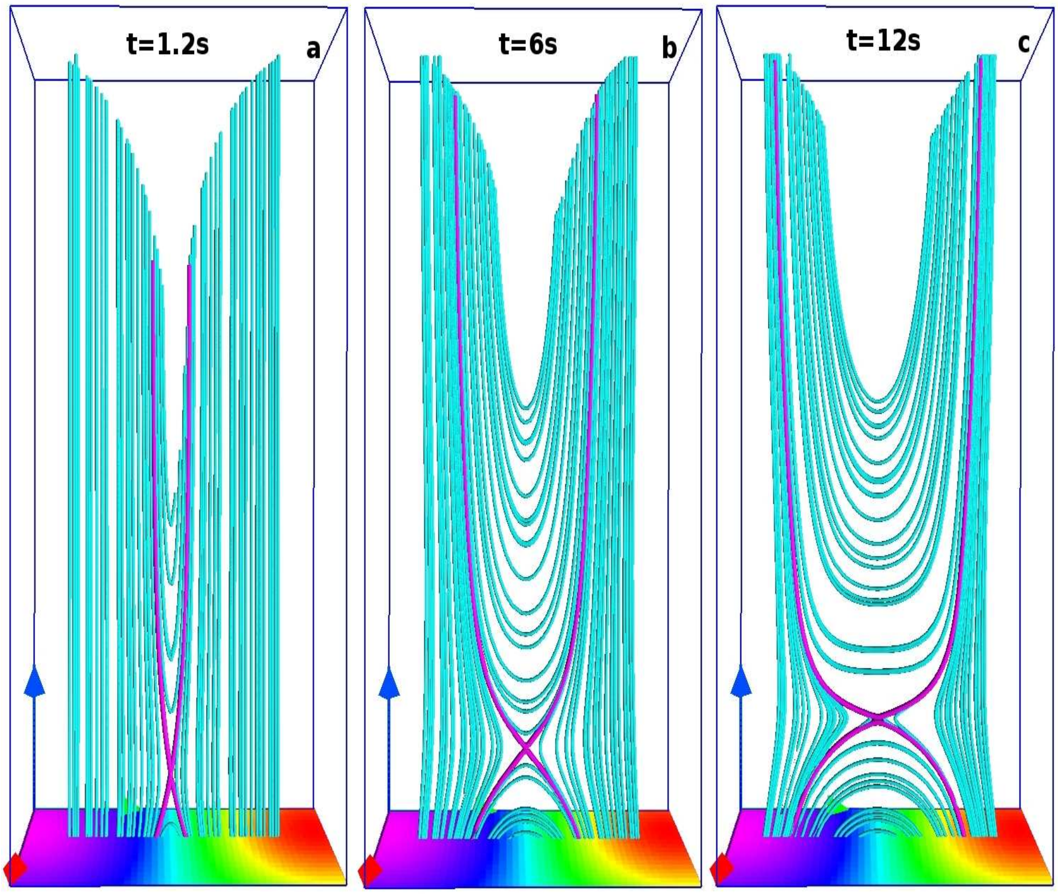

Figure 7.15: Snapshots of field lines for $\mathbf{H}^1$, projected on the yz-plane at $x = 3\pi/2\ m$. Noticeable is the ascend of the X-type neutral point (separatrices of which are drawn in magenta), with time. Also, footpoint separations of reconnected field lines show a concurrent increase in the y direction.

the magnetic island is always pushed at immediate neighborhood of the X-type nulls by the subsequently reconnected field lines. The resulting compression then accounts for the observed ascend. Also the compression being volume preserving because of the solenoidality of flow, the magnetic island becomes more circular with the ascend and, generates an O-type neutral line at $x = \pi\ m, y = \pi/2\ m$ oriented along the z-direction. This circular island then further shrinks self-similarly and decays away at the O-type neutral line (panels d, e and f of Fig. 7.14). As a consequence, the local magnetic pressure decreases and the open field lines oriented along the y direction invade this free space to form a new X-type neutral point (marked by the symbol $X2$), as demonstrated in panel g of Figure 7.14. To explore the subsequent dynamics generated by continuous squashing of this

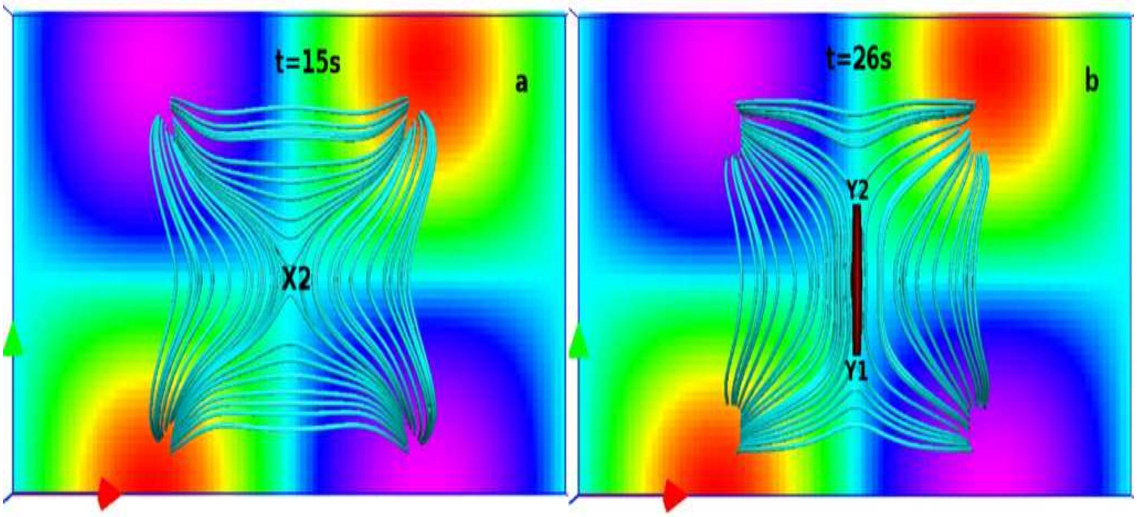

Figure 7.16: Top view of panels g and h of Figure 7.14. The developments of a new X-type null ($X2$ in panel a) and an extended CS (depicted in color red in panel b) is evident.

new X-type null, in Figure 7.16 we present the top view of magnetic field line evolution at instances $t = 15$ s and $t = 26$ s. From this top view, the generation of two Y-type nulls and an extended CS (panel b) is obvious. Noteworthy is the approximate simultaneity of the development of this extended CS with the quasi-steady phase of evolution $t \in (24, 32)$ s, in agreement to one of the analytical requirements of CS formation. Further pushing of field lines then decay this extended CS through MRs, not shown here to keep the number of figures at minimum.

Case ii. $\alpha = 1$ **and** $\gamma = 0.8$

The general evolution of the fluid follows the normalized kinetic energy curve plotted in Figure 7.17. The evolution can clearly be divided into the three following phases. The first phase is characterized by a peak, centered at $t \approx 10$ s, developed as the initial increase in kinetic energy is halted by viscous drag. The second phase is approximately quasi-steady and ranges from $t \in (53, 75)$ s; whereas the third phase shows a monotonic decay of kinetic energy.

The time sequence of magnetic field lines are shown in panels a to f of Figure 7.18. The noteworthy is the development of funnel-shaped helical magnetic field

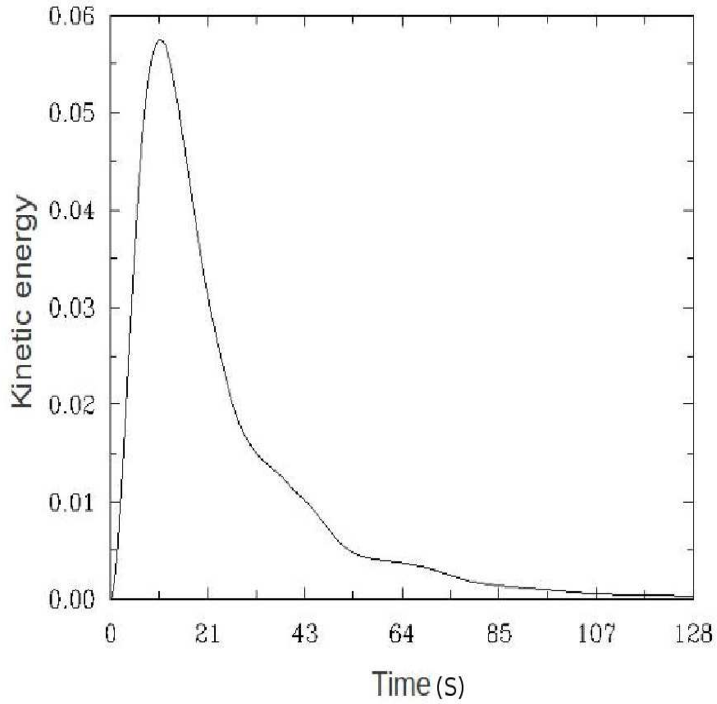

Figure 7.17: History of kinetic energy (normalized to the total initial energy) for the relaxation from the initial state $\mathbf{H}^2$. Important are, development of the peak at $t \approx 10s$, the quasi-steady phase of evolution for $t \in (53, 75)$ s and the subsequent monotonic decay of the kinetic energy.

lines (most prominent at $t = 44$ s), akin to the tornadoes observed at the solar atmosphere. This development of helical field lines coincides with the first phase of the kinetic energy evolution. In panels d and e, we depict a rotation of field lines in a direction opposite to the developed helix. This "untwisting" motion overlaps with the second phase and then decays out eventually. Also noticeable is the absence of extended CSs generated during the evolution.

To elucidate the relevant dynamics of footpoints, in Figure 7.19 we present a schematic of two sets of six initial footpoints lying on the two opposite sides of the glide symmetric plane represented by the central line. The corresponding magnetic field lines then lie on two glide symmetric y-constant planes and are of different heights. The relative polarity of the footpoints are marked by arrows while the length of an arrow measures the intensity of the corresponding magnetic field. The footpoints of field lines with different heights are shifted laterally to

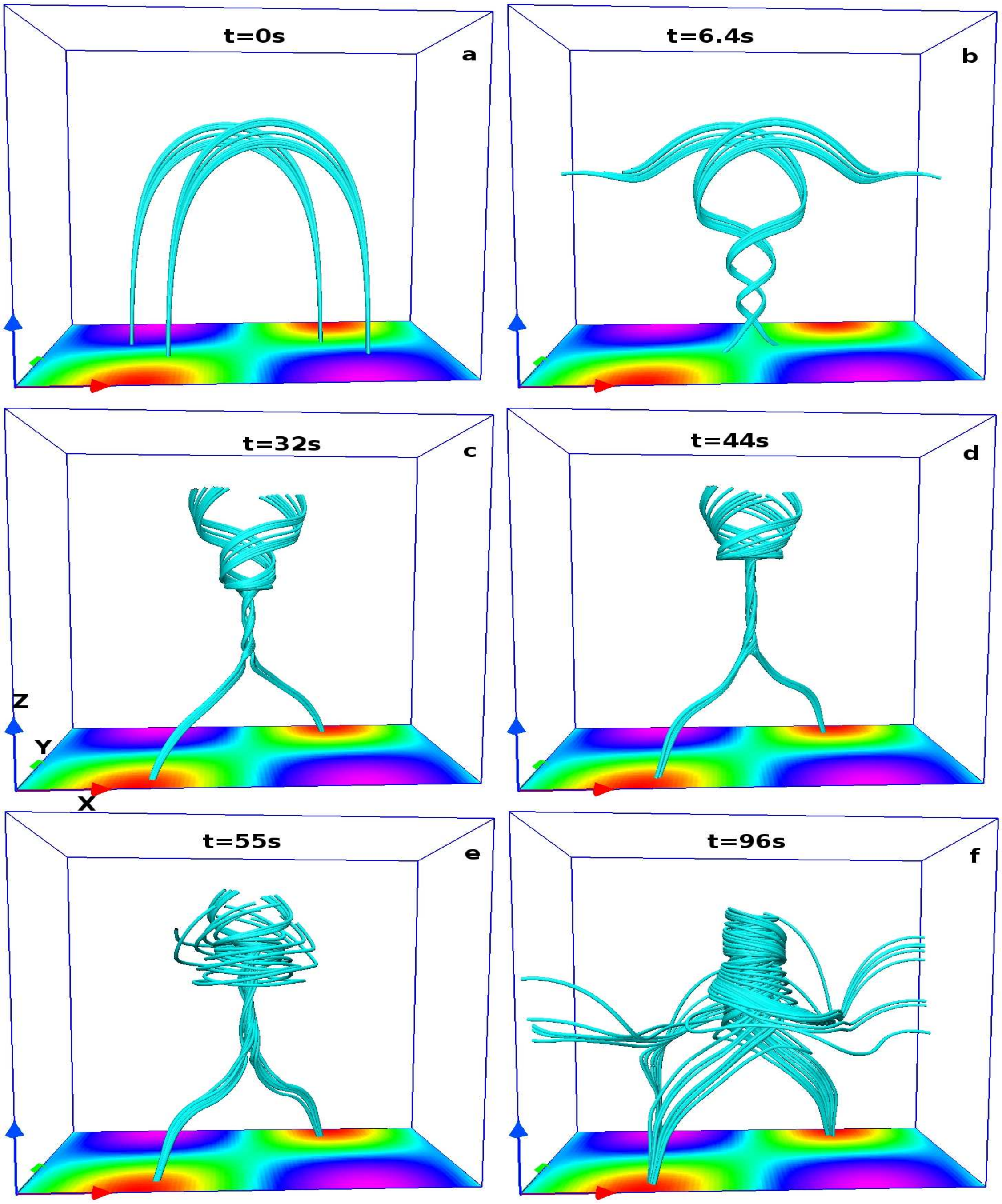

Figure 7.18: Instances of magnetic field lines with $\mathbf{H}^2$ as the initial magnetic field. The overlaying H_z^2 contours (represented by the same color code as used in panel b of Figure 7.11) indicate the glide symmetry of the opposite polarity footpoints situated across the mirror plane $y = \pi/2\ m$. The sequential development of helical field lines, akin to solar tornadoes, is illustrated in panels b to d. Panels e and f represent the "untwisting" motion of the already developed helical field lines illustrated in panel d.

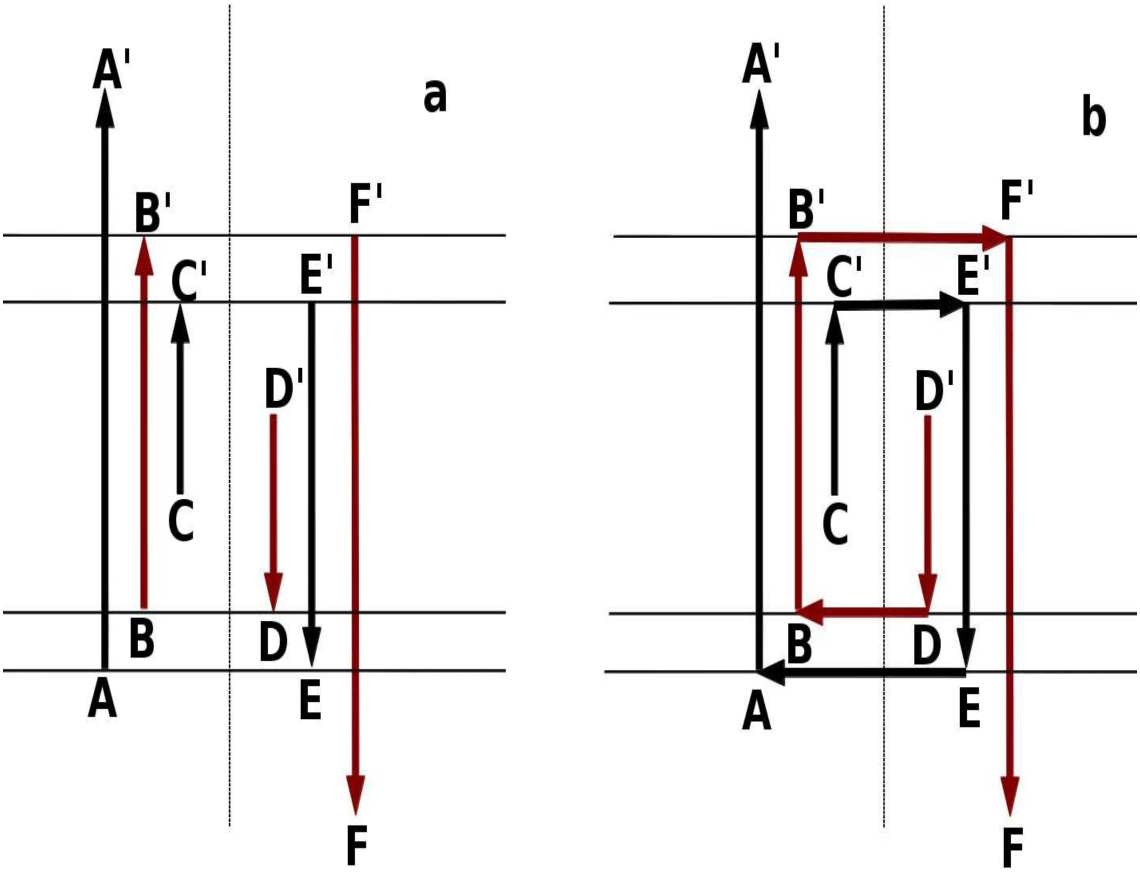

Figure 7.19: The panel a depicts a schematic of the initial field lines for $\mathbf{H}^2$, projected on the xy-plane at $z = 0\ m$. The corresponding footpoints are marked by the pairs A, A'; B, B'; C, C'; D, D'; E, E'; and F, F' respectively. The glide plane is represented by the dotted line situated at the middle. In panel b, the horizontal arrows connect a pair of reconnecting footpoints with opposite polarity.

further enhance the clarity of the schematic. The three pairs of footpoints for the depicted field lines are nomenclatured as A, A'; B, B'; C, C'; D, D'; E, E'; and F, F'.

From equation (7.3.6), the initial Lorentz force $\mathbf{L}^2$ being in the direction y with a sign flip at $y = \pi/2\ m$ – presses the glide-symmetric opposite polarity footpoints toward the $y = \pi/2$ line. This pressing is periodic in the x- direction, being maximum at the two lateral boundaries and zero on the yz-plane at $x = \pi\ m$. In response the footpoints A and E reconnect first, followed by reconnection between E' and C'. The final reconnected field line then, is of the form of a spiral — the projection of which on the xy-plane at $z = 0\ m$ traces out a helical path in

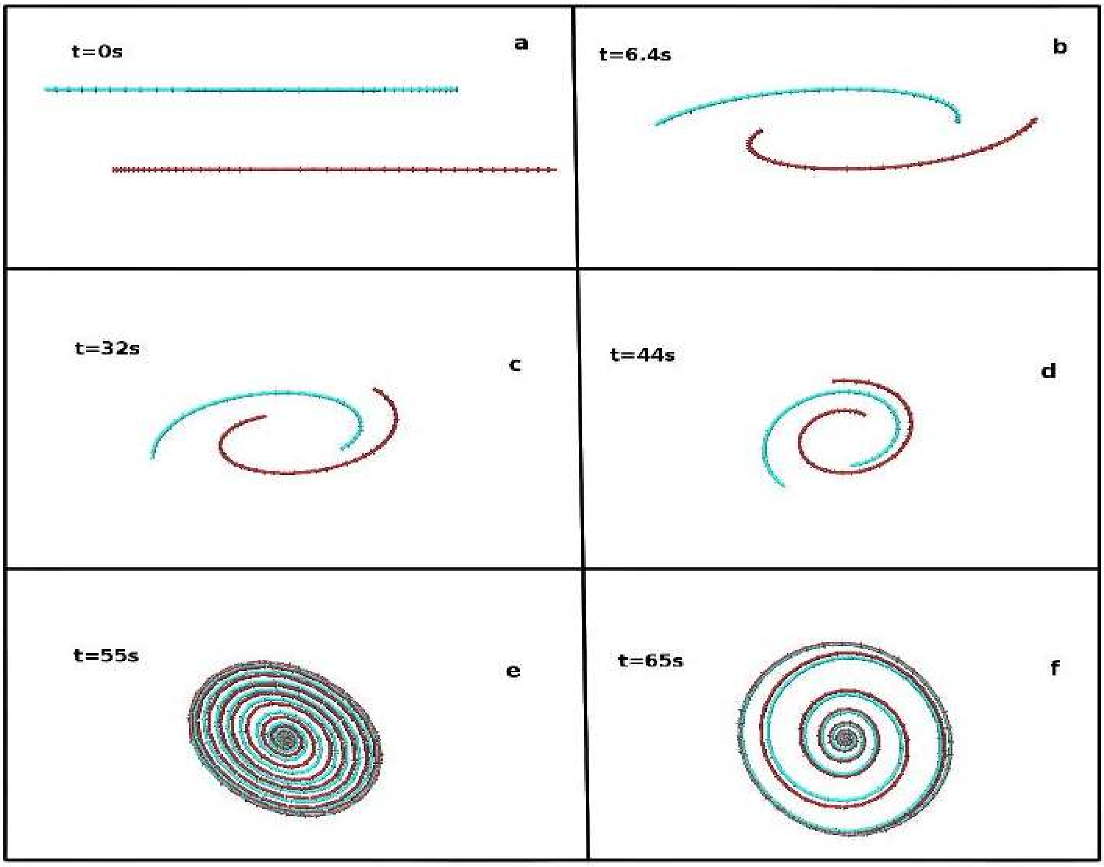

Figure 7.20: The evolution of a pair of glide-symmetric field lines for the field $\mathbf{H}^2$, projected on the xy-plane at $z = \pi/2\ m$. The development of two complementary spirals of similar chiralitity indicates the three dimensional field lines to be helices. Further we note that throughout their evolution, these complementary spirals are in the same direction and hence the geometry of field lines are not favorable for CS formations. The relative decrease in density of field lines at $t = 55$ s (panel e) and $t = 65$ s (panel f) is due to the untwisting motion.

the direction of $CC'E'EAA'$ as illustrated in panel b of Figure 7.19. It is also to be noted that a similar helix with the same chirality develops through footpoint reconnections in the sequence of $F', B'; B, D$. In Figure 7.20, we display the evolution of two such helices projected on the xy-plane at $z = \pi/2\ m$. The spirals marked by the two different colors (red and cyan) correspond to the two helices described above. In panels e and f we depict these spirals at the instances $t = 55$ s and $t = 65$ s coinciding with the quasi-steady phase of the kinetic energy plot. As the spirals maintain their original chirality, two neighboring field lines

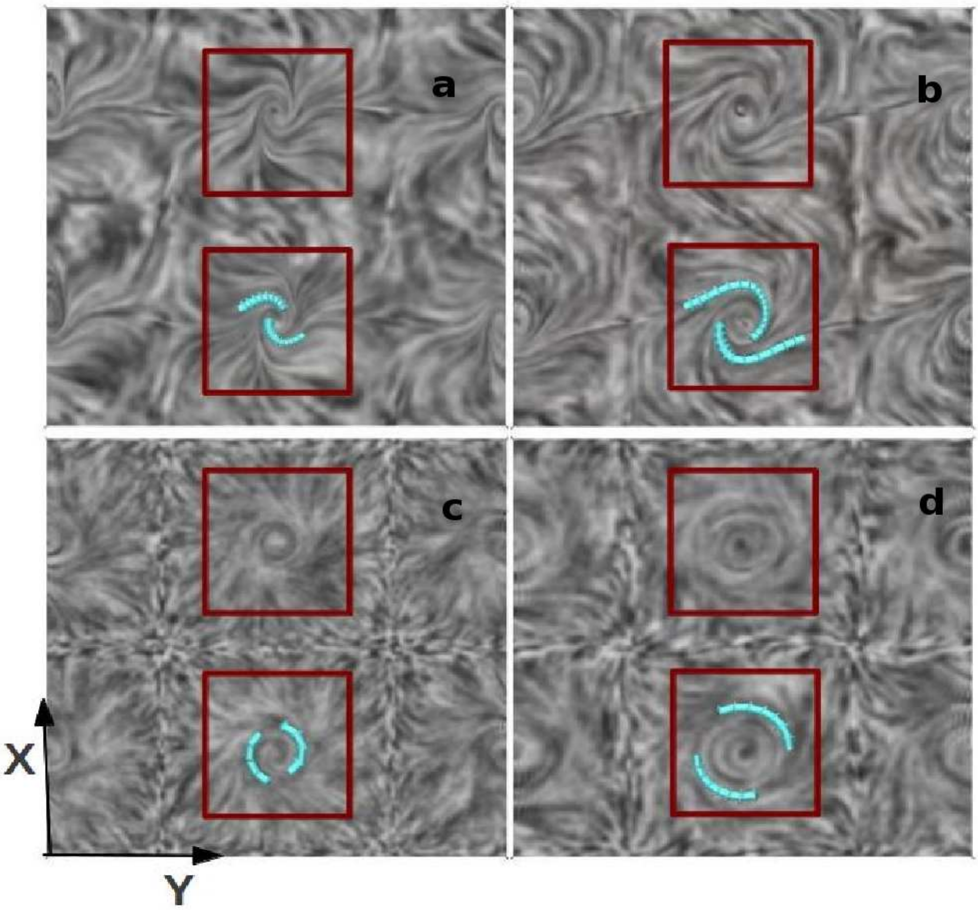

Figure 7.21: The flow images of the velocity generated by the Lorentz force $\mathbf{L}^2$. The panels a and b depict concurrent images ($t = 44$ s) at heights $z = 3\pi/5$, and $6\pi/5$ m respectively, overlaid with velocity field lines (in cyan) projected on the corresponding z-constant levels. Noteworthy are the rotation of the fluid in a clockwise direction as marked by the directions of the plotted velocity field lines; and the increment in size of vortices with height which confirms the development of a funnel shaped structure. In panels c and d, flow images at same heights but later instant $t = 96$ s are shown. The direction of the overlaid velocity field lines (in cyan) show an anticlockwise rotation of the fluid. Here the y coordinate ranges from 0 to 2π m.

are always directed along the same direction — prohibiting formation of extended CSs in absence of a favorable magnetic geometry.

The helical motion of the magnetofluid is further illustrated in Figure 7.21 through the image-based flow visualization technique [152], presented for different vertical levels overlaid with velocity field lines. In confirmation to the

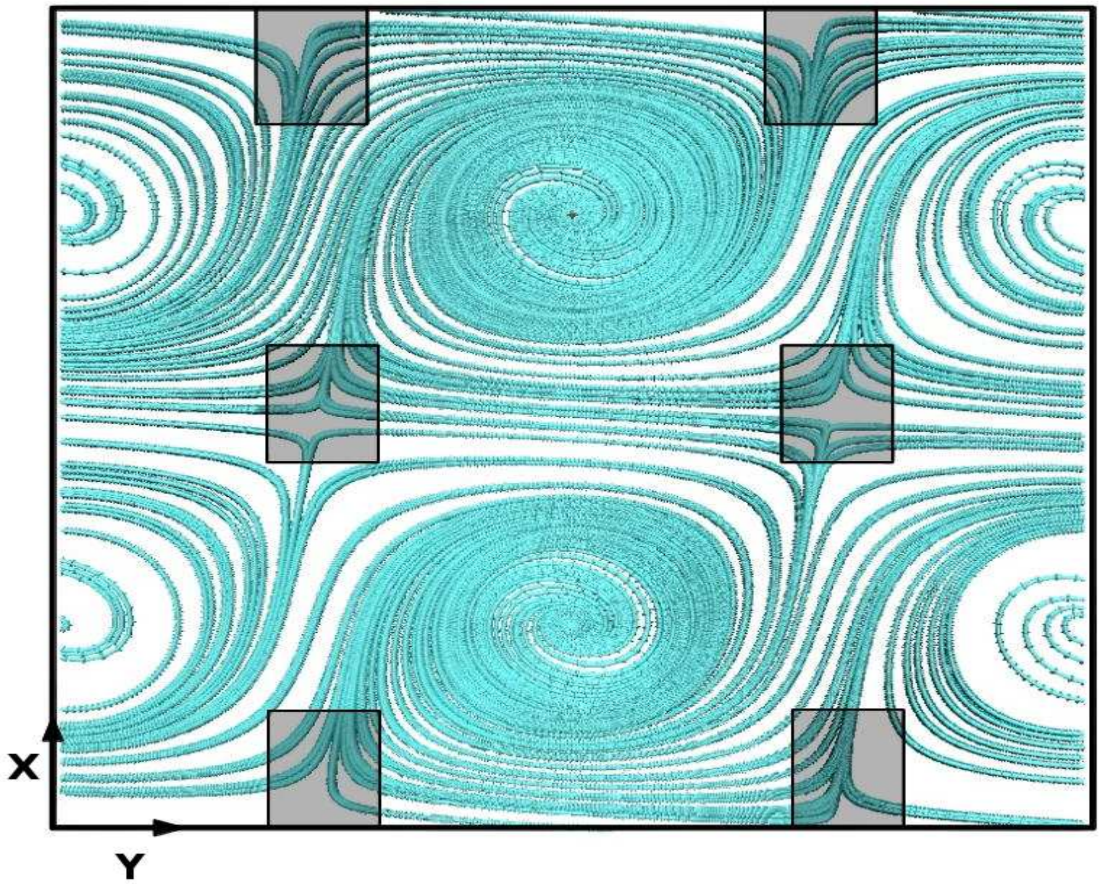

Figure 7.22: Plot of magnetic field lines at $t = 51$ s projected on the xy-plane at $z = 6\pi/5$ m, extended from 0 to 2π m in the y direction. The rectangular patches represent reconnection regions.

twisting motion and the resulting funnel-shape, the figure clearly shows swirls of magnetofluid with size increasing along the vertical.

Moreover, the simulated untwisting motion of previously twisted magnetic field lines (panels e and f) have also been observed in solar tornadoes [116]. For a plausible mechanism of this untwisting motion, we recognize that a viscously damped torsional Alfven wave propagating along the vertical is generated by rotation of field lines with a given chirality. The resulting increase in intensity of the lateral component of magnetic field at a z-constant plane then increases the corresponding magnetic pressure. This increased magnetic pressure pushes out the neighboring magnetic field lines more toward the reconnection regions resembling X-type neutral points situated on the z-constant plane — marked by rectangular patches centered at $(x, y) = (\pi, \pi/2\ m), (\pi, 3\pi/2\ m), (0, \pi/2\ m), (0, 3\pi/2\ m)$ (Fig. 7.22). The subsequent magnetic reconnections then generate counter-clockwise motion of the magnetic field lines as indicated from the plot of the velocity field lines shown in Figure 7.21. Because of this counter-clockwise motion, magnetic field lines first untwist, and then subsequently develop twist with an opposite chirality as demonstrated in Figure 7.18.

C. Case iii. $\alpha = \sqrt{7}$ **and** $\gamma = 0.5$

The overall evolution of the fluid is represented by the history of normalized kinetic energy, plotted in panels a and b of Figure 7.23. Based on these plots, the dynamics of the fluid can coarsely be separated out into four overlapping periods ranging from $t \in (0, 44)$ s, $t \in (44, 72)$ s, $t \in (72, 109)$ s and $t \geq 109$ s. The formation of the first peak in kinetic energy (panel a) is attributed once again to a viscous arrest of increasing kinetic energy of the fluid. Also to be observed are the quasi-steady evolution in the period $t \in (44, 72)$ s, and formation of a second peak in kinetic energy at $t \in (72, 109)$ s.

In Figure 7.24 we depict topologies of evolving magnetic field lines in the period $t \in (0, 51)$ s which overshoots into the onset of the quasi-steady phase. Noteworthy in the depictions is the generation of magnetic field lines which are detached from xy-plane at $z = 0\ m$ and are topologically similar to magnetic flux rope. Because of the inherent complexity in constructing three dimensional field line plots, the subsequent evolution of magnetic field lines is described in Figure 7.25 in terms of their projections on different x-constant planes. The corresponding time period include the quasi-steady phase and the formation of second peak in kinetic energy. An important feature in this period is the formation of an extended CS, depicted by contours of $\mid \mathbf{J}^3 \mid$ in color green, which increases in length along with a simultaneous rise of the flux rope (panels c to d).

Toward an explanation of the evolution, from the expression of the Lorentz force $\mathbf{L}^3$ we note that its direction at the footpoints for any pair of two opposite polarity glide symmetric magnetic field lines about the constant planes $y =$

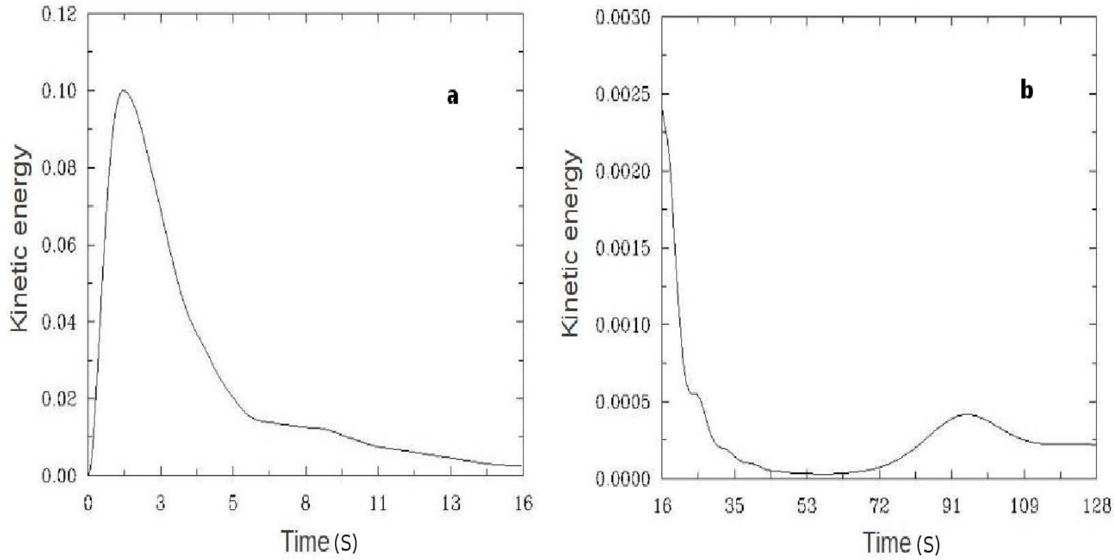

Figure 7.23: Time evolution of kinetic energy of the magnetofluid (normalized to the initial total energy) as the fluid relaxes from the initial field $\mathbf{H}^3$. Panels a and b depict the evolution in two consecutive overlapping ranges. The important features are; the formation of first peak in kinetic energy at $t \approx 1.5$ s, quasi-steady evolution in the period $t \in (44, 72)$ s, and development of a second peak in kinetic energy at $t \approx 91$ s.

$\pi/4, 3\pi/4, 5\pi/4, 7\pi/4$ m, is not favorable for MRs. Instead, $\mathbf{L}^3$ favors a pair of same polarity glide symmetric magnetic field lines to be pushed toward each other. To explore the underlying dynamics then, we consider a set of selected glide symmetric magnetic field lines with the same polarity and located across the glide planes $y = 3\pi/4$ m and $y = 5\pi/4$ m. The field lines represented by the color magenta join two footpoint regions with larger H_z^3 than the inner field lines represented by the color gray. From Figure 7.11 panel d, we note that the initial Lorentz force pushes the inner field lines in the general direction of the glide planes at $y = 3\pi/4$ m and $y = 5\pi/4$ m. The resulting increase in gradient of H_z^3 of two oppositely directed magnetic field lines then causes MRs. The reconnected field lines lying above and below the reconnection region (marked as R), are shown in gray and cyan respectively — in the panel b of the Figure 7.24. It is to be noted that with the rise of a reconnected field line above the region R (represented in gray), the footpoints of its two neighboring reconnected field

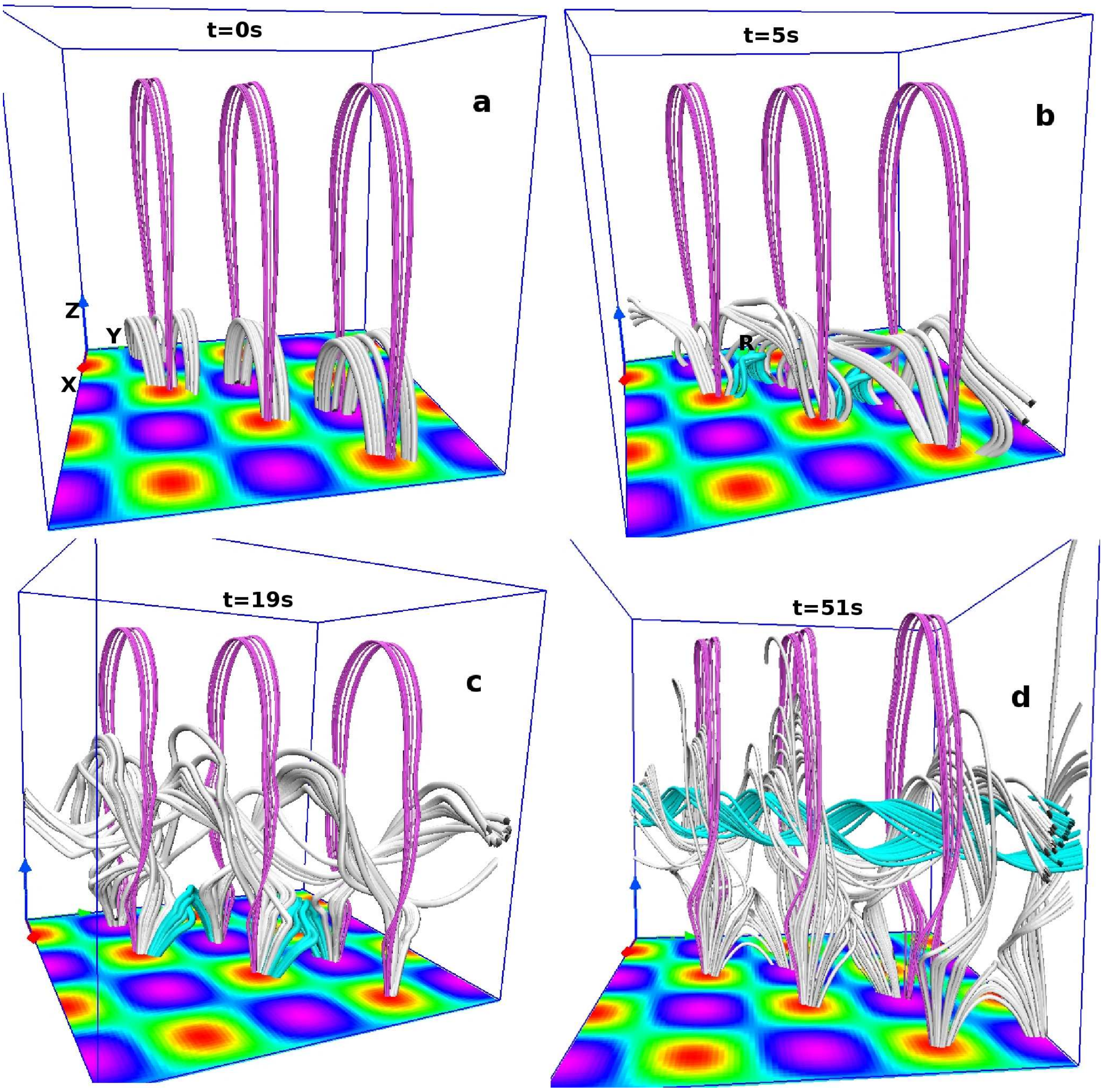

Figure 7.24: Snapshots of magnetic field lines in their evolution where $\mathbf{H}^3$ is the initial magnetic field. The overlying contours of H_z^3 on the xy-plane at $z = 0\ m$ is represented by the same color code as used in panel *c* of Figure 7.11. The magenta colored field lines have footpoints located almost at the sites where $\mid H_z^3 \mid$ is maximum, whereas the lower lying field lines (in Gray) have footpoints considerably away from these maximums. Noteworthy are the formations of helical field lines resembling a twisted flux rope, depicted in color cyan at panel *d*.

lines are also simultaneously being pushed in the direction of the concave side of the rising field line. Because of this push, the neighboring reconnected field lines bulge toward the region R, as depicted in panel *c*. Successive MRs of the inner field lines then bring two such bulged field lines arbitrarily close to each other,

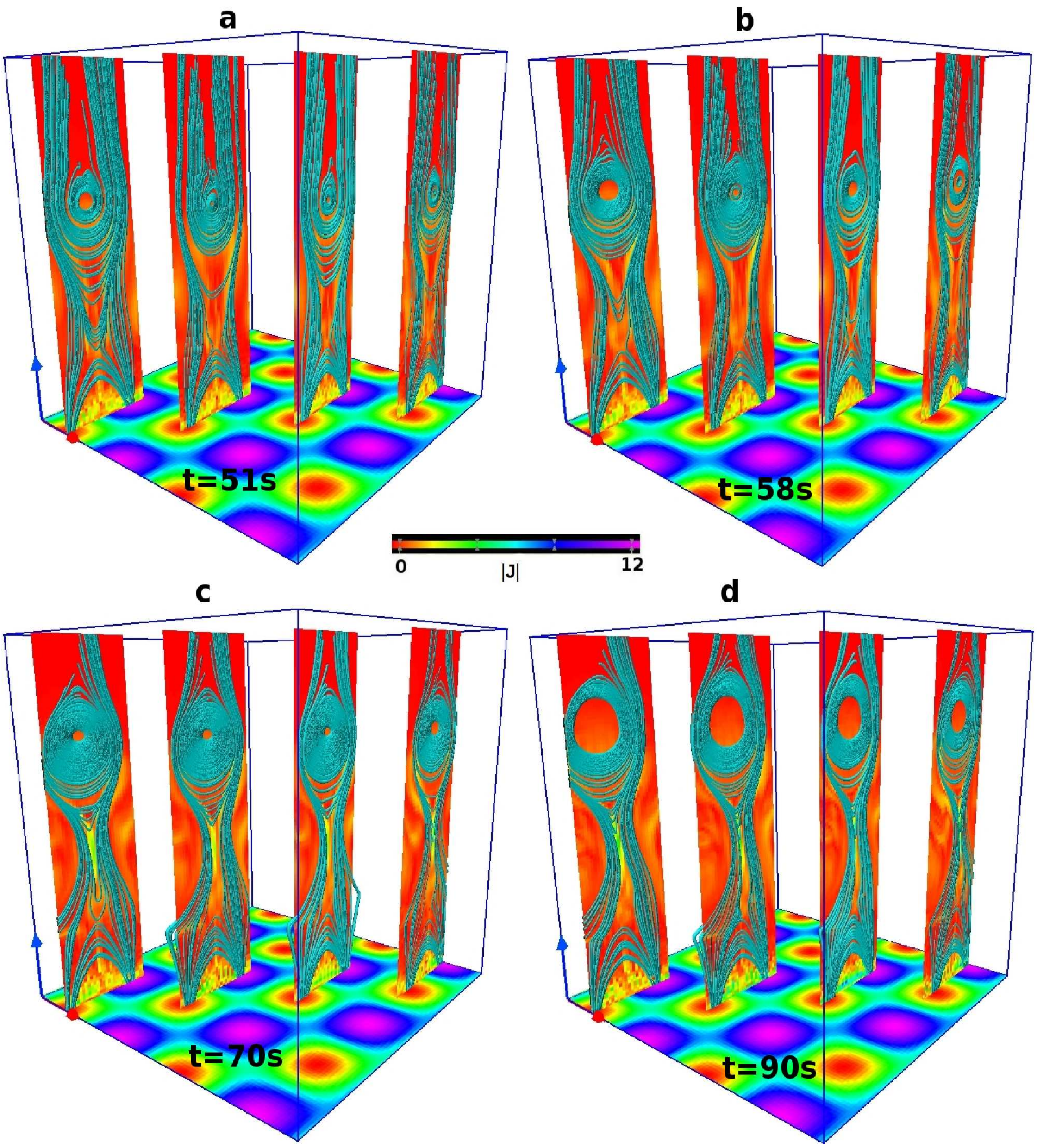

Figure 7.25: Time sequence of field lines in their evolution from the initial field $\mathbf{H}^3$ at the instances $t = 51$ s, $t = 58$ s, $t = 70$ s and $t = 90$ s, projected on x-constant planes. The overlying contours of $\mid \mathbf{J} \mid$ on these constant x-planes are represented by the color code in $A\ m^{-2}$, whereas the contours of H_z^3 on the xy-plane at $z = 0\ m$ are represented by the same color code as used in panel c of Figure 7.11. The intersections of the flux rope with these planes are identified by the closed field lines. Noteworthy are the ascend of the closed field lines, and hence the flux rope, with time along with the formation of an extended CS represented in Green. Also important is the observation that the onset of the extended CS is simultaneous with the quasi-steady phase of the evolution.

leading to further reconnections. The reconnections of the bulged field lines result in generating the detached field lines which are concave away from the negative z-direction and thus have a magnetic tension directed along the vertical. This magnetic tension then upwells a detached field line, resulting in a diminished field region which facilitates additional reconnection of bulged field lines. A repetition of the above sequence of MRs then develop the bunch of detached helical magnetic field lines which resembles a flux rope. A well developed set of such helical field lines (in color cyan) is shown in panel d of Figure 7.24. We must mention here that a strict mathematical description of flux rope as a stack of magnetic flux surfaces, requires the field lines to lie on the surface of the rope. A construction of flux surface is non-trivial in our computations which use advection of vector magnetic field. This non-triviality arises because of a general difficulty in separating out a field line that ergodically span a surface [153] from the one generated through post-processing errors. The equivalence of the detached, helical field lines observed in our computation to a flux rope is then only in an approximate sense. Also, noteworthy is the location of the flux rope which lies over the PIL. Such flux ropes located over PILs are widely believed to represent magnetic structures of solar prominences/filaments [110, 154, 155, 156]. Moreover the repeated reconnections increase magnetic pressure of the flux rope which once exceed the magnetic tension of the overlying field lines, lifts the rope along the vertical. Subsequently, this lift translates into a sustained ascend of the flux rope (Fig. 7.25) maintained by an excess magnetic pressure; generated as field lines get bottle-necked below the rope. Also simultaneous to the ascend of the rope, this excess magnetic pressure drops because of a decrease in local density of field lines. The legs of the open magnetic field lines are then sucked into this depleted field region to account for the formation of the extended CS and its continuous increase in extension. Interestingly, the appearance of the CS almost coincides with the steady phase of the evolution (Fig. 7.23). The second peak in kinetic energy is formed as the upward motion of the rope is arrested by viscosity.

7.4 Summary

In this chapter we have numerically demonstrated the formation of magnetic discontinuities or current sheets in an incompressible, viscous, thermally homogeneous magnetofluid with infinite electrical conductivity for both isolated and open systems. It also emphasizes the role of an unbalanced force pushing the magnetofluid against a viscous drag in formation of MDs. Such a study is necessary since in a multitude of physical systems like solar corona, the fluid Reynolds number is much smaller than the magnetic Reynolds number and viscous effects cannot be neglected. The initial magnetic field is a superposition of two linear force-free fields and hence has possible relevance to eruptive processes in solar atmosphere driven by magnetic flux emergence. We present both indirect and direct evidences for CS formations and their eventual decay by the numerically assisted reconnection mimicking physical magnetic reconnection in terms of maintaining computed energy balance to a reasonable numerical accuracy. It is observed that the time scales over which the CSs are forming is sensitive to viscosity. With other parameters and hence the force counterbalancing viscous drag kept constant, CSs develop at an earlier time for a less viscous magnetofluid as is evident from the plots of average and maximum electric current densities.

A more direct evidence for CS formation is obtained by analyzing the dynamics of magnetic field topology near the two and three dimensional magnetic nulls in the initial magnetic field $\mathbf{H}$. It is observed that the current density increases in the neighborhood of both three dimensional and two-dimensional nulls. For the specific initial magnetic field used in this work, the formations of CSs and their eventual decay at the neighborhood of three dimensional nulls precedes the same near the two dimensional nulls. This delay in CS formation about the two types of magnetic nulls is explained in terms of the initial Lorentz force. The only nonzero component of the initial Lorentz force at the immediate neighborhood of a 2D null is perpendicular to the plane containing the null point whereas for the 3D nulls all components of initial Lorentz force are nonzero in the immediate neighborhood. The pressing of the magnetofluid in a favorable direction then generates CSs near 3D nulls and contributes to development of the first peak in current density. In the neighborhood of 2D nulls the Lorentz force pushes the magnetofluid in a direction perpendicular to the direction favored for CS formation and hence the delay. Eventually a CS is formed by squashing of X-type nulls to two Y-type nulls through a series of complex motions along with an intermediate appearance of a concave gap, consistent with the optical analogy. A continuous extension of these 2D CS in the third direction results in a twisted current sheet, the decay of which gives the second peak in current density.

We also discussed the asymptotic topologies of magnetic field lines shaped up by repeated events of magnetic reconnection using computations relying on the ILES property of nonoscillatory numerics. For the purpose, the initial magnetic field is constructed by a superposition of two linear force-free fields, solved appropriately in the $z \geq 0$ positive half-space of a partially periodic Cartesian coordinate system. This use of the positive half-space being traditional in mimicking the solar atmosphere, the computations presented here could be of direct relevance to observations. Also the corresponding initial magnetic field lines are of the form of loops, similar in geometry to the observed coronal loops.

The dynamics of these initial field lines are investigated in terms of their footpoint evolution with an objective to explore the development of physically realizable magnetic structures through the process of successive magnetic reconnections (MRs). To be in conformity with the analytical requirements of CS formation, the magnetofluid is evolved from an unbalanced state of rest via viscous relaxation under the condition of flux freezing. In the process, magnetic field gradients sharpen unboundedly, ultimately generating under-resolved scales. These scales are then filtered out from the system through numerically assisted MRs. To regularize these reconnections, we rely on the proven dissipative property of MPDATA — the second order accurate advection scheme on which our computational model is based. Post MRs, the computations are again well-resolved and satisfy the condition of flux-freezing. The field lines frozen to the reconnection outflow then press onto other flux systems and repeat the above process. In particular, we explore this repetitive process for field lines characterized with three distinct cases of footpoint geometry.

In Case i, we choose the initial magnetic field to be untwisted with footpoints of opposite polarities satisfying a mirror symmetry and having straight PILs. The magnetofluid evolves with footpoint reconnections and leads to the formation of magnetic islands along with two X-type neutral points. Further, these X-type neutral points vertically ascend along with a simultaneous increase in separation between the footpoints of the underlying reconnected field lines — a phenomenon observed in the context of solar flares. More importantly, continual pressing of these islands develop a new pair of X-type neutral points which when further squashed, generate two Y-type neutral points and an extended CS in accordance to the Parker's optical analogy.

The initial field lines in Case ii are also untwisted but characterized with curved PILs. The corresponding footpoints of opposite polarities satisfy a glide symmetry and hence are topologically more complex in comparison to the footpoints of Case i. The dynamics of the system is predominantly determined by the pressing of glide-symmetric footpoints toward each other. The resulting MRs impart a swirling motion of the magnetofluid along with the generation of helical magnetic field lines which are geometrically similar to the observed solar tornadoes. Additionally, the computations also confirm a later "untwisting" motion of these helical field lines as a consequence of repeated MRs. Such untwisting motions are also observational features of a solar tornado.

The Case iii investigates the evolution where the initial Lorentz force pushes two neighboring sets of twisted, glide-symmetric field lines. The repeated MRs in this case generate magnetic structure similar in appearance to a detached, twisted flux rope. The computations also suggest a sustained ascend of this flux rope driven by a difference in magnetic pressure, above and below the rope. Noteworthy is the development of an extended CS below the flux rope.

Overall, the simulations presented in this chapter are suggestive of MD formation through continuous deformation of magnetic field lines where the initial magnetic field is a superposition of two linear force-free fields. Also, the importance of this work lies in its demonstration that different magnetic structures observed at the solar atmosphere can have a common origin in repeated MRs—sustained by an interplay of forcing and magnetic diffusion in a system of loops. Such repeated MRs (along with the prerequisite development of CSs), being fundamental to astrophysical plasmas; the resulting magnetic structures are expected to develop in other stellar coronae also. Moreover, we find that implicit large eddy simulations are capable to imitate MRs in a high Lundquist number magnetofluid in terms of their localized occurrences.

Chapter 8

On Finite Time Formation of Magnetic Discontinuities

In the previous chapter we have demonstrated the formation of magnetic discontinuity and also the role of magnetic reconnection to establish the quasi-steady equilibrium. The importance of this study is to explore the basic underlying physics of discontinuity formation. The simulations show the general trend to form the magnetic discontinuity, but the formation of a true mathematical discontinuity is limited by the grid resolution. The onset of magnetic reconnection prior to reach a limit of true discontinuity then open a new problem that whether a true magnetic discontinuity will form in finite or an infinite time [148, 157]. The estimation of this time is essential from observational viewpoint to account for the coronal heating rate and also to predict the dynamics of eruptive phenomena like flares or CMEs [158, 159].

Despite the limited grid resolution, the general trend of the growth of the electric current density provides a numerical procedure to inquire whether a discontinuity will form in a finite or an infinite time. The electric current density grows as power law for finite formation time of MD, while it grows algebraically or exponentially for an infinite formation time of MD [158]. In this chapter we numerically investigate the possibility of the finite time formation of magnetic discontinuities in an incompressible fluid of infinitely large electrical conductivity.

Here simulations are carried out with varying grid resolutions with the same

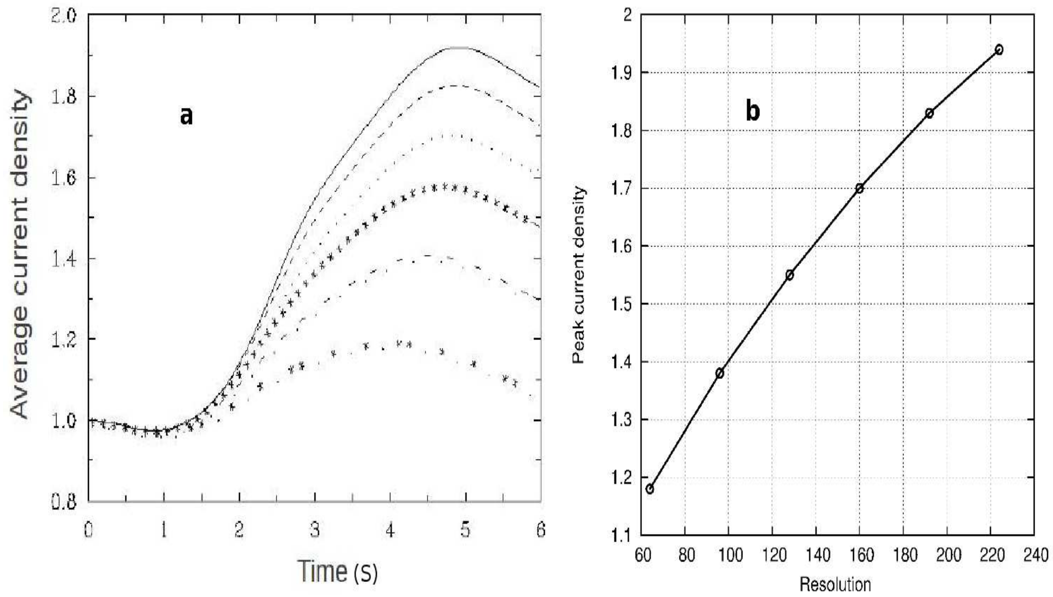

Figure 8.1: Panel a depicts the evolution of normalized current densities (each normalized with their respective initial values) averaged over the computational volume, for different grid resolutions varying from 64^3 to 224^3 in steps of 32^3. Panel b shows the variation of normalized peak current density $\mid \mathbf{J}_{max} \mid$ with increasing grid resolutions.

initial magnetic field and boundary conditions as used in the section 7.2 of the previous chapter. Panel a of Figure 8.1 shows the time variations of the normalized average current density $<\mid \mathbf{J} \mid>$ for different uniform grid resolutions varying from 64^3 (asterisk-dotted line) to 224^3 (solid line) in steps of 32^3. For each grid resolution, the magnetofluid evolves from the initial nonequilibrium state and the current density grows as the gradient in magnetic field sharpens followed by decays in current density when the numerical dissipation becomes effective due to the under-resolved scales [36]. The peak in current density is indicative of the formation of magnetic discontinuities at the 3D nulls as mentioned in the previous chapter. The peak current density $\mid \mathbf{J} \mid_{max}$ with varying grid resolution is plotted in the panel b of Figure 8.1. The increase in $\mid \mathbf{J} \mid_{max}$ with an increase in grid resolution further provide an indirect evidence of the formation of magnetic discontinuities [160, 161].

To study the finite time formation of magnetic discontinuities, we plot the time instant, $t_{\mid \mathbf{J} \mid_{max}}$, at which peak current density appears with the grid resolu-

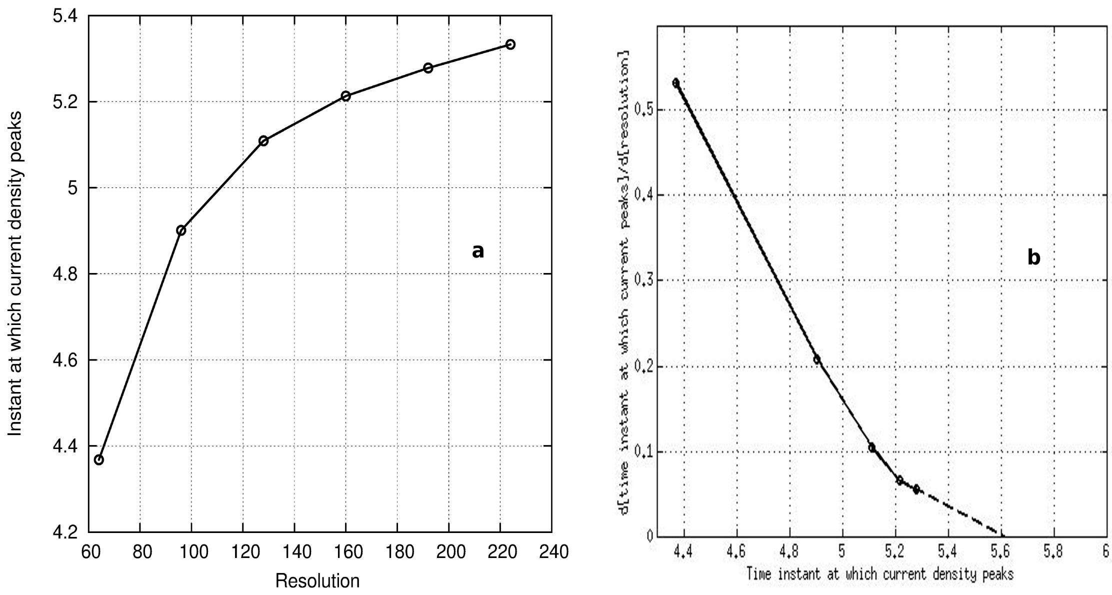

Figure 8.2: Panel a depicts the variation of $t_{|\mathbf{J}|_{max}}$ (in s) with grid resolution N_{res}. The slope of the curve of panel a vs. $t_{|\mathbf{J}|_{max}}$ (in s) is shown in panel b. The expected finite time formation of MD is ≈ 5.6 s.

tion as shown in the panel a of Figure 8.2. From this figure it is seen that the time instant at which current density peaks, shows a tendency of saturation for higher grid resolutions. This saturation of time with a simultaneous increase in the peak current density (vide panel b of Fig. 8.1) is possibly an indication of finite time formation of magnetic discontinuities. In panel b of Figure 8.2 we have plotted the slope of the curve of panel a, i.e. $dt_{|\mathbf{J}|_{max}}/dN_{res}$, with $t_{|\mathbf{J}|_{max}}$. This plot shows that the slope is decreasing, which is extrapolated up to the slope of zero to get an estimate of the corresponding saturation time. The expected finite time formation of magnetic discontinuity is ≈ 5.6 s.

Further evidence of finite time formation of magnetic discontinuity is obtained by plotting the $1/ <| \mathbf{J} |>$ with time, and extrapolating the curve to the zero value of $1/ <| \mathbf{J} |>$ [148, 157]. In panel a of Figure 8.3 we have plotted the $1/ <| \mathbf{J} |>$ with time for varying grid resolutions. In the time interval $T \in (1, 4)$ s, these curves show a general tendency to converge towards zero value of $1/ <| \mathbf{J} |>$, before the onset of numerical dissipation. Such a converging behavior of the curve of $1/ <| \mathbf{J} |>$ then indicates that the current density may

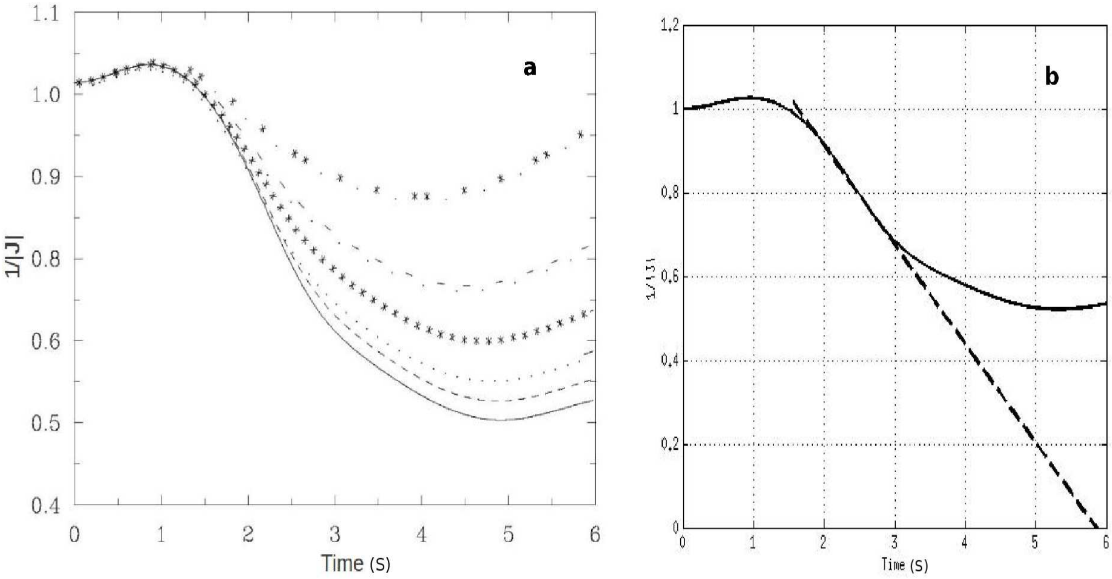

Figure 8.3: Histories of normalized $1/ <| \mathbf{J} |>$ (each normalized to their respective initial values) with varying grid resolutions (same as in panel a of Figure 8.1) is illustrated in panel a. The history of normalized $1/ <| \mathbf{J} |>$ for the grid resolution 224^3 along with the linear fit to the data curve (dotted line) is shown in panel b. The expected finite time formation of MD is $\approx 5.8\ s$.

become infinitely large in a finite time. To further elucidate the possible finite time formation of MD, the temporal evolution of $1/ <| \mathbf{J} |>$ for the highest grid resolution 224^3 is plotted in panel b of Figure 8.3. This plot shows an almost linear behavior in the ideal phase of evolution, $T \in (1, 4)\ s$, before the numerical dissipation intervenes. Extrapolating a linear fit to the data curve in the ideal phase of evolution gives a possible estimate of the finite time formation of magnetic discontinuities, which is $\approx 5.8\ s$.

In summary, we present the possible finite time formation of magnetic discontinuity in an incompressible fluid with infinitely large electrical conductivity. Two different numerical procedures are followed to show the possibility of finite time formation of MD. The results obtained from these two methods indicate the finite time behavior of the formation of magnetic discontinuity in almost the same time. The relevance of our results to a realistic situation lies in the fact that the time of MD formation scales with the Lundquist number of the magnetofluid under consideration. The results presented here are restricted to a single magnetic field topology and also with the limited grid resolutions. Further numerical simulations with different field topology and at higher grid resolutions are required to address the problem of finite time formation of magnetic discontinuities.

Chapter 9

Summary and Future Work

9.1 Summary

In this thesis we have addressed the fundamental problem of the formation of magnetic discontinuities (MDs) in a fluid with large electrical conductivity. A remarkable property of such a large electrical conductivity of the magnetofluid is to maintain the high degree of frozen-in condition. Under this frozen-in condition, an arbitrary field topology relaxing towards the asymptotic states of equilibrium will develop magnetic discontinuities. However the large but finite electrical conductivity of magnetofluid dissipates the MD, resulting in magnetic reconnection. After reconnection, the frozen-in condition is restored, and the post-reconnection field lines develop additional MDs. This process repeats till the magnetofluid achieves the asymptotes of equilibrium. The above process of MD formation and its dissipation is a possible mechanism to heat the corona at its million degree Kelvin temperature.

The theoretical idea of the formation of magnetic discontinuity was proposed by Parker. The analytical demonstration of the basic process of MD formation is a formidable task because of the nonlinear nature of the governing equations. We demonstrate this process of MD formation through numerical methods. For the purpose, we have used the numerical model EULAG-MHD which is based on a second order accurate nonoscillatory numerical scheme MPDATA. This MPDATA has an inherent property of implicit dissipation that provides the basis for ILES (implicit large eddy simulation). The ILES property of MPDATA is essential for resolving the formation of magnetic discontinuities.

The preservation of field topology along with simultaneous dissipation of energy provides an elegant way to find the terminal state of equilibrium using the techniques of variational calculus. We have used the two-fluid plasma model for an open system to obtain the terminal state of equilibrium with flow coupled magnetic field. Such a terminal equilibrium may have possible relevance for modeling the high β solar corona.

We have numerically investigated that it is the locations of 2D and 3D magnetic nulls where magnetic discontinuities appear. In general, it is believed that such nulls are the potential sites at which discontinuity forms naturally. We also found that the magnetic discontinuity appears even in the absence of magnetic nulls. The formation of magnetic discontinuity in absence of magnetic nulls is a more promising scenario of the Parker theory, which states that magnetic nulls are not essential for the formation of MD.

The ILES property of the EULAG-MHD provides an opportunity to understand the process of repeated magnetic reconnections. The ongoing process of repeated reconnections is a result of the competition between the forcing and the residual numerical dissipation. Depending upon the initial magnetic topology, the process of repeated reconnections generate various magnetic structures. Such structures happen to be topologically similar in appearance to that observed in the solar atmosphere. Thus we may infer some clues about the formation of different kinds of coronal structures from these numerical simulations.

Overall, in this thesis attempts have been made to numerically investigate the formation of magnetic discontinuities and subsequent magnetic reconnections which generates various magnetic structures as the magnetofluid relaxes towards the quasi-equilibrium. This study has two important implications. (1) To numerically demonstrate the basic MHD process of the formation of magnetic discontinuities as suggested by Parker. (2) To understand the topological rearrangements of field lines which the coronal magnetic fields or loops may exhibit while seeking to relax towards the quasi-equilibrium.

9.2 Future Work

We have demonstrated the formation of MDs by continuous deformation of the initial complex topology of the magnetic field. However, we have not addressed quantitatively the role of magnetic field strength, which is associated with magnetic twist, in the generation of magnetic discontinuities [3]. We will attempt this problem in future.

A topologically complex magnetic field can be generated by continuously deforming an initial magnetic field by imposing twisting or shearing motion [162, 163]. In such settings of magnetic configuration, we will numerically investigate the formation of magnetic discontinuities. This study will be more relevant to the solar corona, where the deformation of the magnetic field is led by the convective motion at the photosphere.

In this work we have investigated the possible locations of 2D and 3D nulls where discontinuity appears. Future work will also be focused on to investigate the formation of MDs at quasi-separatrix layers [164, 165]— locations where connectivity of field lines changes rapidly.

The works presented here show that implicit large eddy simulation (ILES) are capable to imitate magnetic reconnection in a magnetofluid with large electrical conductivity. Such simulations in absence of physical diffusivity, provides no direct estimate of the reconnection rate. Therefore, an apt physical diffusivity is required to further explore the dynamics of MD formation.

Bibliography

[1] B. Edlén, Monthly Notices Roy. Astron. Soc. **105**, 323 (1945).

[2] M. J. Aschwanden, *Physics of the Solar Corona: An Introduction* (Springer, Berlin, 2004).

[3] E. N. Parker, *Spontaneous Current Sheets Formation in Magnetic Fields* (Oxford University Press, New York, 1994).

[4] J. A. Klimchuk, Sol. Phys. **234**, 41 (2006).

[5] D. Biskamp, *Magnetic Reconnection in Plasmas* (Cambridge University Press, Cambridge, 2000).

[6] B. C. Low and R. Wolfson, Astophys. J. **324**, 574 (1988).

[7] E. N. Parker, Astrophys. J. **174**, 499 (1972).

[8] E. N. Parker, Geophys. Fluid Dyn. **34**, 243 (1985).

[9] E. N. Parker, Geophys. Fluid Dyn. **35**, 277 (1986).

[10] E. N. Parker, *Conversations on Electric and Magnetic Fields in the Cosmos* (Princeton University Press, Princeton, 2007).

[11] E. N. Parker, Astrophys. J. **330**, 474 (1988).

[12] E. N. Parker, Phys. Rev. Lett. **85**, 4405 (2000).

[13] R. Rosner, L. Golub, and G. S. Vaiana, Ann. Rev. Astron. Astrophys. **23**, 413 (1985).

[14] J. W. Dungey, Phys. Rev. Lett. **6**, 47 (1961).

[15] C. T. Russell, IEEE Trans. Plasma Sci. **28**, 1818 (2000).

[16] J. Raeder, Ann. Geophys. **24**, 381 (2006).

[17] J. Birn, J. C. Dorelli, M. Hesse, and K. Schindler, J. Geophys. Res. **109**, A02215 (2004).

[18] M. Yamada, H. Ji, S. Hsu, T. Carter, R. Kulsrud, et al., Phys. Plasmas **4**, 1936 (1997).

[19] M. Yamada, H. Ji, S. Hsu, T. Carter, R. Kulsrud, et al., Phys. Rev. Lett. **78**, 3117 (1997).

[20] E. G. Zweibel and M. Yamada, Ann. Rev. Astron. Astrophys. **47**, 291 (2009).

[21] C. Hirsch, *Numerical Computation of Internal and External Flows* (Butterworth-Heinemann, 2007).

[22] R. Courant and D. Hilbert, *Methods of Mathematical Physics II* (Wiley, New York, 1962).

[23] J. M. Prusa, P. K. Smolarkiewicz, and A. A. Wyszogrodzki, Comput. Fluids **37**, 1193 (2008).

[24] P. K. Smolarkiewicz, Int. J. Numer. Methods Fluids **50**, 1123 (2006).

[25] F. F. Chen, *Introduction to Plasma Physics and Controlled Fusion* (Plenum Press, New York, 1984).

[26] J. A. Bittencourt, *Fundamentals of Plasma Physics* (Pergamon Press, New York, 1986).

[27] P. M. Bellan, *Fundamentals of Plasma Physics* (Cambridge University Press, 2006).

[28] J. P. Friedberg, *Ideal Magnetohydrodynamics* (Plenum, New York, 1987).

[29] H. F. Weinberger, *A First Course in partial Differential Equations* (Blaisdell, New York, 1965).

[30] G. Evans, J. Blackledge, and P. Yardley, *Analytic Methods for Partial Differential Equations* (Springer-Verlag, London, 1999).

[31] E. N. Parker, Plasma Phys. Control. Fusion **54**, 124028 (2012).

[32] E. N. Parker, Geophys. Astrophys. Fluid Dyn. **45**, 159 (1989).

[33] E. N. Parker, Geophys. Astrophys. Fluid Dyn. **46**, 105 (1989).

[34] E. N. Parker, Geophys. Astrophys. Fluid Dyn. **50**, 229 (1990).

[35] P. K. Smolarkiewicz and P. Charbonneau, J. Comput. Phys. **236**, 608 (2013).

[36] D. Kumar, R. Bhattacharyya, and P.K. Smolarkiewicz, Phys. Plasmas **20**, 112903 (2013).

[37] J. M. Prusa and P. K. Smolarkiewicz, J. Comput. Phys. **190**, 601 (2003).

[38] N. P. Wedi and P. K. Smolarkiewicz, J. Comput. Phys. **193**, 20 (2004).

[39] P. K. Smolarkiewicz and L. G. Margolin, Appl. Math. and Comput. Sci. **4**, 527 (1994).

[40] R. Bhattacharyya, B. C. Low, and P. K. Smolarkiewicz, Phys. Plasmas **17**, 112901 (2010).

[41] S. Kumar, R. Bhattacharyya, and P. K. Smolarkiewicz, Phys. Plasmas **21**, 052904 (2014).

[42] J. -F. Cossette, P. K. Smolarkiewicz, and P. Charbonneau, J. Comput. Phys. **274**, 208 (2014).

[43] P. K. Smolarkiewicz, J. Comput. Phys. **54**, 325 (1984).

[44] P. K. Smolarkiewicz and L. G. Margolin, Month. Weather Rev. **121**, 1847 (1993).

[45] P. K. Smolarkiewicz and L. G. Margolin, J. Comp. Phys. **140**, 459 (1998).

[46] L. G. Margolin and M. Shashkov, Int. J. Num. Meth. Fluids **50**, 1193 (2005).

[47] F. F. Grinstein, L. G. Margolin, and W. J. Rider, *Implicit Large Eddy Simulation: Computing Turbulent Fluid Dynamics* (Cambridge University Press, 2006).

[48] A. Harten, J. Comput. Phys. **49**, 357 (1983).

[49] J. P. Boris and D. L. Book, J. Comp. Phys. **11**, 38 (1973).

[50] S. T. Zalesak, J. Comp. Phys. **31**, 335 (1979).

[51] J. P. Boris, *On Large eddy Simulation using Subgrid Turbulence Models, in Whither Turbulence? Turbulence at the Crossroads, ed. J. L. Lumley* (Springer-Verlag, New York, 1990).

[52] L. G. Margolin and W. J. Rider, Int. J. Num. Meth. **39**, 821 (2002).

[53] L .G. Margolin, P. K. Smolarkiewicz and A. A. Wyszogrodzki, Int. J. Num. Meth. **24**, 862 (2002).

[54] M. Ghizaru, P. Charbonneau, and P. K. Smolarkiewicz, Astrophys. J. Lett. **715**, L133 (2010).

[55] E. Racine, P. Charbonneau, M. Ghizaru, A. Bouchat, and P.K. Smolarkiewicz, Astrophys. J. **735**, 46 (2011).

[56] P. Beaudoin, P. Charbonneau, E. Racine, and P.K. Smolarkiewicz, Sol. Phys. **282**, 335 (2013).

[57] P. Charbonneau and P. K. Smolarkiewicz, Science **340**, 42 (2013).

[58] R. Wolfson, Astophys. J. **344**, 471 (1989).

[59] B. C. Low, Astophys. J. **323**, 358 (1987).

[60] G. Vekstein, E. R. Priest, and T. Amari, Astron. Astophys. **243**, 492 (1991).

[61] B. C. Low, Astophys. J. **340**, 558 (1989).

[62] R. Wolfson, Astophys. J. **443**, 810 (1995).

[63] A. M. Janse and B. C. Low, Astophys. J. **690**, 1089 (2009).

[64] B. C. Low and A. M. Janse, Astophys. J. **696**, 821 (2009).

[65] A. M. Janse and B. C. Low, Astophys. J. **722**, 1844 (2010).

[66] B. C. Low, Astophys. J. **381**, 295 (1991).

[67] B. C. Low, Astron. Astophys. **253**, 311 (1992).

[68] A. A. van Ballegooijen, Astophys. J. **298**, 421 (1985).

[69] S. K. Antiochos, Astophys. J. **312**, 886 (1987).

[70] E. G. Zweibel and H. S. Li, Astophys. J. **312**, 423 (1987).

[71] I. J. D. Craig and A. D. Sneyd, Sol. Phys. **232**, 41 (2005).

[72] B. C. Low, Astrophys. J. **718**, 717 (2010).

[73] B. C. Low, Sol. Phys. **266**, 277 (2010).

[74] A. M. Janse, B. C. Low, and E. N. Parker, Phys. Plasmas **17**, 092901 (2010).

[75] Z. Mikic, D. D. Schnack, and G. Van Hoven, Astophys. J. **338**, 1148 (1989).

[76] A. A. van Ballegooijen, Geophys. Astrophys. Fluid Dyn. **41**, 181 (1988).

[77] A. W. Longbottom, G. J. Rickard, I. J. D. Craig, and A. D. Sneyd, Astophys. J. **500**, 471 (1998).

[78] D. P. Stern, Rev. Geophys. **14**, 199 (1976).

[79] B. C. Low, Astrohys. J. **646**, 1288 (2006).

[80] D. I. Pontin and Y.-M. Huang, Astrohys. J. **756**, 7 (2012).

[81] A. L. Wilmot-Smith, G. Hornig, and D. I. Pontin, Astrohys. J. **696**, 1339 (2009).

[82] G. L. Withbroe and R. W. Noyes, Ann. Rev. Astron. Astrophys. **15**, 363 (1977).

[83] B. Lyot, Monthly Notices Roy. Astron. Soc. **99**, 580 (1939).

[84] H. Lin, M. J. Penn, and S. Tomczyk, Astrohys. J. Lett. **541**, L83 (2000).

[85] R. Ramesh, C. Kathiravan, and C. V. Sastry, Astrophys. J. **711**, 1029 (2010).

[86] G. B. Gelfreikh, N. G. Peterova, and B. I. Riabov, Sol. Phys. **108**, 89 (1987).

[87] D. E. Gary and G. J. Hurford, Astrohys. J. **420**, 903 (1994).

[88] E. Marsch, T. Wiegelmann, and L. D. Xia, Astron. Astrophys. **428**, 629 (2004).

[89] T. Wiegelmann, A. Lagg, S. K. Solanki, B. Inhester, and J. Woch, Astron. Astrophys. **433**, 701 (2005).

[90] V. M. Nakariakov, L. Ofman, E. E. Deluca, B. Roberts, and J. M. Davila, Science **285**, 862 (1999).

[91] V. M. Nakariakov and L. Ofman, Astron. Astrophys. **372**, L53 (2001).

[92] E. Verwichte, M. J. Aschwanden, T. Van Doorsselaere, C. Foullon, and V. M. Nakariakov, Astrophys. J. **698**, 397 (2009).

[93] T. Van Doorsselaere, V. M. Nakariakov, P. R. Young, and E. Verwichte, Astron. Astrophys. **487**, L17 (2008).

[94] V. M. Nakariakov and E. Verwichte, Living Reviews in Solar Physics **2**, 3 (2005).

[95] G. A. Gary, Sol. Phys. **203**, 71 (2001).

[96] G. A. Gary and D. Alexander, Sol. Phys. **186**, 123 (1999).

[97] R. F. Stein and J. Leibacher, Ann. Rev. Astron. Astrophys. **12**, 407 (1974).

[98] R. G. Athay and O. R. White, Astrophys. J. **226**, 1135 (1978).

[99] H. Alfvén, Monthly Notices Roy. Astron. Soc. **107**, 211 (1947).

[100] J. B. Zirker, Sol. Phys. **148**, 43 (1993).

[101] E. N. Parker, J. Geophys. Res. **62**, 509 (1957).

[102] P. A. Sweet, IAU Symposium **6**, 123 (1957).

[103] H. E. Petschek, NASA Special Publication **50**, 425 (1964).

[104] K. Shibata and T. Magara, Living Rev. Sol. Phys. **8**, 6 (2011).

[105] G. W. Pneuman, *Solar Flare Magnetohydrodynamics* (Gordon and Breach Science Publishers, New York, 1981).

[106] S. Tsuneta, H. Hara, T. Shimizu, L. W. Acton, K. T. Strong, H. S. Hudson, and Y. Ogawara, PASJ **44**, L63 (1992).

[107] H. Zirin , *Astrophysics of the Sun* (Cambridge University Press, Cambridge, 1988).

[108] R. Kippenhahn and A. Schlüter, Zeitschrift für Astrophysik **43**, 36 (1957).

[109] M. Kuperus and M. A. Raadu, Astron. Astrophys. **31**, 189 (1974).

[110] S. E. Gibson and Y. Fan, J. Geophys. Res. **111**, 12103 (2006).

[111] E. R. Priest, A. W. Hood, and U. Anzer, Astrophys. J. **344**, 1010 (1989).

[112] A. A. van Ballegooijen and S. R. Cranmer, Astrophys. J. **711**, 164 (2010).

[113] C. R. DeVore and S. K. Antiochos, Astrophys. J. **539**, 954 (2000).

[114] B. T. Welsch, C. R. DeVore, and S. K. Antiochos, Astrophys. J. **634**, 1395 (2005).

[115] P. C. Martens and C. Zwaan, Astrophys. J. **558**, 872 (2001).

[116] Y. Su, T. Wang, A. Veronig, M. Temmer, and W. Gan, Astrophys. J. Lett. **756**, L41 (2012).

[117] X. Li, H. Morgan, D. Leonard, and L. Jeska, Astrophys. J. Lett. **752**, L22 (2012).

[118] S. Wedemeyer-Böhm, E. Scullion, O. Steiner, L. Rouppe van der Voort, J. de La Cruz Rodriguez, V. Fedun, and R. Erdélyi, Nature **486**, 505 (2012).

[119] N. K. Panesar, D. E. Innes, S. K. Tiwari, and B. C. Low, Astron. Astrophys. **549**, A105 (2013).

[120] S. Wedemeyer, E. Scullion, L. Rouppe van der Voort, A. Bosnjak, and P. Antolin, Astrophys. J. **774**, 123 (2013).

[121] R. M. Illing and A. J. Hundhausen, J. Geophys. Res. **91**, 10951 (1986).

[122] B. C. Low, Sol. Phys. **167**, 217 (1996).

[123] S. Ortolani and D. D. Schnack, *Magnetohydrodynamics of Plasma Relaxation* (World Scientific, Singapore, 1993).

[124] J. B. Taylor, Phys. Rev. Lett. **33**, 1139 (1974).

[125] K. Avinash and J. B. Taylor, Research Report DOE=ET-53088-472, IF-SR-472, University of texas, Austin , (1991).

[126] K. Avinash, Phys. Fluids **B4**, 3856 (1992).

[127] H. K. Moffatt, J. Fluid Mech. **35**, 117 (1969).

[128] M. A. Berger and G. B. Field, J. Fluid Mech. **147**, 133 (1984).

[129] J. H. Finn and T. M. Antonsen, Comm. Plasma Phys. Contr. Fus. **9**, 111 (1985).

[130] L. Woltjer, A theorem on force-free magnetic fields, Proceedings of the National Academy of Science **44**, 489 (1958).

[131] M. Yamada , J. Geophys. Res. **104**, 14529 (1999).

[132] J. Heyvaerts and E. R. Priest, Astron. Astrophys. **63**, 137 (1984).

[133] D. Nandy, M. Hahn, R. C. Canfield, and D. W. Longcope, Astrophys. J. Lett. **597**, L73 (2003).

[134] V. Krishan, J. Plasma Phys. **56**, 427 (1996).

[135] P. V. Foukal, Sol. Phys. **43**, 327 (1975).

[136] C. Chiuderi, R. Giachetti, and G. Van Hoven, Sol. Phys. **54**, 107 (1977).

[137] D. Kumar and R. Bhattacharyya, Phys. Plasmas **18**, 084506 (2011).

[138] R. Bhattacharyya, M. S. Janaki, B. Dasgupta, and G. P. Zank, Sol. Phys. **240**, 63 (2007).

[139] D. Biskamp, *Magnetohydrodynamic Turbulence* (Academic Press, 2008).

[140] S. Chandrasekhar and P. C. Kendall, Astrophys. J. **126**, 457 (1957).

[141] D. Kumar, R. Bhattacharyya, and P. K. Smolarkiewicz, Phys. Plasmas **22**, 012902 (2015).

[142] L. G. Margolin, W. J. Rider, and F. F. Grinstein, J. Turbul. **7**, N15 (2006).

[143] A. Domaradzki, Z. Xiao, and P. K. Smolarkiewicz, Phys. Fluids **15**, 3890 (2003).

[144] B. Ravindra, P. Venkatakrishnan, S. K. Tiwari, and R. Bhattacharyya, Astrophys. J. **740**, 637 (2011).

[145] E. R. Priest and T. G. Forbes, *Magnetic Reconnection: MHD Theory and Applications* (Cambridge University Press, New York, 2000).

[146] E. R. Priest and V. S. Titov, Phil. Trans. R. Soc. Lond. **354**, 2951 (1996).

[147] E. R. Priest and P. Démoulin, J. Geophys. Res. **100**, 23443 (1995).

[148] R. M. Kerr and A. Brandenburg, Phys. Rev. Lett. **83**, 1155 (1999).

[149] L. G. Margolin, P. K. Smolarkiewicz, and A. A. Wyszogradzki, J. Appl. Mech. **73**, 469 (2006).

[150] R. A. Kopp and G. W. Pneuman, Sol. Phys. **50**, 85 (1976).

[151] S. Tsuneta, Astrophys. J. **456**, 840 (1996).

[152] J. J. van Wijk, ACM Transactions on Graphics **21**, 745 (2002).

[153] J. R. Jokipii and E.N. Parker, Astrophys. J. **155**, 777 (1969).

[154] S. F. Martin, Sol. Phys. **182**, 107 (1998).

[155] B. C. Low, J. Geophys. Res. **106**, 25141 (2001).

[156] Y. Fan and S. E. Gibson, Astrophys. J. **668**, 1232 (2007).

[157] R. Grauer and C. Marliani, Phys. Rev. Lett. **84**, 21 (2000).

[158] X. Wang and A. Bhattacharjee, Astrophys. J. **420**, 415 (1994).

[159] X. Wang and A. Bhattacharjee, Astrophys. J. **401**, 371 (1992).

[160] I. J. D. Craig and Y. E. Litvinenko, Phys. Plasmas **12**, 112105 (2005).

[161] C. Mellor, C. L. Gerrard, K. Galsgaard, A. W. Hood, and E. R. Priest, Sol. Phys. **227**, 39 (2005).

[162] T. Török and B. Kliem, Astron. Astrophys. **406**, 1043 (2003).

[163] G. Aulanier, T. Török, P. Démoulin and E. E. DeLuca, Astrophys. J. **708**, 314 (2010).

[164] P. Démoulin, E. R. Priest and D. P. Lonie, J. Geophys. Res. **101**, 7631 (1996).

[165] K. Galsgaard, V. S. Titov and T. Neukirch, Astrophys. J. **595**, 506 (2003).

List of Publications

1. *Solar coronal loops as non force-free minimum energy relaxed states*, **Dinesh Kumar** and R. Bhattacharyya, Physics of Plasmas **18**, 084506 (2011).

2. *Formation of magnetic discontinuities through superposition of force-free magnetic fields: Periodic boundaries*, **Dinesh Kumar**, R. Bhattacharyya, and P. K. Smolarkiewicz, Physics of Plasmas **20**, 112903 (2013).

3. *Repetitive formation and decay of current sheets in magnetic loops: An origin of diverse magnetic structures*, **Dinesh Kumar**, R. Bhattacharyya, and P. K. Smolarkiewicz, Physics of Plasmas **22**, 012902 (2015).